博士論文

Implementation of Microwave-Activated Conditional Quantum Operations in Superconducting Circuits

（超伝導回路におけるマイクロ波誘起型
条件付き量子操作の実装）

白井 菖太郎

Implementation of Microwave-Activated Conditional Quantum Operations in Superconducting Circuits

by

Shotaro Shirai

A dissertation submitted to

Graduate School of Arts and Sciences
The University of Tokyo

for the degree of

Doctor of Philosophy

Committee in charge:

Associate Professor Atsushi Noguchi, Chair
Professor Yoshio Torii
Associate Professor Ryuji Takagi
Professor Kouichi Semba
Professor Fumiki Yoshihara

January 8, 2024

Abstract

There are two main approaches to correcting errors during quantum computation. The first one is redundantly embedding the degrees of freedom of a single qubit into multiple qubits. The second is known as bosonic codes, a method that embeds the information of a single qubit into a single multi-level system, such as a harmonic oscillator, using an auxiliary qubit. For the former, it is essential to implement quantum operations with low wiring costs and develop an architecture robust to parameter variations during fabrication steps. For the latter, it is necessary to establish a state manipulation method that does not degrade the coherence of the harmonic oscillator. Keeping these challenges in mind, we consulted on the research and obtained the following results.

To achieve high-precision control in superconducting circuits, it is essential to establish a fabrication recipe for superconducting circuit elements with sufficiently long coherence times. We achieved state-of-the-art coherence times exceeding $400\,\mu$s of transmon qubits using high-temperature-grown Titanium Nitride superconducting thin films on silicon substrates. This result was achieved by optimizing the fabrication recipe and design of the superconducting circuit.

Using a microwave-activated interaction with a fixed-frequency transmon qubit as a coupler, we developed a controlled-Z gate between transmon qubits. This method does not require frequency tunability of the qubits, and it maintains the advantages of fixed-frequency transmon qubits, such as long coherence time and low wiring cost, while minimizing the always-on residual ZZ interaction, which causes coherent errors, compared to conventional methods. This gate architecture offers higher design freedom and tolerance to parameter variations during fabrication steps.

We implemented a conditional displacement gate between an auxiliary qubit and a resonator. Previously, in superconducting circuits, a weak dispersive coupling between the resonator and transmon qubit is primarily used as a resource interaction for the conditional displacement gate. Unfortunately, this valuable control resource can be a bit-flip error propagation channel during conditional gate operations. To address this issue, we implemented artificial spin-dependent forces (SDF) interaction between a superconducting resonator and a cubic transmon, offering second-order nonlinearity as a resource of SDF interaction. Using this interaction, we successfully prepared the superconducting resonator's squeezed vacuum and cat states.

要旨

　本研究では、高い設計自由度を持つ超伝導量子回路を用いて量子誤り訂正機能の実装へ向けた研究に取り組んだ。量子誤り訂正の手法は大きく2つに分けることができ、1つ目は多数の量子ビットに冗長化して1量子ビットの自由度を埋め込む(符号化)ものである。そして2つ目はボゾニック符号とも呼ばれ、調和振動子など単一の多自由度系に冗長化して量子ビットの情報を埋め込む手法である。前者では多数の量子ビットを集積する必要があり、配線効率の良好な演算操作の実装や量子ビット製造時の作製ばらつきに対する堅牢さが、後者については、ノイズ源が少ないという調和振動子の特性を損なうことのない調和振動子の状態制御手法の確立がそれぞれ重要な課題である。これらの課題を念頭に研究を遂行し得られた成果は以下の通りである。

　超伝導回路において高精度な制御を実現するためには十分長いコヒーレンス時間を持った超伝導回路素子の作製手法の確立が必要不可欠である。本研究ではシリコン基板上に高温成長した窒化チタン超伝導薄膜を用い、作製プロセスの検討・改善により、現在主流な超伝導量子ビットの一つであるトランズモン型量子ビットにおいて最先端の性能に並ぶ$400\,\mu$sを超えるコヒーレンス時間を達成した。

　トランズモン型量子ビットには周波数固定と周波数可変の2タイプが存在し、周波数固定トランズモン型量子ビットは可変のものに比べて長いコヒーレンス時間を持ち、配線数の面でも有利である。しかし、周波数が動かせないことによって製造時のばらつきに脆弱であることに加え、コヒーレントエラーの原因になる残留ZZ相互作用の影響が大きいという問題があった。本研究では周波数固定トランズモン型量子ビットを結合器として用いることにより、配線コストを増加させることなくデータ量子ビットの間に生じる残留ZZ相互作用を小さく抑え、従来手法に比べて高い設計自由度と製造ばらつきに対する堅牢さを兼ね備えた制御位相ゲート手法を開発した。

　ボゾニック符号のプロトコルに従い符号化された状態を調和振動子中に用意するためには、調和振動子の量子状態を制御する必要があり、超伝導回路では主に共振器とトランズモン型量子ビットの間の弱い分散結合が用いられてきた。この分散結合は有用な相互作用である一方で、トランズモン型量子ビットに起きた誤りが共振器へと伝搬する経路ともなってしまう。そこで本研究では、Superconducting Nonlinear Asymmetric Inductive eLement (SNAIL)と呼ばれる素子でトランズモン型量子ビットのジョセフソン接合を置き換えたCubic Transmonと呼ばれる素子を用いて超伝導共振器との間の人工的なスピン依存力を創り出し、これを用いてCubic Transmonと超伝導共振器の間の制御変位ゲートの実装を行った。そしてこれを用いて超伝導共振器中に真空スクイーズド状態や猫状態を準備することに成功した。

Acknowledgements–謝辞

vi

さん議論していただきました。これらの議論を通じて超伝導回路の取り扱いについて、理解をより深めることができました。心より感謝申し上げます。

　松浦康平助教には、外部の研究室に所属する著者にも気さくに声を掛けていただき、遅くまで実験につきあっていただきました。博士課程から研究室が変わり新しい環境に慣れない中、大きな励みになりました。心より感謝申し上げます。

　博士課程(当時)の部谷謙太郎氏には、学部生時代から様々な場面でお話や議論をしていただきました。学部生時代に参加した勉強会でお会いし、理論を自在に使いこなし超伝導回路を制御している部谷さんのような研究がしたいと思ったことが超伝導回路の研究へのめりこみ、博士課程まで進学するきっかけの一つとなりました。心より感謝申し上げます。

　河野信吾研究員(当時)には、理化学研究所のクリーンルームの中やランチルームで気さくに声を掛けていただき、超伝導回路の作製や測定について多くの知見を教えていただきました。心より感謝申し上げます。

　博士課程(当時)の砂田佳希氏には、超伝導量子ビットの測定や設計について多くの議論をしていただきました。砂田さんの測定データの品質の高さ、理論モデルの正確さは自身の研究を進めていく上で重要な指針でもありました。心より感謝申し上げます。

　博士課程の竹田悠大河氏には、著者の研究に不可欠なサンプルを提供していただきました。また、粘り強く実験に取り組み、目的を達成していく姿には大きな感銘を受けました。心より感謝申し上げます。

　博士課程の重藤真人氏には、研究室所属当初から研究に関することだけでなく多くの場面で話し相手になっていただきました。セミナー発表の際など、重藤さんの物理的示唆に富んだ考察の数々に多くのことを学ばせていただきました。心より感謝申し上げます。

　博士課程の谷口建人氏には、互いの研究に関して多くの議論をしていただきました。理論的解析や考察をもとに次々と測定系を構築し実験を進めていく姿はとてもパワフルで、自身の研究を進める上でも大きな励みとなりました。心より感謝申し上げます。

　修士課程(当時)の大久保裕太氏には、本研究のテーマの一つである2量子ビットゲートの実証実験をともに行っていただきました。どんどんと実験技術を身に付けて測定を進めていく姿は大きな刺激となりました。心より感謝申し上げます。

　修士課程の松山勇喜氏とは、実験やサンプル作製を一緒に行う機会が多くあり、難易度の高いサンプル作製にも工夫を凝らして取り組む姿に大きな刺激を受けました。心より感謝申し上げます。

　野口研究室で学生としてともに励んだ渡辺玄哉氏、中島悠来氏、前蔵遼氏、橋爪みのり氏、木名瀬哲氏、遊喜光氏、安藤元太氏、柏本佳寿氏にも心より感謝申し上げます。著者は駒場キャンパスの研究室に顔を出す機会はあまり多くありませんでしたが、研究に関する議論だけでなく、皆さんとの雑談も楽しい研究室生活を送るうえでとても大切な時間でした。

　東京大学野口研究室アシスタントの寺田規美代氏には、書類手続きなど多くの場面で助けていただきました。また、いろいろな楽しい催しを企画してくださり、研究室生活が明るくとても楽しいものとなりました。心より感謝申し上げます。

　理化学研究所量子コンピュータ研究センターアシスタントの加藤彩子氏には、書類手続きや物品の発注など多くの場面で助けていただきました。おかげで円滑な研究室生活を送ることができました。心より感謝申し上げます。

　量子情報関東Student Chapterのメンバーの皆様には、円滑な研究会運営を行うために様々な面で協力していただきました。皆様のおかげでどの研究会も活気にあふれ、実り多いものとなりました。心より感謝申し上げます。

　最後に、博士課程進学を快く後押ししていただき、これまでの学生生活を支えてくださった両親や家族に心より感謝申し上げます。

Contents

Chapter 1

Introduction

The concept of a quantum computer emerged in the 1980s. Benioff demonstrated that unitary time evolutions can perform calculations without energy dissipation [1]. Feynman also highlighted the challenges of simulating natural phenomena with traditional computers and proposed using quantum mechanical systems as a solution [2]. Following this, in 1985, Deutsch formulated the quantum Turing machine model. Then, Shor devised a quantum algorithm for prime factorization in polynomial time in 1994. During the mid-1990s, there was a notable advancement in the experimental field. In 1995, Wineland and colleagues successfully demonstrated a controlled-NOT gate using a trapped Beryllium ion system [3]. In addition, a ground-breaking advancement, the realization of a superconducting qubit [4], was achieved in 1999 by Nakamura and Tsai's group. These experimental advancements have paved the way for more complex quantum computing systems.

Today, the scope of quantum information science extends well beyond quantum computation. It encompasses various applications such as communications, sensing, high-energy physics, and dark matter search. Numerous research institutes and companies around the globe are actively working towards integrating these quantum technologies into society. Today, various physical systems, such as superconducting circuits, trapped charged particles, and semiconductor quantum dots, are used to realize these technologies. Furthermore, with the advent of programmable quantum processors in the 100+ qubit class, we are now transitioning into a phase where the practicality of quantum algorithms can be tested on actual devices. However, as of 2023, these quantum processors are called Noisy Intermediate-Scale Quantum (NISQ) devices [5]. The accuracy of each operation in these devices is approximately in the 99% range, which means that the deeper the quantum circuit, the more the calculation results are obscured by noise. Quantum error correction codes are a potential solution to address errors in quantum computations, and they are currently undergoing extensive research both theoretically and experimentally. However, implementing quantum error correction requires significant overhead for both the quantum bits and classical control systems, making it crucial to implement the tools needed for quantum error correction efficiently.

In this thesis, we focused on research toward implementing quantum error correction efficiently using superconducting quantum circuits, which possess a high degree of design freedom. In the field of superconducting circuits, there are two main types of quantum error correction approaches. The first type involves redundantly embedding the degrees of freedom of a single qubit into multiple qubits. For this approach, it is necessary to integrate a significant number of physical qubits, and it is also important to implement operations with low wiring costs and robustness against design parameter fluctuations during the fabrication process. The second type is known as bosonic codes, a method

that embeds the information of a single qubit into a single multi-level system, such as a harmonic oscillator, using an auxiliary qubit. The harmonic oscillators are implemented in superconducting circuits as superconducting 3D cavities or lumped element resonators, which have high coherence. Auxiliary qubit-conditional operations are important in running a bosonic error correction. However, implementing these operations can also degrade the coherence of the resonator. Therefore, it is crucial to implement conditional operations that minimize the impact on the resonator's coherence.

Keeping these challenges in mind, we first developed a fabrication recipe for superconducting circuit elements with sufficiently long coherence times, which is important for high-quality quantum operations. Here, using high-temperature-grown Titanium Nitride superconducting thin films on silicon substrates, we achieved coherence times exceeding $400\,\mu$s of transmon qubits and internal quality factors larger than 10^6 of lumped element superconducting resonators. Then, using the recipe, we fabricated devices mainly for two types of experiments. One is for a microwave-activated controlled-Z gate implementation using a fixed-frequency transmon qubit as a coupler. This method does not require frequency tunability of the transmon qubits, and it maintains the advantages of fixed-frequency transmon qubits, such as long coherence time and low wiring cost, while suppressing a residual ZZ interaction, which causes coherent errors, compared to conventional methods. The other one is for a microwave-activated conditional displacement gate implementation using a flux-biased Superconducting Nonlinear Asymmetric Inductive element (SNAIL), offering second-order nonlinearity to the system. Previously, in superconducting circuits, a weak dispersive coupling between the resonator and transmon qubit was primarily used as a resource interaction for the conditional displacement gate. This valuable control resource can be a bit-flip error propagation channel during conditional gate operations. To address this issue, we implemented artificial spin-dependent forces between a superconducting resonator and a Cubic Transmon, which replaced the Josephson junction with a SNAIL. We successfully prepared squeezed vacuum and cat states in the superconducting resonator using this device.

1.1   Structure of this thesis

This thesis is structured as follows. In Chapter 2, we introduce the theoretical background of circuit-QED. In Chapter 3, we introduce the superconducting circuit design strategy. In Chapter 4, we describe our experimental setup and devices. In Chapter 5, we report measurement results of high-quality transmons and resonators. In Chapter 6, we propose and demonstrate the microwave-activated controlled-Z gate using the fixed-frequency transmon coupler. In Chapter 7, we propose and demonstrate the microwave-activated conditional displacement gate implementation using a flux-biased SNAIL. In Chapter 8, we summarize our results and discuss prospects.

Chapter 2

Circuit quantum electrodynamics

The fundamental procedure in circuit-Quantum Electrodynamics (circuit-QED) experiments is designing a circuit that exhibits quantum behavior and then fabricating and measuring the circuit based on that design. In this cycle, circuit quantization bridges the gap between circuit symbols depicted in a blueprint and a Hamiltonian that contains information about the circuit's quantum behavior.

This chapter summarizes the procedure for deriving a Hamiltonian from a schematic. Then, based on the obtained Hamiltonians, we introduce some essential experimental techniques for conducting circuit-QED experiments.

2.1 Circuit elements

We first introduce superconducting quantum circuit elements constituting circuits treated in this thesis. In principle, circuits are represented using branches and two nodes. As shown in Fig. 2.1, a circuit element consists of two nodes (N_i, N_{i+1}) and a branch. The branch has a direction, where the direction of a current ($I_b(t)$) or a magnetic flux ($\Phi_b(t)$) is taken as reference and the direction of $N_i \to N_{i+1}$ is positive. Note that the direction of the voltage ($V_b(t)$) is opposite to the current.

The electromagnetic behavior of an element is expressed by its magnetic flux $\Phi_b(t)$ and charge $Q_b(t)$. From Faraday's law, an electromotive force is induced by the time variation of the magnetic flux, and there is the following relationship between the magnetic flux and voltage of an element,

$$V_b(t) = \frac{d}{dt}\Phi_b(t). \tag{2.1}$$

Assuming $\Phi_b(-\infty) = 0$ is the initial condition, the magnetic field at a certain time can
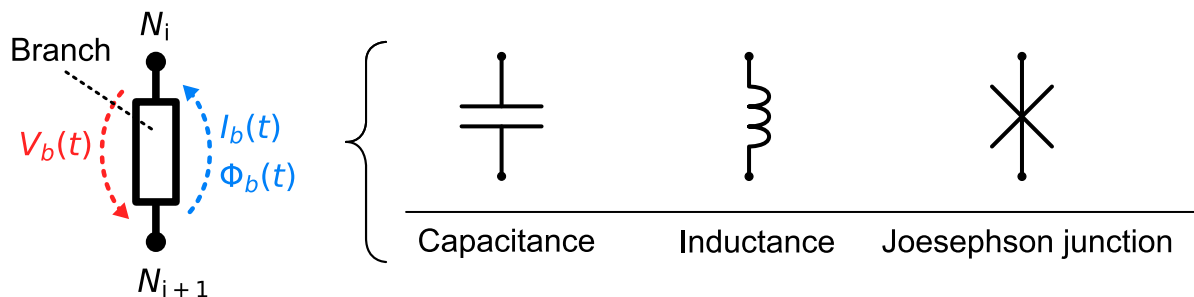
Figure 2.1: Definition of general circuit element and circuit element symbols to be covered in this chapter.

be expressed from the above equation as follows

$$\Phi_b(t) = \int_{-\infty}^{t} V_b(\tau)d\tau. \tag{2.2}$$

For the charge stored in an element, charge conservation law states that the difference in charge passing in and out through each node per unit of time must be equal to the current, and the following relationship holds

$$I_b(t) = \frac{d}{dt}Q_b(t). \tag{2.3}$$

Collecting energy stored in circuit elements is the front door to get a quantum Hamiltonian of a circuit. To do so, we first determine the energy the linear capacitance and inductance elements hold. Since the energy of capacitance C with voltage V applied is $E = \frac{1}{2}CV^2$, it can be expressed as follows

$$E_C(t) = \frac{C}{2}\left(\frac{d}{dt}\Phi(t)\right)^2 = \frac{C}{2}\dot{\Phi}^2, \tag{2.4}$$

where Eq. (2.1) is used. The energy of inductance L with current I is $E = \frac{1}{2}LI^2$ and expressed by the following equation

$$E_L(t) = \frac{L}{2}I(t)^2 = \frac{1}{2L}\Phi(t)^2 \tag{2.5}$$

where $\Phi(t) = LI(t)$ and Eq. (2.3) are used.

Next, we introduce the Josephson junction, a key element in superconducting quantum circuits. The Josephson junction [6] consists of weakly coupled two superconductors separated by an insulator (S/I/S junction). For superconducting qubits, as shown in Fig. 2.2, the S/I/S structure of aluminum-aluminum oxide-aluminum (Al/AlO$_x$/Al) is currently the mainstream. From the Ginzburg-Landau theory, the state of each superconductor can be represented by the order parameter $\psi_0 e^{-i\theta_{a,b}}$, and a phase difference is $\theta = \theta_a - \theta_b$ between the two superconductors separated by the oxide film. When a wire connects the two ends of the Josephson junction, a current flows depending on the phase difference even if no voltage is applied, which is represented as follows

$$I = I_0 \sin\theta. \tag{2.6}$$

This is called the DC Josephson effect. Here, I_0 is called the critical current. When a current above I_0 flows the Josephson junction, it deviates from the Eq. (2.6) and resistance appears, or hysteresis is observed in the vicinity of I_0. On the other hand, when an external circuit is connected to the Josephson junction to change the phase difference in time, a voltage difference is induced at both ends of the Josephson junction, as expressed by the following equation.

$$V = \frac{\hbar}{2e}\frac{d\theta}{dt}. \tag{2.7}$$

This is called the AC Josephson effect. Assuming that the current flowing through the junction is less than I_0 and the voltage across the junction is V, the energy stored in a Josephson junction can be expressed as follows

$$E_{\mathrm{JJ}}(t) = \int_{-\infty}^{t} I(\tau)V(\tau)d\tau = \int_{-\infty}^{t} \frac{I_0\hbar}{2e}\sin\theta\frac{d\theta}{d\tau}d\tau,$$
$$= E_{\mathrm{J}}(1 - \cos\theta), \tag{2.8}$$

where E_{J} is called the Josephson energy and $E_{\mathrm{J}} = \frac{I_0\hbar}{2e}$.
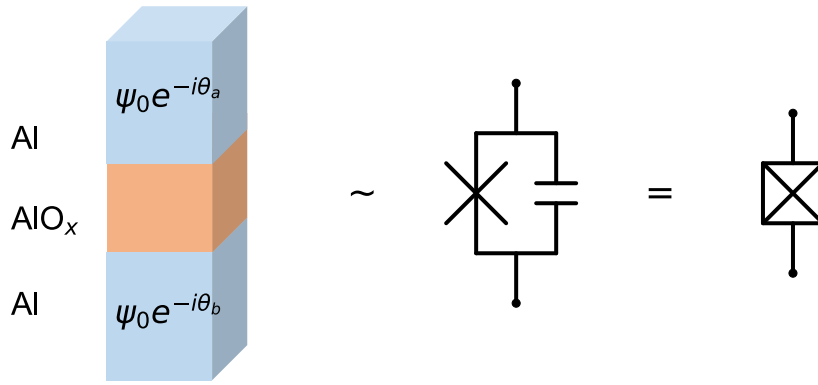
Figure 2.2: Schematic of Josephson junction (left). The junction has parallel capacitance due to the structure of the oxide layer sandwiched between the superconductors (center). The schematic diagram of a Josephson junction with capacitance is often used, as shown in the symbol (right).

2.2 Kirchhoff's current and voltage law

To investigate the time evolution of the current and stored charge in each element of a given circuit, it is sufficient to obtain circuit equations for the circuit, which correspond to the equations of motion in classical mechanics. Kirchhoff's current and voltage laws (KCL and KVL) are the main tools for obtaining these equations. This section will explain how these laws are expressed for arbitrary circuits composed of the elements introduced in Fig. 2.1.

First, as shown in Fig. 2.3(a), considering the current conservation law for a certain node N_i, the sum of the current flowing in and out at a certain time t must be equal, and the following relationship holds for these currents

$$\sum_{k \in \{a,b,c,\dots\}} \pm I_k(t) = 0. \tag{2.9}$$

This is Kirchhoff's current law, which corresponds to the circuit equation for the node N_i.

We next consider a closed loop shown in Fig. 2.3(b). A magnetic field, denoted by the flux density Φ_{ext}, is applied to this loop. By applying Maxwell-Faraday's law $\nabla \times \boldsymbol{E} = -\frac{\partial \boldsymbol{B}}{\partial t}$ to this loop and integrating both sides with the area S, we obtain the following equation

$$\int\int_S \nabla \times \boldsymbol{E}(t,l) \cdot d\boldsymbol{s} = -\int\int_S \frac{\partial \boldsymbol{B}(t,l)}{\partial t} \cdot d\boldsymbol{s}, \tag{2.10}$$

where l is the coordinate defined on the loop. $\boldsymbol{E}(t,l)$ and $\boldsymbol{B}(t,l)$ are the electric and magnetic fields of each branch, respectively. From Stokes' theorem, we can rewrite the left-hand side of Eq. (2.10) as follows

$$\int\int_S \nabla \times \boldsymbol{E}(t,l) \cdot d\boldsymbol{s} = \oint_C \boldsymbol{E}(t,l) \cdot d\boldsymbol{l}. \tag{2.11}$$

Since the right-hand side of this equation corresponds to a summation of the voltage along with the loop, we can obtain the following equation

$$\oint_C \boldsymbol{E}(t,l) \cdot d\boldsymbol{l} = \sum_{k \in loop_m} \mp V_k(t). \tag{2.12}$$

(a)   (b)
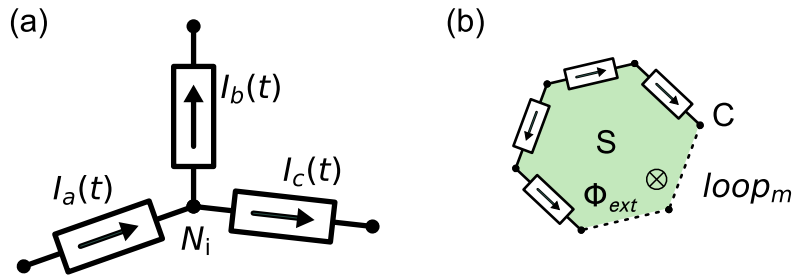
Figure 2.3: (a) Example of a node (N_i) to which KCL is applied. Currents $I_a(t)$, $I_b(t)$, and $I_c(t)$ flow out or in, respectively, according to the arrows. (b) Example of a loop to which KVL is applied. A closed $loop_m$ is formed by several circuit elements and is penetrated by an external magnetic flux Φ_{ext}. C and S are the line-integral path and the area-integral region, respectively.

Additionally, by performing area integration on the right-hand side of Eq. (2.10), we obtain the following equation

$$-\int\int_{\text{S}} \frac{\partial \boldsymbol{B}(t,l)}{\partial t} \cdot d\boldsymbol{s} = -\frac{\partial}{\partial t}\Phi_{\text{ext}}(t). \tag{2.13}$$

Using Eqs. (2.12) and (2.13), we obtain KVL as follows

$$\sum_{k\in loop_m} \mp V_k(t) = -\frac{\partial}{\partial t}\Phi_{\text{ext}}(t). \tag{2.14}$$

Also, in terms of the flux variables, we have the following equation

$$\sum_{k\in loop_m} \pm\Phi_k(t) = \Phi_{\text{ext}}(t) + A. \tag{2.15}$$

Furthermore, considering the loop consists of the superconducting material, the integration constant is limited as follows

$$\sum_{k\in loop_m} \pm\Phi_k(t) - \Phi_{\text{ext}}(t) = N\Phi_0. \tag{2.16}$$

where $\Phi_0 = \frac{h}{2e}$ is the magnetic flux quantum. This equation expresses a set of holonomic constraints for the generalized coordinates when finding a circuit Lagrangian with minimal dynamical variables. Hereafter, the time dependence of circuit variables such as $\Phi(t), I(t)$ and $V(t)$ will be omitted and written as Φ, I and V.

2.3 Circuit quantization

2.3.1 LC resonator

First, we consider the circuit quantization of an LC resonator shown in Fig. 2.4. Applying KCL to the node N_1, we obtain a circuit equation as follows

$$\frac{\Phi_a}{L} + C\ddot{\Phi}_a = 0, \tag{2.17}$$

where KVL, $\Phi_a - \Phi_b = 0$, is used. There are correspondences between F and $-\Phi_a/L$, and ma and $C\ddot{\Phi}_a$ when compared with the equation of motion $F = ma$. Furthermore,
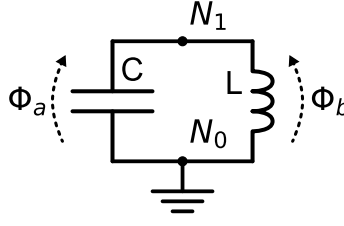
Figure 2.4: Circuit schematics of an LC resonator, which consists of two nodes (N_0, N_1), a capacitance branch (C, Φ_a), and an inductance branch (L, Φ_b).

the work done by the force $-\Phi_a/L$ is found to be path-independent and conservative and can be regarded as the motion of a particle of mass C in a potential U, which is given by

$$U = -\int_0^{\Phi_a} F d\Phi' = \frac{\Phi_a^2}{2L}. \tag{2.18}$$

The kinetic energy is $\frac{C}{2}\dot{\Phi}_a^2$ and the Lagrangian is found to be

$$\mathcal{L}_{\mathrm{LC}} = T - U = \frac{C}{2}\dot{\Phi}_a^2 - \frac{\Phi_a^2}{2L}. \tag{2.19}$$

Substituting Eq. (2.19) to Euler-Lagrange equation, Eq. (2.17) will be reproduced. From the Legendre transformation

$$\mathcal{H} \equiv \sum_i \frac{\partial \mathcal{L}}{\partial \dot{q}_i} \dot{q}_i - \mathcal{L}, \tag{2.20}$$

we can obtain the classical Hamiltonian of the LC resonator as follows

$$\mathcal{H}_{\mathrm{LC}} = \frac{Q^2}{2C} + \frac{\Phi^2}{2L}. \tag{2.21}$$

Here, $Q = \frac{\partial \mathcal{L}_{\mathrm{LC}}}{\partial \dot{\Phi}_a} = C\dot{\Phi}_a$ and $\Phi_a = \Phi$. To obtain a quantum Hamiltonian, we introduce non-commuting magnetic flux and charge operators and rewrite the classical one as follows

$$\Phi \longrightarrow \hat{\Phi}, \tag{2.22}$$

$$Q \longrightarrow \hat{Q}, \tag{2.23}$$

$$i\hbar = [\hat{\Phi}, \hat{Q}]. \tag{2.24}$$

Finally, we obtain the quantum Hamiltonian of the LC resonator

$$\hat{\mathcal{H}}_{\mathrm{LC}} = \frac{\hat{Q}^2}{2C} + \frac{\hat{\Phi}^2}{2L}. \tag{2.25}$$

Furthermore, from the harmonic oscillator analogy, the magnetic flux and charge operators can be rewritten using the creation and annihilation operators as follows

$$\hat{Q} = \sqrt{\frac{\hbar\omega C}{2}}(\hat{a}^\dagger + \hat{a}) = \sqrt{\frac{\hbar}{2Z}}(\hat{a}^\dagger + \hat{a}), \tag{2.26}$$

$$\hat{\Phi} = i\sqrt{\frac{\hbar}{2\omega C}}(\hat{a}^\dagger - \hat{a}) = i\sqrt{\frac{\hbar Z}{2}}(\hat{a}^\dagger - \hat{a}), \tag{2.27}$$

where $Z = \sqrt{L/C}$ is used. Substituting Eqs. (2.26) and (2.27), we can rewrite Eq. (2.25) as follows

$$\hat{\mathcal{H}}_{\mathrm{LC}} = \hbar\omega\left(\hat{n} + \frac{1}{2}\right). \tag{2.28}$$
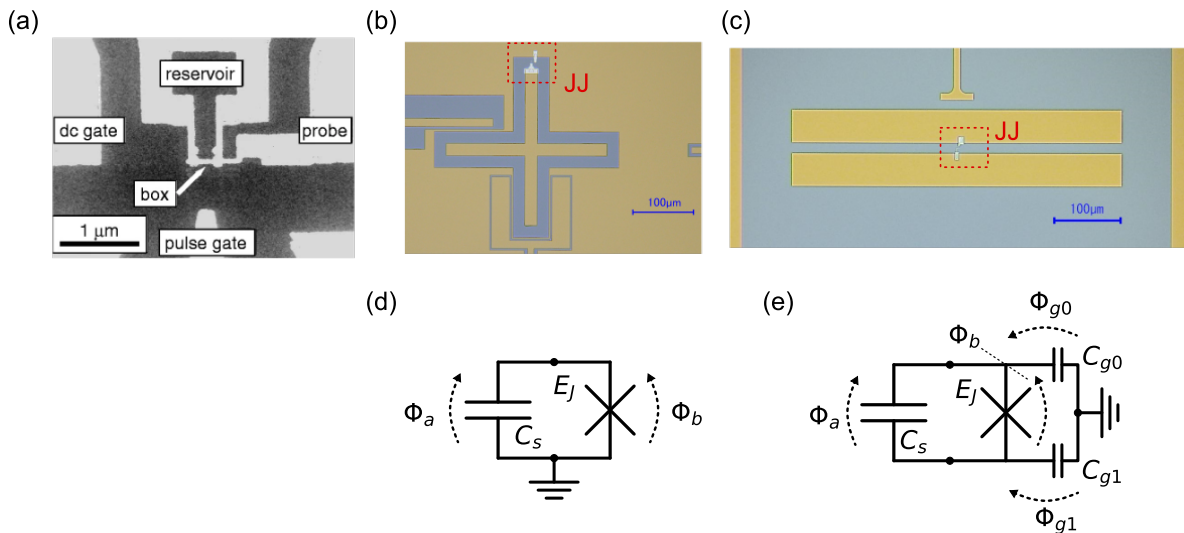
Figure 2.5: (a-c) Sample images of a Cooper-pair box (CPB) [4], a single-end trans-mon (Xmon) [8], and a floating transmon, respectively. (d) Simplified equivalent circuit schematics of the CPB and single-end transmon. The Josephson junction (JJ) is directly connected to the ground and shunted by the capacitor (C_s). (e) Simplified equivalent circuit schematics of the floating transmon. JJ is floating and shunted by C_s. Each rectangle electrode also has capacitance to the ground (C_{g0}, C_{g1}). In addition, branch fluxes ($\Phi_a, \cdots, \Phi_{g1}$) are assigned to branches in each schematic.

2.3.2   Cooper-pair box and transmon

Charge qubit, so-called Cooper-pair box (CPB) shown in Fig. 2.5(a), is one type of the earliest superconducting qubit realized by the NEC group in 1999 [4]. At that time, the coherence time of CPBs was very short, around 1 ns. Still, several years after this invention, a transmon-type superconducting qubit (transmon) shown in Fig. 2.5(b,c) was proposed [7], which could have a longer lifetime by changing design parameters and has been used to today.

First, we consider the CPB or single-end transmon circuit shown in Fig. 2.5(d). By collecting kinetic and potential energies, we obtain the following Lagrangian

$$\mathcal{L}_{\mathrm{CPB}} = \frac{C_s}{2}\dot{\Phi}^2 + E_J \cos{(\Phi/\phi_0)}, \tag{2.29}$$

where the KVL of $\Phi_a = \Phi_b \equiv \Phi$ is used, and we ignore the constant in the potential energy of the Josephson junction in Eq. (2.8). Note that, the phase of the superconductor ϕ and the magnetic flux Φ are related through the following equation obtained from Eqs. (2.1) and (2.7):

$$\Phi = \frac{\hbar}{2e}\phi = \phi_0\phi. \tag{2.30}$$

Here, $\phi_0 = \Phi_0/2\pi$ is called the reduced magnetic flux quantum. Applying the Legendre transformation to this equation, we obtain the classical Hamiltonian of the circuit

$$\mathcal{H}_{\mathrm{CPB}} = \frac{C_s\phi_0^2}{2}\dot{\phi}^2 + E_J \cos\phi, \tag{2.31}$$

where $\phi = \Phi/\phi_0$ is used. Using Eq. (2.1), we now introduce a generalized variable normalized by the charge of the Cooper pair

$$N = \frac{Q}{2e} = \frac{C_s}{2e}\phi_0\dot{\phi}. \tag{2.32}$$

Substituting this equation to Eq. (2.31), we obtain the equation as follows

$$\mathcal{H}_{\text{CPB}} = 4E_{C_s} N^2 - E_J \cos \phi, \tag{2.33}$$

where $E_{C_s} = \frac{e^2}{2C_s}$ is the charging energy of the shunt capacitor.

Before going to a quantum Hamiltonian, we examine a similar circuit shown in Fig. 2.5(e). We can obtain the following Lagrangian by collecting kinetic and potential energies:

$$\mathcal{L}_{\text{FT}} = \frac{C_s \phi_0^2}{2} \dot{\phi}_a^2 + \frac{C_{g0} \phi_0^2}{2} \dot{\phi}_{g0}^2 + \frac{C_{g1} \phi_0^2}{2} \dot{\phi}_{g1}^2 + E_J \cos \phi_b. \tag{2.34}$$

Using the KVL, we can rewrite this equation as follows

$$\mathcal{L}_{\text{FT}} = \frac{C_s \phi_0^2}{2} \dot{\phi}^2 + \frac{C_{g0} \phi_0^2}{2} \dot{\phi}_{g0}^2 + \frac{C_{g1} \phi_0^2}{2} \left(-\dot{\phi} + \dot{\phi}_{g0} \right)^2 + E_J \cos \phi. \tag{2.35}$$

Here, $\Phi_a / \phi_0 = \Phi_b / \phi_0 \equiv \phi$. In this Hamiltonian, the generalized coordinate ϕ_{g0} is a cyclic coordinate, meaning that its derivative $\dot{\phi}_{g0}$ is the only component included in the Lagrangian, i.e., $\frac{\partial \mathcal{L}_{\text{FT}}}{\partial \phi_{g0}} = 0$. As a result, the Euler-Lagrange equation

$$\frac{d}{dt} \frac{\partial \mathcal{L}}{\partial \dot{q}_j} = \frac{\partial \mathcal{L}}{\partial q_j}, \ (j = 1, 2, \ldots, n) \tag{2.36}$$

leads to the following relation for the generalized momentum

$$\frac{\partial \mathcal{L}_{\text{FT}}}{\partial \dot{\phi}_{g0}} = \phi_0^2 \left\{ (C_{g0} + C_{g1}) \dot{\phi}_{g0} - C_{g1} \dot{\phi} \right\} = A(constant). \tag{2.37}$$

Solving this equation for $\dot{\phi}_{g0}$ and substituting it into Eq. (2.35) yields the following Lagrangian

$$\mathcal{L}_{\text{FT}} = \frac{C' \phi_0^2}{2} \dot{\phi}^2 + E_J \cos \phi + \frac{A^2}{2\phi_0^2 (C_{g0} + C_{g1})}, \tag{2.38}$$

where $C' = C_s + C_{g0} C_{g1} / (C_{g0} + C_{g1})$. Therefore, we can decouple the dynamics of ϕ_{g0} from the system of interest. Henceforth, we ignore the last constant term. Applying the Legendre transformation, we obtain the classical Hamiltonian for the floating transmon

$$\mathcal{H}_{\text{FT}} = 4E_{C'} N'^2 - E_J \cos \phi, \tag{2.39}$$

where $N' = \frac{1}{2e} \frac{\partial \mathcal{L}_{\text{FT}}}{\partial \dot{\phi}}$ and $E_{C'} = \frac{e^2}{2C'}$. Finally, we can derive the same form as in Eq. (2.33). From here, we use Eq. (2.33) for the following discussion. Depending on the situation, one can apply similar discussions by replacing E_C with E'_C. We introduce the non-commuting phase and number operators and rewrite the classical one as follows

$$\phi \longrightarrow \hat{\phi}, \tag{2.40}$$

$$N \longrightarrow \hat{N}, \tag{2.41}$$

$$i = [\hat{\phi}, \hat{N}]. \tag{2.42}$$

Then, we obtain the quantum charge qubit Hamiltonian

$$\hat{\mathcal{H}}_{\text{CQ}} = 4E_C \hat{N}^2 - E_J \cos \hat{\phi}. \tag{2.43}$$

So far, we have not considered the DC gate voltage in Fig. 2.5(a). This effect can be understood as the Cooper pair difference depending on the voltage, and the Hamiltonian is rewritten as follows [7]

$$\hat{\mathcal{H}}_{\text{CQ}} = 4E_C \left(\hat{N} - N_g \right)^2 - E_J \cos \hat{\phi}, \tag{2.44}$$

where N_g represents the number of Cooper pairs induced by the gate voltage. For the numerical calculations, we introduce the following operators in the charge basis representation [9]:

$$\hat{N} = \sum_{N=-\infty}^{\infty} N|N\rangle\langle N|, \tag{2.45}$$

$$\cos\hat{\phi} = \frac{1}{2}\sum_{N=-\infty}^{\infty}\left(|N\rangle\langle N+1| + |N+1\rangle\langle N|\right). \tag{2.46}$$

Truncating the dimension of the Hilbert space for numerical calculations, the above operators can be written in the following matrix representations

$$\hat{N} \rightarrow \mathbf{N} = \begin{pmatrix} -n & & \\ & \ddots & \\ & & n \end{pmatrix}, \tag{2.47}$$

$$\cos\hat{\phi} \rightarrow \mathbf{P} = \frac{1}{2}\begin{pmatrix} & 1 & & \\ 1 & & \ddots & \\ & \ddots & & 1 \\ & & 1 & \end{pmatrix}, \tag{2.48}$$

where the Hilbert space dimension is $2n+1$. Regarding computational cost, using a discrete-valued charge basis is preferable to a continuous-valued phase basis. In this thesis, the charge basis is mainly used. However, if one desires to compute the wavefunction in phase space, the following equation

$$|\phi\rangle = \sum_{N=-\infty}^{\infty} e^{iN\phi}|N\rangle \tag{2.49}$$

gives phase-basis wavefunctions. Using Eqs. (2.44), (2.47), and (2.48), we obtain the following charge qubit Hamiltonian as follows

$$\hat{H}_{\mathrm{CQ}} = 4E_C\left(\mathbf{N} - N_g\mathbf{I}\right)^2 - E_J\mathbf{P}. \tag{2.50}$$

Here, $\mathbf{I}$ represents the identity operator. The energy spectrum of the charge qubit is calculated by numerically diagonalizing the Hamiltonian. Fig. 2.6 shows the results, obtained by changing E_C while keeping $E_J = 15$ GHz. Usually, the two lowest energy levels are used as a qubit, whereas Fig. 2.6(a) shows that the first excited state energy changes with the charge bias when E_J/E_C is small. This frequency tunability acts as a path of charge noise propagation channel and decreases a phase coherence time T_2. Increasing a ratio E_J/E_C, the dephasing induced by the charge noise can be suppressed according to the following equation [7]

$$T_2 \sim \frac{1}{\sqrt{\delta f_{01}^2}} \propto \exp\left(\sqrt{\frac{2E_J}{E_C}}\right), \tag{2.51}$$

where δf_{01}^2 is the variance of the frequency difference between the ground and first excited states of the charge qubit, and this is the main reason for the poor performance of the early charge qubits. In addition, Eq. (2.51) shows that increasing E_J/E_C exponentially increases the phase coherence time, and a charge qubit designed in this regime is called the transmon [7], and typical E_J/E_C is 40–70.
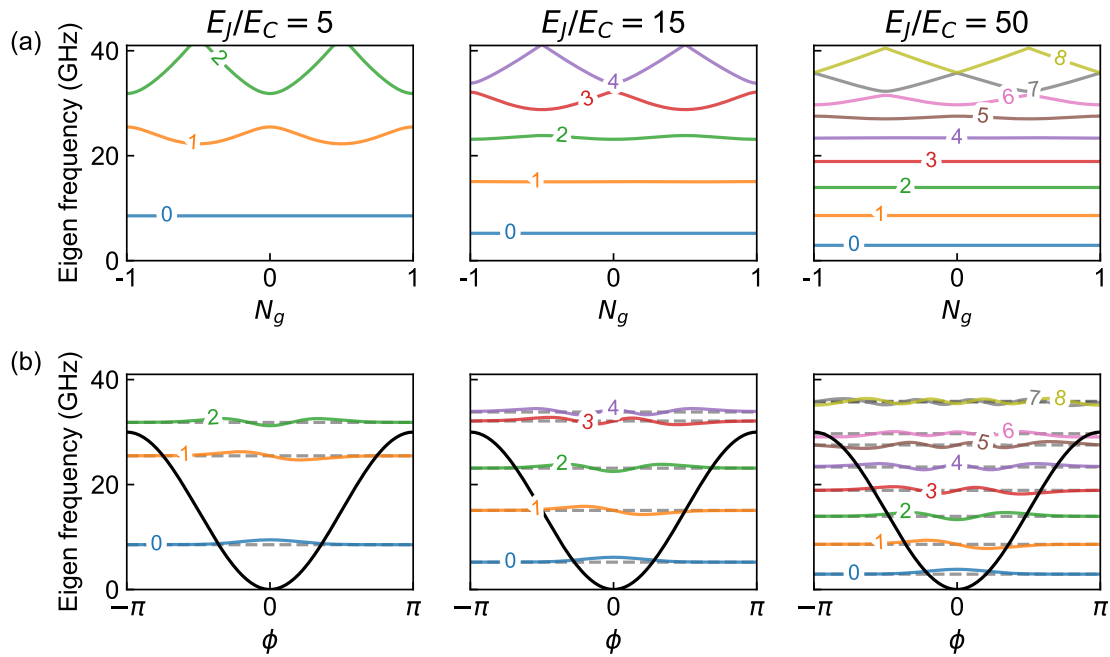
Figure 2.6: (a) Offset charge-dependent spectrum of charge qubits, and E_C is swept from left to right as 3.0, 1.0, and 0.3 GHz with fixed $E_J = 15$ GHz. (b) Eigenvalues (dashed holizontal lines) and real part of wavefunctions (colord solid lines) in the phase basis representation at $N_g = 0$. The black solid line shows the cosine potential of the Josephson junction with $E_J = 15$ GHz. The inline numbers are the eigenvalue numbers in ascending order of energy.

In the transmon regime, as shown in Fig. 2.6(b), $\hat{\phi}$ is well localized around the potential minima for the lower eigenstates, and thanks to this localization, the Taylor expansion of Eq. (2.43) for $\hat{\phi}$ becomes a good approximation of the original one as follows

$$\hat{\mathcal{H}}_{\mathrm{CQ}} \approx 4E_C\hat{N}^2 + \frac{E_J}{2}\hat{\phi}^2 - \frac{E_J}{24}\hat{\phi}^4, \tag{2.52}$$

where we consider up to the fourth-order terms. Limited to the case of small excitation numbers, $\hat{\phi}$ can be regarded as an operator with continuous rather than periodic real eigenvalues and can be further rewritten using the creation and annihilation operators as follows

$$\hat{\mathcal{H}}'_{\mathrm{CQ}} = \sqrt{8E_C E_J}\,\hat{b}^\dagger\hat{b} - \frac{E_C}{12}\left(\hat{b}^\dagger + \hat{b}\right)^4, \tag{2.53}$$

$$\approx \hbar\omega_q\hat{b}^\dagger\hat{b} - \frac{E_C}{2}\hat{b}^\dagger\hat{b}^\dagger\hat{b}\hat{b}, \tag{2.54}$$

where $\hbar\omega_q = \sqrt{8E_C E_J} - E_C$. For the second line, the rotating-wave approximation is used, and we introduced the following equations

$$\hat{N} = \frac{i}{2}\left(\frac{E_J}{2E_C}\right)^{1/4}\left(\hat{b}^\dagger - \hat{b}\right), \tag{2.55}$$

$$\hat{\phi} = \left(\frac{2E_C}{E_J}\right)^{1/4}\left(\hat{b}^\dagger + \hat{b}\right). \tag{2.56}$$

2.3.3 Cubic transmon

Cubic transmon shown in Fig. 2.7(a) is one of the superconducting qubits proposed and experimentally demonstrated by Noguchi *et al.* in 2019 [10], which replaced the Josephson

junction of the ordinary transmon with the SNAIL shown in Fig. 2.7(b). In this thesis, the cubic transmon is an important element for implementing a qubit-conditional operation for a resonator. Thus, we introduce a Hamiltonian model of the floating type cubic transmon. Similar to the floating type transmon, collecting the energy of each branch shown in Fig. 2.7(c), the circuit Lagrangian can be written as follows

$$
\begin{aligned}
\mathcal{L}_{\mathrm{CT}} = {} & \frac{C_s}{2}\dot{\Phi}_1^2 + \frac{C_{J2}}{2}\dot{\Phi}_2^2 + \frac{C_{J3}}{2}\dot{\Phi}_3^2 \\
& + \frac{C_{g1}}{2}\dot{\Phi}_{g1}^2 + \frac{C_{g2}}{2}\dot{\Phi}_{g2}^2 + \frac{C_{g3}}{2}\dot{\Phi}_{g3}^2 \\
& + E_{J1}\cos\left(\Phi_1/\phi_0\right) + E_{J2}\cos\left(\Phi_2/\phi_0\right) + E_{J3}\cos\left(\Phi_3/\phi_0\right).
\end{aligned}
\tag{2.57}
$$

Applying KVL to the three loops labeled 1 to 3 shown in Fig. 2.7(c), we can rewrite the above equation as follows

$$
\begin{aligned}
\mathcal{L}_{\mathrm{CT}} = {} & \frac{C_s\phi_0^2}{2}\dot{\phi}_1^2 + \frac{C_{J2}\phi_0^2}{2}\dot{\phi}_2^2 + \frac{C_{J3}\phi_0^2}{2}\left(\dot{\phi}_1 - \dot{\phi}_2\right)^2 \\
& + \frac{C_{g1}\phi_0^2}{2}\left(\dot{\phi}_1 + \dot{\phi}_{g2}\right)^2 + \frac{C_{g2}\phi_0^2}{2}\dot{\phi}_{g2}^2 + \frac{C_{g3}\phi_0^2}{2}\left(\dot{\phi}_2 + \dot{\phi}_{g2}\right)^2 \\
& + E_{J1}\cos\phi_1 + E_{J2}\cos\phi_2 + E_{J3}\cos\left(\phi_1 - \phi_2 - \phi_e\right),
\end{aligned}
\tag{2.58}
$$

where $\Phi_i/\phi_0 \equiv \phi_i$, $i \in (1,2,3,g1,g2,g3)$ and $\Phi_{\mathrm{ext}}/\phi_0 \equiv \phi_e$ are used. Following the same approach as the floating transmon, we can decouple the cyclic coordinate ϕ_{g2} from the system dynamics and obtain the following classical Hamiltonian by the Legendre transformation

$$
\begin{aligned}
\mathcal{H}_{\mathrm{CT}} = {} & 4E_{C_1}N_1^2 + 4E_{C_2}N_2^2 + 8E_{C_{12}}N_1N_2 \\
& - E_{J1}\cos\phi_1 - E_{J2}\cos\phi_2 - E_{J3}\cos\left(\phi_1 - \phi_2 - \phi_e\right).
\end{aligned}
\tag{2.59}
$$

In general, E_{C_1}, E_{C_2}, and $E_{C_{12}}$ have complicated expressions. Assuming $C_{J3} = C_{J2}$ and $C_{g2} = C_{g1}$, we can simplify E_{C_1}, E_{C_2}, and $E_{C_{12}}$ as follows

$$
E_{C_1} = 2E_{C_{12}} = \frac{e^2}{2C_S + C_{J2} + C_{g1}},
\tag{2.60}
$$

$$
E_{C_2} = \frac{e^2\left(2C_SC_{g1} + C_SC_{g3} + 2C_{J2}C_{g1} + C_{J2}C_{g3} + C_{g1}^2 + C_{g1}C_{g3}\right)}{(2C_S + C_{J2} + C_{g1})(2C_{J2}C_{g1} + C_{J2}C_{g3} + C_{g1}C_{g3})}.
\tag{2.61}
$$

These equations are instructive when we design a cubic transmon. We also introduce the non-commuting phase and number operators and rewrite the classical ones as follows

$$
\phi_1 \longrightarrow \hat{\phi}_1,
\tag{2.62}
$$

$$
\phi_2 \longrightarrow \hat{\phi}_2,
\tag{2.63}
$$

$$
N_1 \longrightarrow \hat{N}_1,
\tag{2.64}
$$

$$
N_2 \longrightarrow \hat{N}_2,
\tag{2.65}
$$

$$
i = [\hat{\phi}_1, \hat{N}_1],
\tag{2.66}
$$

$$
i = [\hat{\phi}_2, \hat{N}_2].
\tag{2.67}
$$

Then, we obtain the quantum cubic transmon Hamiltonian

$$
\begin{aligned}
\hat{\mathcal{H}}_{\mathrm{CT}} = {} & 4E_{C_1}\hat{N}_1^2 + 4E_{C_2}\hat{N}_2^2 + 8E_{C_{12}}\hat{N}_1\hat{N}_2 \\
& - E_{J1}\cos\hat{\phi}_1 - E_{J2}\cos\hat{\phi}_2 - E_{J3}\cos\left(\hat{\phi}_1 - \hat{\phi}_2 - \phi_e\right).
\end{aligned}
\tag{2.68}
$$

(a)

(b)

(c)
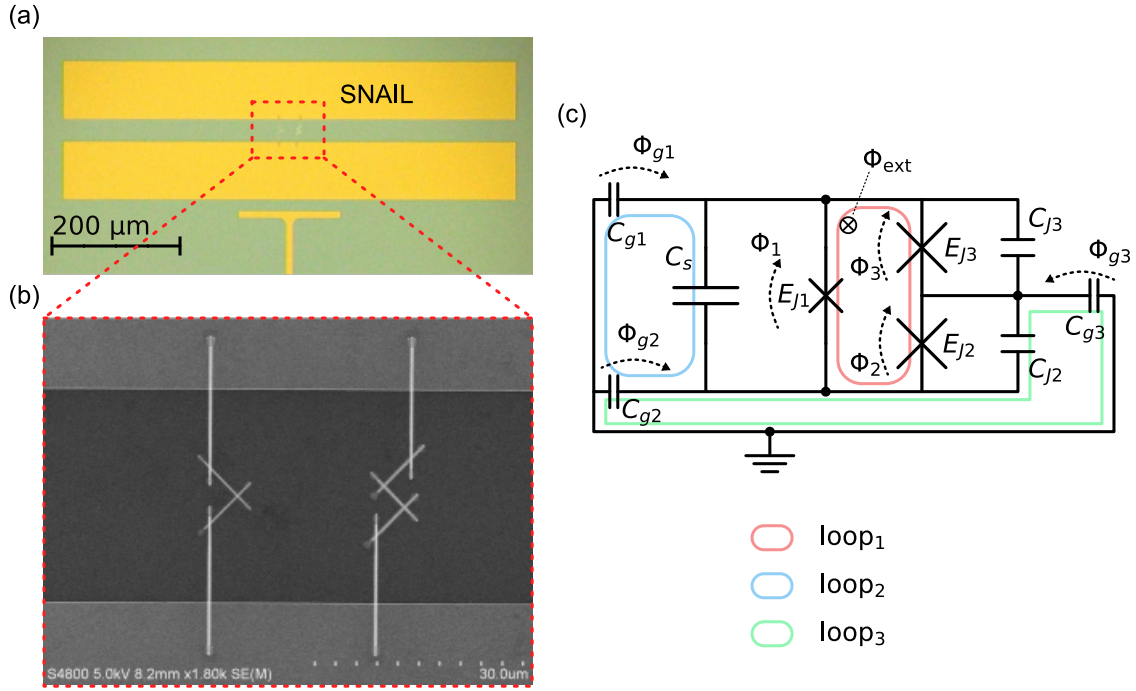
Figure 2.7: (a) Optical image of a cubic transmon. In contrast to the literature [10], the floating type is used here. (b) Scanning electron micrograph of the SNAIL. (c) Equivalent circuit schematics of the floating cubic transmon. The SNAIL is floating and shunted by C_s, including a junction capacitance C_{J1} (not shown). Rectangle electrodes and an island between two Josephson junctions have capacitances to the ground (C_{g1}, C_{g2}, C_{g3}). In addition, branch fluxes ($\Phi_1, \cdots, \Phi_{g3}$) are assigned to branches in each schematic. For loops that include a Josephson junction and do not include a capacitor to the ground, KVL has already been applied to reduce the number of variables. In contrast, for the three loops labeled 1 to 3, KVL has not yet been applied. Φ_{ext} indicates the applied external magnetic flux density.
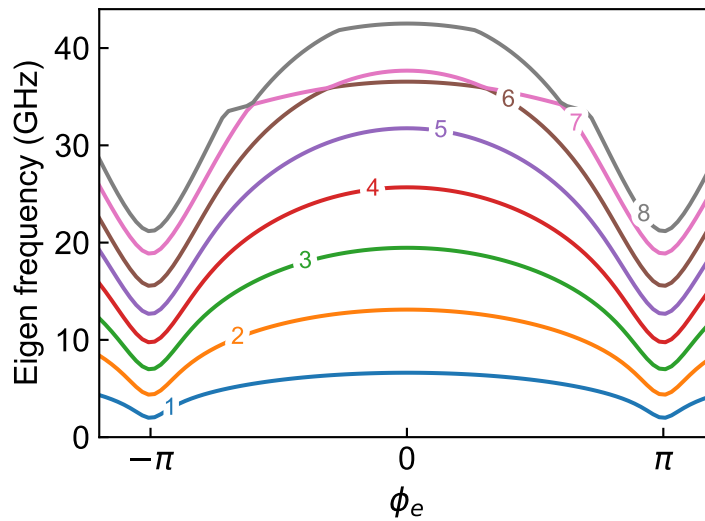
Figure 2.8: (a) Eigen energies of the cubic transmon depending on the external magnetic field via ϕ_e. The inline numbers are the eigenvalue numbers from the lowest energy to the highest. We set $n_{1,2} = 10$, $E_{J1} = 14$ GHz, $E_{J2} = E_{J3} = 2.5 \times 14$ GHz, and $E_{C_i} = (0.2, 3, 0.2)$ GHz for $i = (1, 2, 12)$.

As in the case of the transmon, the behavior of the energy spectrum is calculated numerically by solving the following Hamiltonian

$$\begin{aligned}
\hat{\mathcal{H}}_{\text{CT}} = {} & 4E_{C_1}\mathbf{N}_1^2 \otimes \mathbf{I}_2 - E_{J1}\mathbf{P}_1 \otimes \mathbf{I}_2 \\
& + 4E_{C_2}\mathbf{I}_1 \otimes \mathbf{N}_2^2 - E_{J2}\mathbf{I}_1 \otimes \mathbf{P}_2 \\
& + 8E_{C_{12}}\mathbf{N}_1 \otimes \mathbf{N}_2 - E_{J3}\cos\left(-\phi_e\right)\mathbf{P}_1 \otimes \mathbf{P}_2^\dagger.
\end{aligned} \tag{2.69}$$

Here, $\mathbf{I}_1$ and $\mathbf{I}_2$ are the identity operators in each subspace. The example of diagonalization results is shown in Fig. 2.8. Next, Fig. 2.9 shows the behavior of the wave function in each representation under the external magnetic flux $\phi_e = 0.2$ as an example. The function shapes for the lowest three energy states are similar to those of the transmon along the tilted axis $2\phi_2 = \phi_1 - \phi_e$. Therefore, a one-dimensional approximation along this axis is valid for the low-energy subspace, and the constraint of $2\phi_2 = \phi_1 - \phi_e$ is called the single-flux approximation [10, 11]. Under this approximation, the potential form in Eq. (2.68) is rewritten as follows

$$\hat{U}_{\text{SNAIL}}(\hat{\phi}_1, \phi_e) = -E_{J1}\cos\hat{\phi}_1 - 2aE_{J1}\cos\left(\frac{\hat{\phi}_1 - \phi_e}{2}\right), \tag{2.70}$$

where we assume $E_{J2} = E_{J3}$, $a = E_{J2}/E_{J1}$. Suppose the environment is cool enough compared to the first excited state energy of the cubic transmon. The cubic transmon state should be around the potential minima under a static magnetic field, and the phase that gives the potential minima is obtained by solving the following equation

$$\left.\frac{d\hat{U}_{\text{SNAIL}}}{d\hat{\phi}_1}\right|_{\phi_{\min}} = 0. \tag{2.71}$$

Therefore, we redefine the phase operator as the displacement from the minima of the SNAIL potential as follows

$$\hat{\delta}_1 \equiv \hat{\phi}_1 - \phi_{\min}. \tag{2.72}$$

This new operator satisfies the same commutation relation as the original operator:

$$[\hat{\phi}_1, \hat{N}_1] = [\hat{\delta}_1, \hat{N}_1] = i. \tag{2.73}$$

Applying Taylor expansion to the SNAIL potential, we obtain the effective cubic transmon Hamiltonian as follows

$$\hat{\mathcal{H}}'_{\text{CT}} = 4E_{C_1}\hat{N}_1 + c_2\hat{\delta}_1^2 + c_3\hat{\delta}_1^3 + c_4\hat{\delta}_1^4 + \mathcal{O}(\hat{\delta}_1^5), \tag{2.74}$$

where c_n is the Taylor coefficient and calculated as follows

$$c_n = \left.\frac{d^n U_{\text{SNAIL}}}{d\hat{\phi}_1^n}\right|_{\phi_{\min},\phi_e} \tag{2.75}$$

As in the case of transmon, we introduce the following transformations

$$\hat{N}_1 = N_{1,\text{zpf}}\left(\hat{b}^\dagger - \hat{b}\right) = \frac{i}{2}\left(\frac{c_2}{E_{C_1}}\right)^{1/4}\left(\hat{b}^\dagger - \hat{b}\right), \tag{2.76}$$

$$\hat{\delta}_1 = \delta_{1,\text{zpf}}\left(\hat{b}^\dagger - \hat{b}\right) = \left(\frac{E_{C_1}}{c_2}\right)^{1/4}\left(\hat{b}^\dagger + \hat{b}\right), \tag{2.77}$$
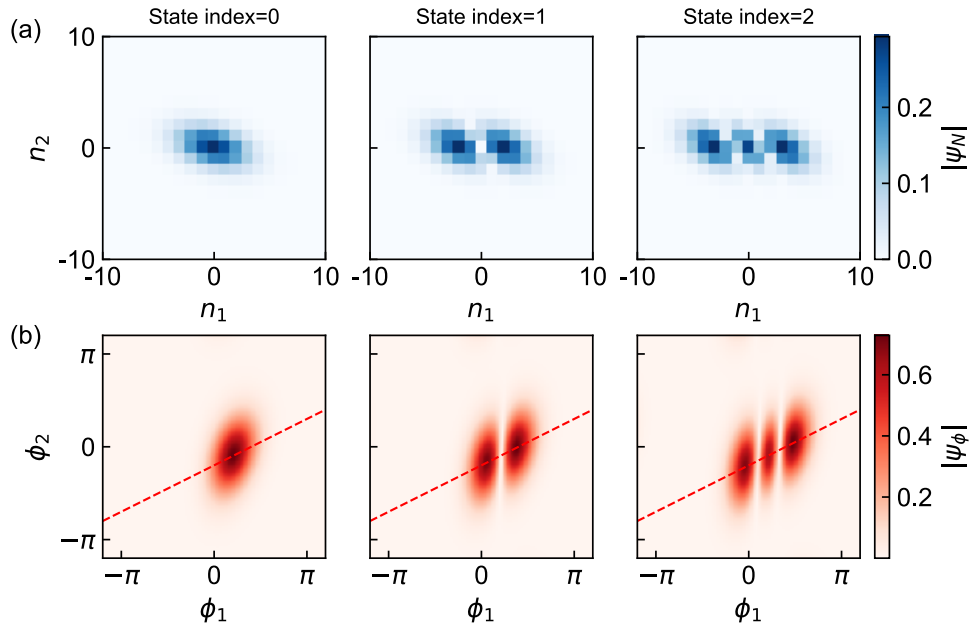
Figure 2.9: Wave functions in the charge (a) and phase (b) basis with $\phi_e = 2\pi \times 0.2$ for the lowest three energy states. The red dashed lines show the condition of $2\phi_2 = \phi_1 - \phi_e$.

and the effective Hamiltonian is further rewritten as follows

$$\hat{\mathcal{H}}_{\mathrm{CT}}^{\mathrm{eff}} = \sqrt{16 E_{C_1} c_2} \hat{b}^\dagger \hat{b} + c_3 \delta_{1,\mathrm{zpf}}^3 \left(\hat{b}^\dagger + \hat{b} \right)^3 + c_4 \delta_{1,\mathrm{zpf}}^4 \left(\hat{b}^\dagger + \hat{b} \right)^4, \tag{2.78}$$

$$= \hbar \omega_{\mathrm{CT}} \hat{b}^\dagger \hat{b} + g_3 \left(\hat{b}^\dagger + \hat{b} \right)^3 + g_4 \left(\hat{b}^\dagger + \hat{b} \right)^4. \tag{2.79}$$

This Hamiltonian well characterizes the cubic transmon. When subjected to microwave irradiation, the second term in the equation represents the origin of the second-order nonlinearity. On the other hand, the third term represents the third-order nonlinearity, which enables the cubic transmon to function as a qubit by generating a self-Kerr effect.

2.3.4 Composite system : Transmon + LC resonator

The transmon-resonator composite system illustrated in Fig. 2.10 is indispensable in circuit-QED experiments. In this context, we will derive the quantum Hamiltonian of the system. As usual, the Lagrangian is obtained by collecting the energy of the circuit as follows

$$\mathcal{L}_{\mathrm{RQ}} = \frac{C + C_{12}}{2} \dot{\Phi}_1^2 + \frac{C_{\mathrm{S}} + C_{12}}{2} \dot{\Phi}_2^2 - C_{12} \dot{\Phi}_1 \dot{\Phi}_2 - \frac{\Phi_1^2}{2L} + E_J \cos\left(\Phi_2 / \phi_0\right). \tag{2.80}$$

The generalized momentums are as follows

$$Q_1 = (C + C_{12})\dot{\Phi}_1 - C_{12}\dot{\Phi}_2, \tag{2.81}$$

$$Q_2 = (C_{\mathrm{S}} + C_{12})\dot{\Phi}_2 - C_{12}\dot{\Phi}_1. \tag{2.82}$$

Using them and Legendre transformation, we obtain the following Hamiltonian

$$\mathcal{H}_{\mathrm{RQ}} = \frac{Q_1^2}{2C_r} + \frac{\Phi_1^2}{2L} + \frac{Q_2^2}{2C_q} - E_J \cos\left(\Phi_2 / \phi_0\right) + \frac{Q_1 Q_2}{C_g}, \tag{2.83}$$
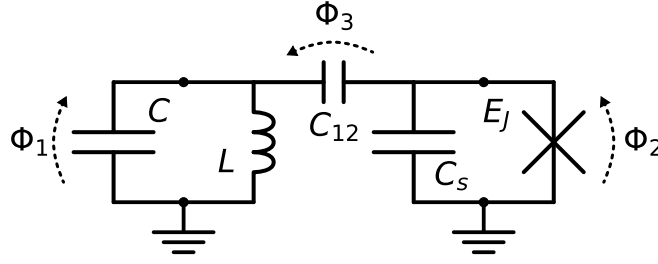
Figure 2.10: Composite system schematic of single-end transmon and LC resonator, capacitively coupled through C_{12}. Branch fluxes (Φ_1, Φ_2, Φ_3) are assigned to branches, and KVL has already been applied for two loops to reduce the number of variables.

where

$$C_r = \frac{C(1 + C_{12}/C_{\mathrm{S}} + C_{12}/C)}{1 + C_{12}/C_{\mathrm{S}}}, \tag{2.84}$$

$$C_q = \frac{C_{\mathrm{S}}(1 + C_{12}/C_{\mathrm{S}} + C_{12}/C)}{1 + C_{12}/C}, \tag{2.85}$$

$$C_g = \frac{CC_{\mathrm{S}}(1 + C_{12}/C_{\mathrm{S}} + C_{12}/C)}{C_{12}}. \tag{2.86}$$

Following the quantization procedures of the LC resonator and single-end transmon, we can rewrite Eq. (2.83) and obtain the quantum Hamiltonian as follows

$$\hat{\mathcal{H}}_{\mathrm{RQ}} = \frac{\hat{Q}_1^2}{2C_r} + \frac{\hat{\Phi}_1^2}{2L} + 4E_C\hat{N} - E_J\cos\hat{\phi} + \frac{2e}{C_g}\hat{N}\hat{Q}_1 \tag{2.87}$$

Based on the previous discussions, we can approximate this Hamiltonian using the creation-annihilation operators as follows

$$\hat{\mathcal{H}}_{\mathrm{RQ}} \approx \hbar\omega_r\hat{a}^\dagger\hat{a} + \hbar\omega_q\hat{b}^\dagger\hat{b} - \frac{E_C}{2}\hat{b}^\dagger\hat{b}^\dagger\hat{b}\hat{b} + i\hbar g(\hat{a}^\dagger + \hat{a})(\hat{b}^\dagger - \hat{b}). \tag{2.88}$$

Here, the last term denotes capacitive coupling

$$g = \frac{e}{C_g}\sqrt{\frac{Z_r}{2\hbar}}\left(\frac{E_J}{2E_{C_q}}\right)^{1/4}, \tag{2.89}$$

where $Z_r = \sqrt{L/C_r}$ and $E_{C_q} = e^2/2C_q$. Furthermore, the rotating-wave approximation and the two-level approximation for the transmon result in the following Jaynes-Cummings Hamiltonian

$$\hat{\mathcal{H}}_{\mathrm{JC}} = \hbar\omega_r\hat{a}^\dagger\hat{a} - \frac{\hbar\omega_q}{2}\hat{\sigma}_Z + i\hbar g(\hat{a}^\dagger\hat{\sigma}^- - \hat{a}\hat{\sigma}^+). \tag{2.90}$$

2.4   Basics of quantum control

This section describes the basic quantum control techniques in circuit-QED systems based on the Hamiltonians derived in the previous section.

2.4.1 Microwave driven single-qubit gate

Microwave pulses are generally used to control the state of superconducting qubits, including the transmon. The superconducting qubit must be coupled to an external circuit to irradiate microwave pulses to a qubit. The drive term through the external circuit is modeled as follows [See Appendix. B]

$$\hat{H}'_d = \frac{\hbar\Omega(t)}{2}\left(\hat{b}^\dagger e^{-i(\omega t+\phi)} + \hat{b}e^{i(\omega t+\phi)}\right), \tag{2.91}$$

where ω, $\Omega(t)$, and ϕ represent the microwave drive frequency, the time-varying amplitude, and the phase, respectively. Therefore, from Eq. (2.54), the driven transmon is modeled as follows

$$\hat{H}_{\text{sys}}/\hbar = \omega_q \hat{b}^\dagger \hat{b} + \frac{\alpha}{2}\hat{b}^\dagger \hat{b}^\dagger \hat{b}\hat{b}$$
$$+ \frac{\Omega(t)}{2}\left(\hat{b}^\dagger e^{-i(\omega t+\phi)} + \hat{b}e^{i(\omega t+\phi)}\right), \tag{2.92}$$

where $\alpha = -E_C/\hbar$. Performing the rotating frame transformation with $\hat{R} = e^{-i\omega t\hat{b}^\dagger \hat{b}}$ and the two-level approximation, we obtain the following simplified Hamiltonian

$$\hat{H}_{sys}/\hbar \approx \frac{\Omega(t)}{2}\left(\hat{\sigma}_+ e^{-i\phi} + \hat{\sigma}_- e^{i\phi}\right)$$
$$= \frac{\Omega(t)}{2}\hat{\sigma}_x \cos\phi - \frac{\Omega(t)}{2}\hat{\sigma}_y \sin\phi. \tag{2.93}$$

With the above Hamiltonian, a solution of the Schrödinger equation is following

$$\hat{U}(t, t+T_g) = \exp\left[-i\frac{1}{2}\int_t^{t+T_g}\Omega(\tau)(\hat{\sigma}_x \cos\phi - \hat{\sigma}_y \sin\phi) + d\tau\right]. \tag{2.94}$$

Here, $\phi = 0$ $(\pi/2)$ corresponds to the x(y)-axis rotation on the Bloch sphere.

2.4.2 Dispersive readout

The state readout of a superconducting qubit is performed by irradiating a microwave pulse to a resonator coupled to the superconducting qubit and measuring the phase shift of the reflected microwave pulse; this readout method is called dispersive readout. To understand the dynamics of the dispersive readout, we first derive the effective dispersive Hamiltonian from the Eq. (2.88). For subsequent calculations, we rewrite this equation in an explicit form using the Fock basis of the transmon as follows

$$\hat{H}/\hbar = \underbrace{\omega_r \hat{a}^\dagger \hat{a} + \sum_n \omega_n |n\rangle\langle n|}_{\hat{H}_0} + \underbrace{\sum_k g_{n,n+1}\left(\hat{a}^\dagger|n\rangle\langle n+1| + \hat{a}|n+1\rangle\langle n|\right)}_{\hat{V}}, \tag{2.95}$$

where $\omega_n = \omega_q n + \frac{\alpha}{2}n(n-1)$, $\alpha = -E_C$, and $g_{n,n+1} = g\sqrt{n+1}$ are used. To obtain the diagonalized form, we perform the Schrieffer-Wolff transformation [See Appendix. A.5]. Using the first line of Eq. (A.15), $\hat{S}_1$ is calculated as follows

$$\hat{S}_1 = i\sum_{n=0}\lambda_{n,n+1}\left(\hat{a}^\dagger|n\rangle\langle n+1| + \hat{a}|n+1\rangle\langle n|\right), \tag{2.96}$$

where $\lambda_{n,n+1} = g_{n,n+1}/(\Delta_{n,n+1}+\alpha)$ and $\Delta_{n,n+1} = \omega_{n+1}-\omega_n-\omega_r$. Using the above equation, the first and second line of Eq. (A.15), we obtain the effective dispersive Hamiltonian valid up to the second order of $|g/(\omega_q - \omega_r)|$ as follows

$$
\begin{aligned}
\hat{H}_{\text{eff}}/\hbar &= \hat{H}_0 + \frac{i}{2}[\hat{S}_1, \hat{V}], \\
&\approx \omega_r \hat{a}^\dagger \hat{a} + \sum_n \omega_n |n\rangle\langle n| + \sum_{n=0} \chi_{n,n+1}|n+1\rangle\langle n+1| - \chi_{0,1}\hat{a}^\dagger\hat{a}|0\rangle\langle 0| \\
&\quad + \sum_{n=1}(\chi_{n-1,n} - \chi_{n,n+1})\hat{a}^\dagger\hat{a}|n\rangle\langle n|.
\end{aligned}
\tag{2.97}
$$

In the last line, two-photon transition terms are ignored, and $\chi_{n,n+1} = g_{n,n+1}^2/\Delta_{n,n+1}$. Then, applying the two-level approximation, we obtain the familiar form of the dispersive Hamiltonian

$$
\hat{H}_{\text{disp}}/\hbar = (\omega_r' + \chi\hat{\sigma}_z)\hat{a}^\dagger\hat{a} - \frac{\omega_q'}{2}\hat{\sigma}_z.
\tag{2.98}
$$

Introducing $\Delta = \omega_q - \omega_r$, each of the above variables can be written as follows

$$
\omega_r' = \omega_r - \frac{g^2}{\Delta + \alpha},
\tag{2.99}
$$

$$
\omega_q' = \omega_q + \frac{g^2}{\Delta},
\tag{2.100}
$$

$$
\chi = -\frac{g^2\alpha}{\Delta(\Delta + \alpha)}.
\tag{2.101}
$$

Here, the first and second lines are the (first-order) Lamb-shifted resonator and transmon frequencies, and the last is the so-called dispersive shift. The first term of Eq. (2.98) shows that the resonance frequency of the resonator changes depending on the state of the qubit. In the dispersive readout scheme, the qubit state can be determined by measuring the phase change of the reflected pulse due to this frequency shift. Moreover, the effective Hamiltonian (2.97) is valid in the $1 \gg |g/\Delta|$ regime. Still, the actual interaction between the resonator and the transmon depends on the number of photons in the resonator through $g_{\text{int}} = \sqrt{n}g$. The critical photon number can be calculated using the equation below

$$
n_{\text{crit}} = \frac{\Delta^2}{4g^2}.
\tag{2.102}
$$

It is the number of photons inside the resonator when the detuning between the resonator and the transmon equals twice the coupling constant $2\sqrt{n}g$. When you start experiments, this formula helps you make a good initial guess of the readout power. Ignoring dissipation, according to input-output theory [12], the average photon number of the single-sided resonator is:

$$
\langle n \rangle = \frac{4}{\kappa_e}\frac{P}{\hbar\omega}.
\tag{2.103}
$$

The resonator is connected to the one-dimensional waveguide via coupling strength κ_e. The resonator is coherently driven by a microwave tone with frequency ω and power P. Using these equations, we obtain the critical readout power as follows

$$
P_{\text{crit}} = \frac{\kappa_e\Delta^2}{16g^2}\hbar\omega_r.
\tag{2.104}
$$

Chapter 3

Superconducting circuit design

This chapter describes design and fabrication methods for superconducting circuits. The fabrication flow of the superconducting circuits you will measure is summarized in the following steps:

1. Find an abstract Hamiltonian of your circuits and determine theoretical values of linear elements and Josephson junctions giving desired behavior.

2. Draw a design CAD of the circuit, realizing the parameters determined in step 1 through iterative numerical simulations using a finite-element electromagnetic simulator such as COMSOL.

3. Let's go to the clean room and fabricate it.

3.1 Circuit design and parameter estimation

This section summarizes useful formulas for designing superconducting circuits and numerical simulation methods for obtaining Hamiltonian parameters from blueprints.

3.1.1 CPW resonator design

Readout resonators are often implemented as CPW resonators, important components of superconducting microwave circuits. These resonators reduce cross-talk by concentrating most of the electromagnetic field between the center conductor and nearby ground. In particular, the $\lambda/4$ CPW resonator is used in many situations thanks to its shorter length, and the resonant frequency is given by the following equation [13]

$$\omega_0 = 2\pi \frac{v_{\text{ph}}}{4l}, \tag{3.1}$$

$$v_{\text{ph}} = \frac{c}{\sqrt{\varepsilon_{\text{eff}}}} = \frac{1}{\sqrt{C_x L_x}}, \tag{3.2}$$

where c and l are the speed of light in vacuum and the length of the resonator, respectively. C_x and L_x are the capacitance and inductance per unit length of CPW. The second line represents the effective phase velocity of CPW in the situation shown in Fig. 3.1, and it

19
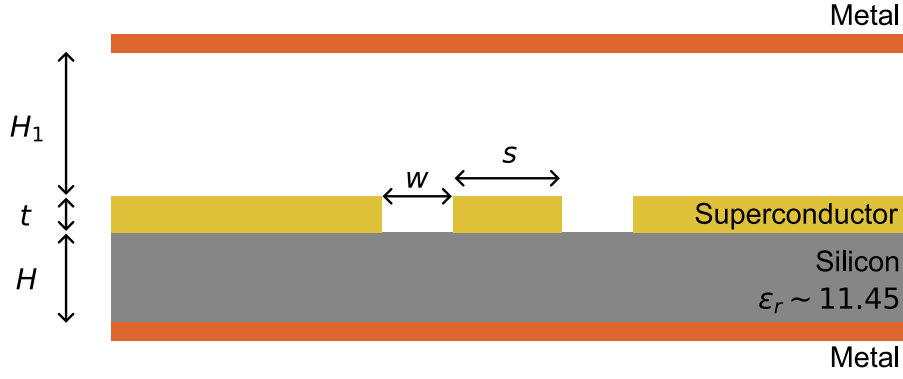
Figure 3.1: Geometry of the typical coplanar-waveguide.

can be obtained using the following formulas [13]

$$\varepsilon_{\mathrm{eff}} = 1 + q(\varepsilon_r - 1), \tag{3.3}$$

$$q = \frac{\frac{K(k)}{K(k')}}{\frac{K(k_1)}{K(k_1')} + \frac{K(k)}{K(k')}}, \tag{3.4}$$

$$k = \frac{\tanh\left(\frac{\pi s}{4H}\right)}{\tanh\left(\frac{\pi(s+2w)}{4H}\right)}, \ k' = \sqrt{1 - k^2}, \tag{3.5}$$

$$k_1 = \frac{\tanh\left(\frac{\pi s}{4H_1}\right)}{\tanh\left(\frac{\pi(s+2w)}{4H_1}\right)}, \ k_1' = \sqrt{1 - k_1^2}, \tag{3.6}$$

where $K(k)$ is the complete elliptic integral of the first kind. Then, the unit capacitance and inductance are given by

$$C_x = 2\varepsilon_0 \varepsilon_{\mathrm{eff}}\left(\frac{K(k_1)}{K(k_1')} + \frac{K(k)}{K(k')}\right), \tag{3.7}$$

$$L_x = \frac{\mu_0/2}{\frac{K(k_1)}{K(k_1')} + \frac{K(k)}{K(k')}}, \tag{3.8}$$

and the characteristic impedance of CPW is $Z_0 = \sqrt{L_x/C_x}$. Using these equations, the initial guess of the resonator length can be determined analytically. Since there are parasitic capacitances due to bending the CPW, fine-tuning is required to achieve the desired frequency.

The CPW resonator is usually modeled as a distributed element circuit, complicating circuit quantization. Therefore, we introduce the relationship between the $\lambda/4$ CPW resonator and a parallel LCR resonator by comparing the input impedances as shown in Fig. 3.2. The input impedance of the CPW resonator near the resonance frequency can be written as

$$Z_{\mathrm{in}}^{\mathrm{CPW}} = Z_0 \frac{1 - i\tan(\alpha l)\cot(\beta l)}{\tan(\alpha l) - \cot(\beta l)}, \tag{3.9}$$

where $\alpha + i\beta = \gamma$ is a complex propagation constant of the CPW. Considering near the resonance frequency $\omega = \omega_0 + \Delta\omega$, this is approximated as follows

$$Z_{\mathrm{in}}^{\mathrm{CPW}} \approx \frac{Z_0}{\alpha l + i\pi\Delta\omega/2\omega_0}, \tag{3.10}$$

(a)

(b)
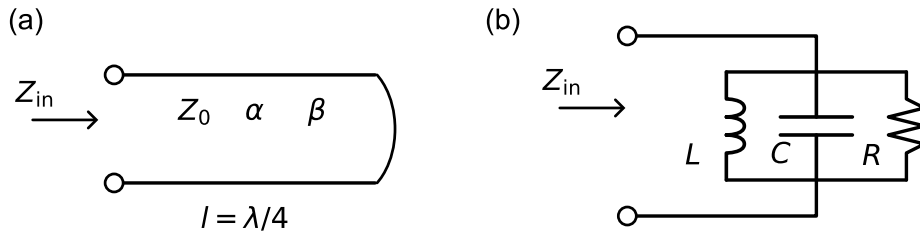
Figure 3.2: (a) Simplified circuit of $\lambda/4$ CPW resonator. (b) Circuit schematics of the parallel LCR resonator.

where $\beta = \omega/v_{\mathrm{ph}}$. On the other hand, the input impedance of the parallel LCR resonator near the resonance frequency is

$$Z_{\mathrm{in}}^{LCR} \approx \frac{1}{1/R + 2i\Delta\omega C}. \tag{3.11}$$

Comparing them, the following equations are obtained

$$R = \frac{Z_0}{\alpha l}, \tag{3.12}$$

$$C = \frac{\pi}{4\omega_0 Z_0}, \tag{3.13}$$

$$L = \frac{1}{\omega_0^2 C}. \tag{3.14}$$

From now on, the circuit will include the CPW resonators based on these equations.

3.1.2   Josephson junction design

To design a transmon, it is necessary to decide the geometrical parameters of the Josephson junction and the parallel shunt capacitor. First, we explain how to design a Josephson junction. The following equation connects E_J in the Hamiltonian and geometric parameters of a Josephson junction:

$$I_c = \frac{\pi\Delta(T)}{2eR_n}\tanh\left(\frac{\Delta(T)}{2k_BT}\right), \tag{3.15}$$

$$E_J = \frac{\hbar}{2e}I_c, \tag{3.16}$$

where I_C is the critical current, $\Delta(T)$ is the superconducting energy gap, e is the electron charge, R_n is the normal resistance of a junction, k_B is the Boltzmann constant, and T is the temperature. This equation is called Ambegaokar-Baratoff's equation [14], an important equation for circuit design. In this thesis, aluminum Josephson junctions are used, and the ambient temperature is sufficiently lower than the superconducting transition temperature of aluminum to allow $\tanh\left(\frac{\Delta(T)}{2k_BT}\right) \sim 1$. The superconducting gap Δ at absolute zero temperature can be calculated by measuring the transition temperature T_c of the deposited aluminum thin film through the following equation [15]

$$\frac{\Delta(0)}{k_BT_c} = 1.764. \tag{3.17}$$

Since the superconducting transition temperature of thin aluminum films is about 1.2 K, we use $\Delta(0) = 180$ μeV in this thesis. Eq. (3.15) shows that the room temperature

Figure 3.3: (a) Top view of a Dolan bridge mask pattern. (b) Cross-sectional view along the black dashed line in (a).

resistance of a Josephson junction can control the Josephson energy. Therefore, the area of a Josephson junction is a main design parameter.

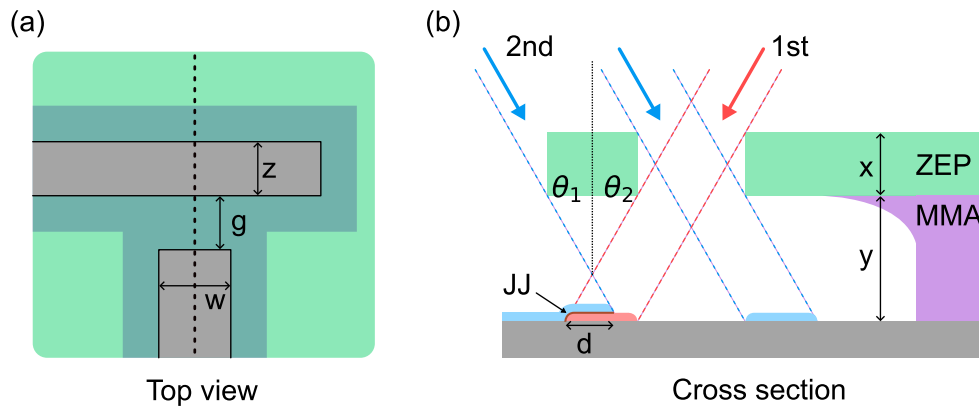Josephson junctions are typically fabricated by the shadow evaporation technique. First, we explain the Dolan bridge method. Thanks to a bridge of width g shown in Fig. 3.3(a), it is possible to fabricate a Josephson junction with an area of $d \times w$, as shown in Fig. 3.3(a) and (b). Assuming $\theta_1 = \theta_2$, the overlapping length of d is calculated by the following equation

$$d = \begin{cases} 2y \tan \theta - g, & \text{if } z - x \tan \theta < d \\ z - x \tan \theta, & \text{otherwise.} \end{cases} \tag{3.18}$$

The Dolan method is more flexible than the Manhattan method, which will be introduced later, and is better suited for making complicated junction shapes.

However, the bridge part of the Dolan method is mechanically weak, and the Manhattan method has recently been used to resolve this problem. This method allows selective deposition thanks to the shadow of resist sidewalls, as shown in Figs. 3.4(a–c). Under this situation, the size of a Josephson junction is $d \times w$, and assuming $\theta_1 = \theta_2$ again, the height of a sidewall, $x + y$, and a width of a mask, $w(d)$, must satisfy the following conditions

$$w, d < (x + y) \tan \theta. \tag{3.19}$$

One problem common to the Dolan and Manhattan methods is that milling causes damage to the substrate surface below Josephson junctions. The damaged substrate surface forms dangling bonds, which could be a host of impurity TLS and a source of decoherence of superconducting qubits. To avoid this problem, a method called in-situ bandage [16] has been developed. This method prevents milling of the substrate surface below Josephson junctions as shown in Figs. 3.4(d,e). When using the in-situ bandage method, the design parameters have a stricter limitation as follows

$$w, d < \frac{x + y}{\sqrt{2} \tan \theta}. \tag{3.20}$$

Depending on requirements, Josephson junctions can be fabricated by the methods described above. Generally speaking, the Dolan method has more design flexibility, making it suitable for fabricating complex junction arrays and multiple junctions with large area ratios. On the other hand, the Manhattan method is less dependent on the deposition angle of the junction size and is mechanically more robust, making it suitable for large-scale integration.
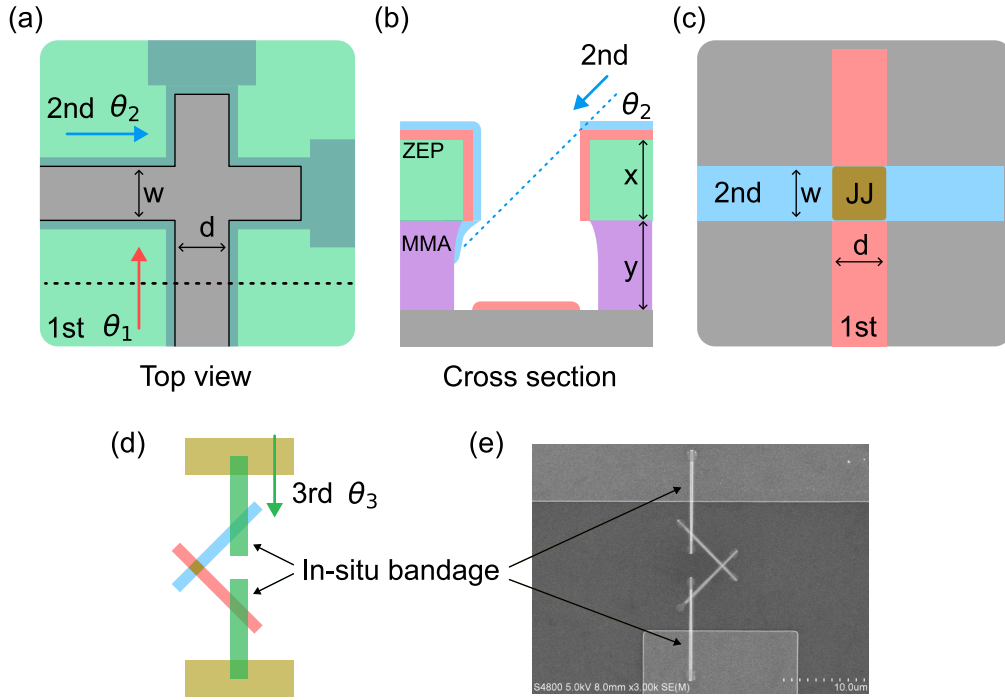
Figure 3.4: (a) Top view of the Manhattan-type resist mask pattern. (b) Cross-sectional view along the black dashed line in (a). (c) Sketch of the resulting Josephson junction after evaporation. (d) Sketch of the Manhattan-type resist mask pattern with the in-situ bandage (green). (e) Scanning electron micrograph of the Josephson junction after resist removal.

The next step is to investigate the mapping between the area of the Josephson junction and the room temperature resistance; an example of the results is shown in Fig. 3.5. The measured resistances are well-fitted by the following function

$$f(x) = \frac{a}{x+b}, \tag{3.21}$$

where a, b, and x are fitting constants and a sweeping parameter of a Josephson junction size, respectively. Moreover, the fitting constant b is considered to be an offset due to the sidewalls of the first layer of the Josephson junction itself, and $\sqrt{b_{\text{fit}}} \sim 100$ nm is consistent with the thickness of the Josephson junction, which is also about 100 nm. The conditions for the normal resistance of the junction depend on the maintenance status of the evaporator and the vacuum level, and it is recommended that the conditions be checked periodically.

3.1.3 Transmon electrodes

Next, we explain how to analytically estimate the electrode design of a transmon based on the literature [17]. Ignoring the ground plane for simplicity in the layout shown in Fig. 3.6, the shunt capacitance is estimated by conformal mapping using the following equations

$$C_s = \frac{\varepsilon_r + 1}{2} \frac{\varepsilon_0 l}{C_K(k)}, \tag{3.22}$$

$$C_K(k) = \frac{K(k)}{K'(k')}, \tag{3.23}$$

$$k = \frac{a}{b}, \ k' = \sqrt{1 - k^2}, \tag{3.24}$$
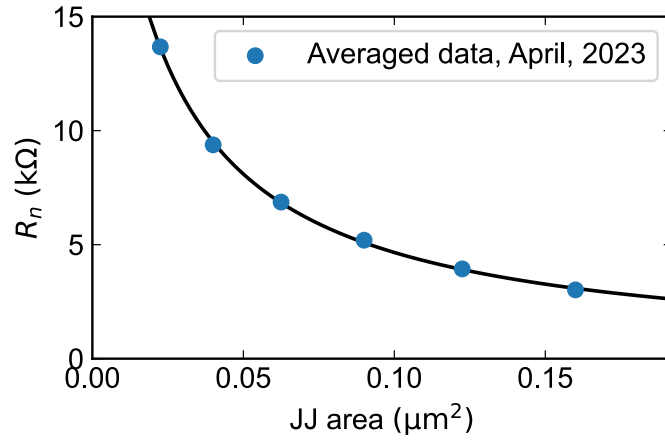
Figure 3.5: Example of room temperature resistance measurements of Josephson junctions. The black solid line is the fitting result with the function $f(x) = \frac{a}{x+b}$.

Figure 3.6: Example of the electrode pattern of a transmon. The electrodes of length l and width $b - a$ are separated by gap $2a$.

where ε_r is the relative permittivity of the substrate.

3.2 Finite-element electromagnetic simulation

At this point, we have determined the initial design parameters of the readout circuit and the Josephson junction parameters for nonlinear elements such as transmon. Based on this information, this section explains how to determine the circuit pattern for fabrication using finite-element electromagnetic simulation.
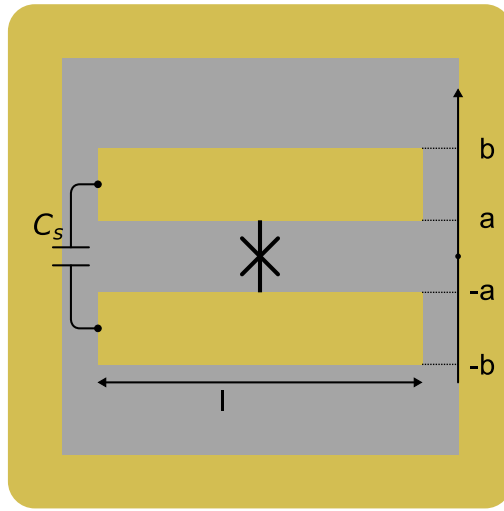
3.2.1 Transmon linearization

To finalize the design of the transmon, iterative tuning of design parameters for electrodes and Josephson junctions is required. However, it is generally challenging to include Josephson junctions in finite-element simulators. Therefore, we consider a transmon as a harmonic oscillator shown in Fig. 3.7(a). At the Hamiltonian level, we consider the following previously introduced Hamiltonian

$$\hat{\mathcal{H}}_{\mathrm{CQ}} \approx 4E_C \hat{N}^2 + \frac{E_J}{2}\hat{\phi}^2 - \frac{E_J}{24}\hat{\phi}^4, \tag{3.25}$$

and ignoring the fourth and higher order terms, we consider the following linearized transmon Hamiltonian

$$\hat{\mathcal{H}}_{\mathrm{LT}} = \frac{\hat{Q}^2}{2C_{\mathrm{eff}}} + \frac{\hat{\Phi}^2}{2L_J}. \tag{3.26}$$

Here, $\hat{N} = \hat{Q}/2e$, $\Phi = \phi_0 \phi$ and $L_J = \phi_0^2/E_J$ are used, and L_J is called the Josephson inductance. The eigenfrequency of this Hamiltonian can be obtained from the eigenvalue analysis of the finite-element simulator as shown in Figs. 3.7(b) and (c). However, the effective capacitance of C_{eff} includes both the effect of the ground plane and deviations from the analytical solution. Therefore, we correct this deviation by sweeping the length l of the electrodes, and the example of length sweep is shown in Fig. 3.8. Once the eigenvalue f_e for the transmon mode is obtained from the finite-element electromagnetic simulation, the capacitance value is calculated from the following equation

$$C_{\mathrm{eff}} = \frac{1}{(2\pi f_e)^2 L_J}, \tag{3.27}$$

and you can finalize the electrode size using these fitting results. Typically, to obtain the anharmonicity about -200 MHz, 60–80 fF is required when f_e is about 5 GHz.

3.2.2 Coupling strength

A superconducting circuit must combine several circuit elements to achieve its full potential. In an actual circuit pattern, this coupling part has a complicated structure, and it is challenging to obtain coupling constants analytically. As discussed above, circuits with Josephson junctions in the transmon regime, i.e., $E_J/E_C \gg 1$, are treated as an LC resonator. Thus, as shown in Figs. 3.9(a)–(c), the resonator-resonator (R-R), transmon-resonator (Q-R), and transmon-transmon (Q-Q) coupled systems can be treated as a coupled LC resonators shown in Fig. 3.9(d). Here, we explain how to obtain coupling constants from the finite-element electromagnetic simulation results.

We consider the coupled qubits with a coupling constant g and energy difference Δ as a starting point. Assuming $g \ll |\Delta|$, their eigenstates are hybridized as follows

$$\widetilde{|0,1\rangle} = |0,1\rangle + \frac{g}{\Delta}|1,0\rangle,$$
$$\widetilde{|1,0\rangle} = |1,0\rangle - \frac{g}{\Delta}|0,1\rangle.$$
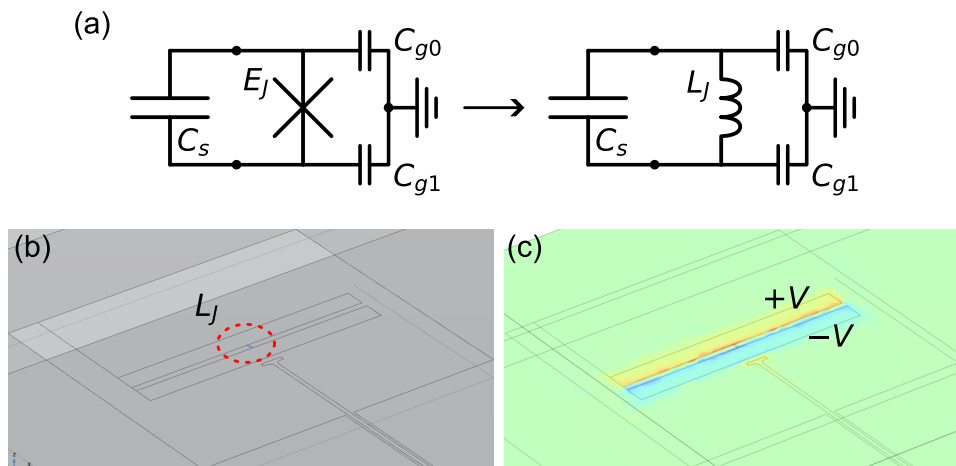
Figure 3.7: (a) Transmon linearization. The Josephson junction is replaced with a linear Josephson inductance. (b) Screenshot of COMSOL GUI, with L_J placed as a lumped element inductor in the area where JJ is located. (c) Example of the eigenvalue analysis result showing the electric field distribution. The floating transmon mode appears to be a differential mode.
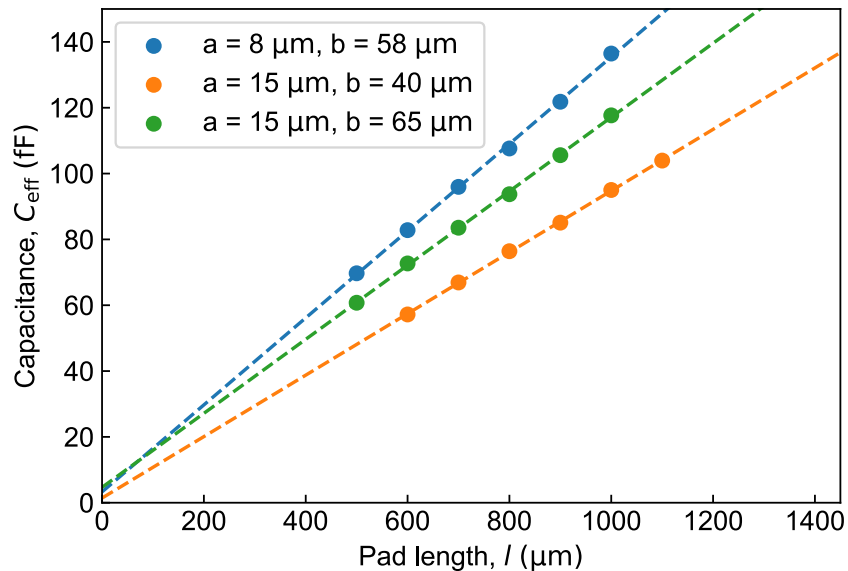
Figure 3.8: Relation between electrode size and capacitance obtained from the finite-element electromagnetic simulation using COMSOL. The dashed line shows the linear fitting results. The distance between the electrodes and the ground plane is fixed.
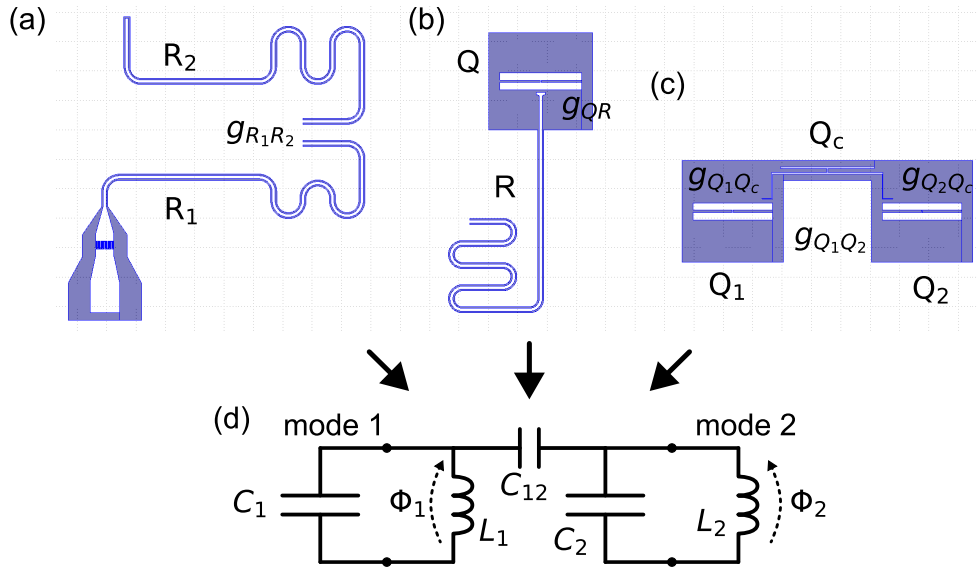
Figure 3.9: (a) CAD pattern of a coupled two CPW resonators system. We can consider them lossless LC resonators using Eqs. (3.13) and (3.14). (b) CAD pattern of a coupled CPW resonator and a transmon system. (c) CAD pattern of a coupled three transmons system. (d) Equivalent circuit schematic of a coupled two LC resonators system. The left (mode 1) and right (mode 2) resonators are capacitively coupled.

Thus, in a coupled system, the other mode is also weakly excited when one mode is excited. This can be generalized to the case of coupled LC resonators, and we consider the following Hamiltonian

$$\hat{H} = \frac{\hat{Q}_1^2}{2C_1} + \frac{\hat{\Phi}_1^2}{2L_1} + \frac{\hat{Q}_2^2}{2C_2} + \frac{\hat{\Phi}_2^2}{2L_2} + \frac{C_{12}}{C_\Sigma}\hat{Q}_1\hat{Q}_2, \tag{3.28}$$

$$\approx \hbar\omega_1\hat{a}^\dagger\hat{a} + \hbar\omega_2\hat{b}^\dagger\hat{b} + \hbar g(\hat{a}^\dagger\hat{b} + \hat{a}\hat{b}^\dagger), \tag{3.29}$$

where the rotating wave approximation is used for the second line, and $C_\Sigma = C_1C_2 + C_1C_{12} + C_2C_{12}$. In addition, the flux and charge operators are written as follows

$$\hat{Q}_1 = \sqrt{\frac{\hbar}{2\omega_1 L_1}}(\hat{a}^\dagger + \hat{a}) = \sqrt{\frac{\hbar}{2Z_1}}(\hat{a}^\dagger + \hat{a}) = Q_{\mathrm{zpf},1}(\hat{a}^\dagger + \hat{a}), \tag{3.30}$$

$$\hat{\Phi}_1 = i\sqrt{\frac{\hbar\omega_1 L_1}{2}}(\hat{a}^\dagger - \hat{a}) = i\sqrt{\frac{\hbar Z_1}{2}}(\hat{a}^\dagger - \hat{a}) = i\Phi_{\mathrm{zpf},1}(\hat{a}^\dagger - \hat{a}), \tag{3.31}$$

$$\hat{Q}_2 = \sqrt{\frac{\hbar}{2\omega_2 L_2}}(\hat{b}^\dagger + \hat{b}) = \sqrt{\frac{\hbar}{2Z_2}}(\hat{b}^\dagger + \hat{b}) = Q_{\mathrm{zpf},2}(\hat{b}^\dagger + \hat{b}), \tag{3.32}$$

$$\hat{\Phi}_2 = i\sqrt{\frac{\hbar\omega_2 L_2}{2}}(\hat{b}^\dagger - \hat{b}) = i\sqrt{\frac{\hbar Z_2}{2}}(\hat{b}^\dagger - \hat{b}) = i\Phi_{\mathrm{zpf},2}(\hat{b}^\dagger - \hat{b}), \tag{3.33}$$

where $\hat{a}$ and $\hat{b}$ are annihilation operators in the bare basis, and the coupling constant is

$$g = \frac{C_{12}}{C_\Sigma}\sqrt{\frac{\omega_1 C_1}{2}}\sqrt{\frac{\omega_2 C_2}{2}} = \frac{C_{12}}{C_\Sigma}\sqrt{\frac{1}{2Z_1}}\sqrt{\frac{1}{2Z_2}}. \tag{3.34}$$

From Eq. (3.29), applying the following transformation, we obtain the diagonalized Hamil-

tonian as follows

$$\hat{H}'/\hbar = \hat{U}\hat{H}\hat{U}^\dagger/\hbar = \omega_1'\hat{a}^\dagger\hat{a} + \omega_2'\hat{b}^\dagger\hat{b}, \tag{3.35}$$

$$\hat{U} = \exp\left[\Lambda\left(\hat{a}^\dagger\hat{b} - \hat{a}\hat{b}^\dagger\right)\right], \tag{3.36}$$

$$\omega_1' = \frac{1}{2}\left(\omega_1 + \omega_2 + \sqrt{\Delta^2 + 4g^2}\right), \tag{3.37}$$

$$\omega_2' = \frac{1}{2}\left(\omega_1 + \omega_2 - \sqrt{\Delta^2 + 4g^2}\right), \tag{3.38}$$

where $\Delta = \omega_1 - \omega_2$ and $\Lambda = \frac{1}{2}\arctan(2g/\Delta)$. Solving equations (3.37) and (3.38) for ω_1 and ω_2 allows us to represent the bare frequencies in terms of the dressed frequencies accessible via numerical simulation:

$$\omega_1 = \frac{A_+ \pm \sqrt{A_-^2 - 4g^2}}{2}, \tag{3.39}$$

$$\omega_2 = \frac{A_+ \mp \sqrt{A_-^2 - 4g^2}}{2}, \tag{3.40}$$

where $A_\pm = \omega_1' \pm \omega_2'$. Furthermore, the eigenstate $|\psi\rangle$ in the bare basis and the annihilation operators are then transformed as follows

$$|\psi'\rangle = \hat{U}|\psi\rangle, \tag{3.41}$$

$$\hat{a}_c \equiv \hat{U}\hat{a}\hat{U}^\dagger = \cos\Lambda\,\hat{a} - \sin\Lambda\,\hat{b}, \tag{3.42}$$

$$\hat{b}_c \equiv \hat{U}\hat{b}\hat{U}^\dagger = \cos\Lambda\,\hat{b} + \sin\Lambda\,\hat{a}, \tag{3.43}$$

where $\hat{a}_c$ and $\hat{b}_c$ are new annihilation operators in the coupled basis. When a classical finite-element simulator obtains eigenvalues, the electromagnetic field distribution of each eigenvalue has a clearly defined phase. Then, this can be considered a large photon number coherent state in a coupled system, with a coherent amplitude of α_c. It can be expressed as follows:

$$
\begin{aligned}
|\alpha_c\rangle &= \hat{D}(\alpha_c)|0,0\rangle, \\
&= \exp\left(\alpha_c\hat{a}_c^\dagger - \alpha_c^*\hat{a}_c\right)|0,0\rangle, \\
&= \exp\left(\cos\Lambda(\alpha_c\hat{a}^\dagger - \alpha_c^*\hat{a})\right) \otimes \exp\left(-\sin\Lambda(\alpha_c\hat{b}^\dagger - \alpha_c^*\hat{b})\right)|0,0\rangle, \\
&= |\alpha_c\cos\Lambda, -\alpha_c\sin\Lambda\rangle.
\end{aligned}
\tag{3.44}
$$

Thus, a coherent state with an amplitude of α_c in a coupled system comprises bare modes excited at certain rates. Then, assuming mode $\hat{a}_c$ is excited with the amplitude α_c, a ratio of expectation values of the currents flowing in each inductor shown in Fig. 3.9(d) is written as follows

$$
\begin{aligned}
r = \frac{\langle\hat{I}_2\rangle_{\alpha_c}}{\langle\hat{I}_1\rangle_{\alpha_c}} &= -\frac{L_1\Phi_{\mathrm{zpf},2}}{L_2\Phi_{\mathrm{zpf},1}}\tan\Lambda, \\
&= -\sqrt{\frac{L_1\omega_2}{L_2\omega_1}}\tan\Lambda,
\end{aligned}
\tag{3.45}
$$

and

$$\tan\Lambda = \frac{-1}{2g}\left(\sqrt{A_- - 4g^2} \mp A_-\right). \tag{3.46}$$

Thus, if the ratio r is obtained from the numerical simulation, the coupling constant g is determined from the solution of Eq. (3.45). For this equation, we consider specific function forms for each case. From here on, we assume that the finite element simulator is COMSOL.

Q-Q coupling

For example, consider the case of three coupled transmons shown in Fig. 3.10. The Josephson inductance is larger (around 1 to 2 orders of magnitude) than the geometric inductance. Due to this, the inductance is considered to exist only at the Josephson junction. Assuming this, we can calculate the currents flowing Josephson inductors when the mode $\hat{a}_c$ is excited. The following is the procedure in COMSOL.

1. Select circuit patterns other than Josephson junctions as the perfect conductor.

2. To calculate g_{12}, select the Josephson junction patterns and set them as lumped element inductors. Then, input the values of Josephson inductance of L_{J1} and L_{J2} derived from E_{J1} and E_{J2}.

3. Execute eigenvalue search, and nothing is assigned for L_{Jc} of no interest.

4. Repeat the above procedure for the other coupling pairs.

We now have the left-hand side values of Eq. (3.45), and dressed mode frequencies. Then, the right-hand side of Eq. (3.45) can be written as follows

$$F_{QQ}(g) = \frac{1}{2g}\sqrt{\frac{L_{J1}}{L_{J2}}}\sqrt{\frac{A_+ \mp \sqrt{A_-^2 - 4g^2}}{A_+ \pm \sqrt{A_-^2 - 4g^2}}}\left(\sqrt{A_- - 4g^2} \mp A_-\right), \qquad (3.47)$$

where $A_\pm$ are known from the simulation. The solutions are shown in Fig. 3.11. To evaluate the validity of this method, the coupling constants are also calculated from the normal mode splitting. This method is simpler and requires only sweeping the L_J value of one of the pairs of interest, and the results are shown in Fig. 3.12. It is necessary to convert the half of normal mode splitting $g_0/2\pi$ determined at $L_{J0}(\neq L_J)$ to the coupling constant at the design value using the following equation:

$$g = \left(\frac{L_{J0}}{L_J}\right)^{1/4} g_0. \qquad (3.48)$$

Here, L_J is the design value, and L_{J0} is the value at the anti-crossing point as shown in Fig. 3.12. Table 3.1 summarizes the results of the two methods, which are consistent. The current ratio method can estimate the coupling constants without time-consuming parameter sweeps.

Table 3.1: Comparison of coupling constants between transmons.

	Normal mode splitting	Current ratio	Experiment [18]
$\lvert g_{12}/2\pi \rvert$ (MHz)	3.2	2.9	1.9
$\lvert g_{1c}/2\pi \rvert$ (MHz)	46	38	40
$\lvert g_{2c}/2\pi \rvert$ (MHz)	46	40	31

Q-R coupling

In general, microwave resonators cannot be considered lumped element resonators. Therefore, the case of Q-R coupling slightly differs from the Q-Q coupling case. The inductance of the microwave resonator is distributed, and it is difficult to obtain the current value by

the finite-element electromagnetic simulation. Thus, we consider the problem in terms of energy ratio. First, we rewrite Eq. (3.45) as follows

$$\frac{\sqrt{L_2}\langle \hat{I}_2 \rangle_{\alpha_c}}{\sqrt{L_1}\langle \hat{I}_1 \rangle_{\alpha_c}} = -\sqrt{\frac{\omega_2}{\omega_1}} \tan \Lambda, \tag{3.49}$$

where we assume the mode 1 and mode 2 are a distributed constant resonator and a transmon, respectively. When the mode 1 is excited, the following equation holds for the energy stored in the electromagnetic fields

(Energy of the electric field) = (Energy of the magnetic field)

$$+ \text{(Energy in the Josephson inductance)}, \tag{3.50}$$

$$\mathcal{E}_{\text{ele}} = \mathcal{E}_{\text{mag}} + \mathcal{E}_{\text{JJ}}. \tag{3.51}$$

Thus, the left-hand side of Eq. (3.49) can be rewritten as follows

$$\frac{\sqrt{L_2}\langle \hat{I}_2 \rangle_{\alpha_c}}{\sqrt{L_1}\langle \hat{I}_1 \rangle_{\alpha_c}} = \sqrt{\frac{4\mathcal{E}_{\text{JJ}}^1}{4\mathcal{E}_{\text{mag}}^1}}. \tag{3.52}$$

In COMSOL, the spatial integrals for electric and magnetic fields are implemented, and $\mathcal{E}_{\text{ele}}$ and $\mathcal{E}_{\text{mag}}$ can be obtained numerically. Furthermore, since the current flowing through the lumped element is not included in the spatial integrals, $\mathcal{E}_{\text{JJ}}$ can also be obtained as follows

$$\mathcal{E}_{\text{JJ}}^{\text{COMSOL}} = \mathcal{E}_{\text{ele}}^{\text{COMSOL}} - \mathcal{E}_{\text{mag}}^{\text{COMSOL}}. \tag{3.53}$$

We can obtain the Q-R coupling constant by solving Eq. (3.49) with this ratio for g.

R-R coupling

In the case of R-R coupling, there are no lumped elements, and it is generally difficult to determine the coupling constant by the current ratio method. Therefore, we consider a specific case where a coupling pair consists of two $\lambda/4$ CPW resonators to obtain the current ratio. In this case, the energy of the magnetic field can be calculated if the maximum current value at the anti-node is known. This value can be obtained by setting a lumped element inductor with a negligibly small inductance value at the current anti-node. Therefore, the left-hand side of Eq. (3.45) can be obtained, but the right-hand side requires some modifications as follows

$$-\frac{L_1 \Phi_{\text{zpf},2}}{L_2 \Phi_{\text{zpf},1}} \tan \Lambda = -\frac{L_1}{L_2}\sqrt{\frac{Z_2}{Z_1}} \tan \Lambda,$$

$$= -\frac{Z_{0,1}}{\omega_1}\frac{\omega_2}{Z_{0,2}}\sqrt{\frac{Z_2}{Z_1}} \tan \Lambda. \tag{3.54}$$

For the second line, Eq. (3.14) is used, and $Z_{0,1}$ and $Z_{0,2}$ are the characteristic impedance of the $\lambda/4$ CPW resonators. From Eqs. (3.14) and (3.13), the following relationship exists between the characteristic impedance and the effective LC resonator model impedance

$$Z_i = \frac{4}{\pi} Z_{0,i}, \text{ for } i \in \{1, 2\}. \tag{3.55}$$

From Eq. (3.54), assuming that the characteristic impedances of the CPW resonators are equal, we obtain the following equation

$$\frac{\langle \hat{I}_2 \rangle_{\alpha_c}}{\langle \hat{I}_1 \rangle_{\alpha_c}} = -\frac{\omega_2}{\omega_1} \tan \Lambda. \tag{3.56}$$

We can obtain the R-R coupling constant for the coupled $\lambda/4$ CPW resonators by solving Eq. (3.56) with a numerically obtained ratio for g.
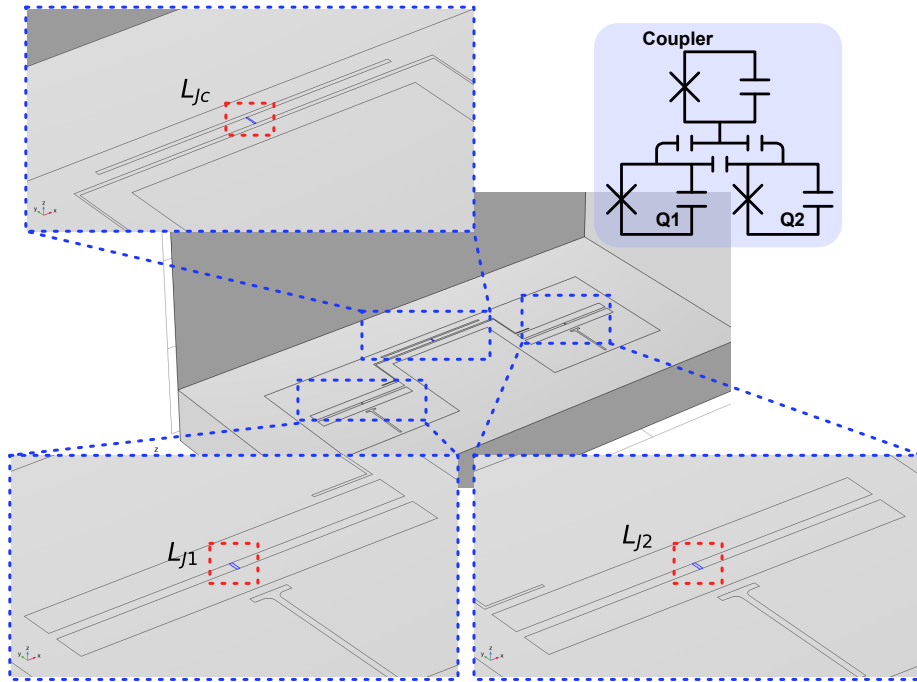
Figure 3.10: Screenshots of the COMSOL and an equivalent circuit schematic of the coupled three transmon system. Each transmon contains a Josephson inductance that is located inside the red box. During the simulation, two inductances of interest are enabled, and the other is disabled. The Josephson inductance values are $L_{Ji} = (10.3, 10.0, 9.5)$ nH for $i = (1, 2, c)$.
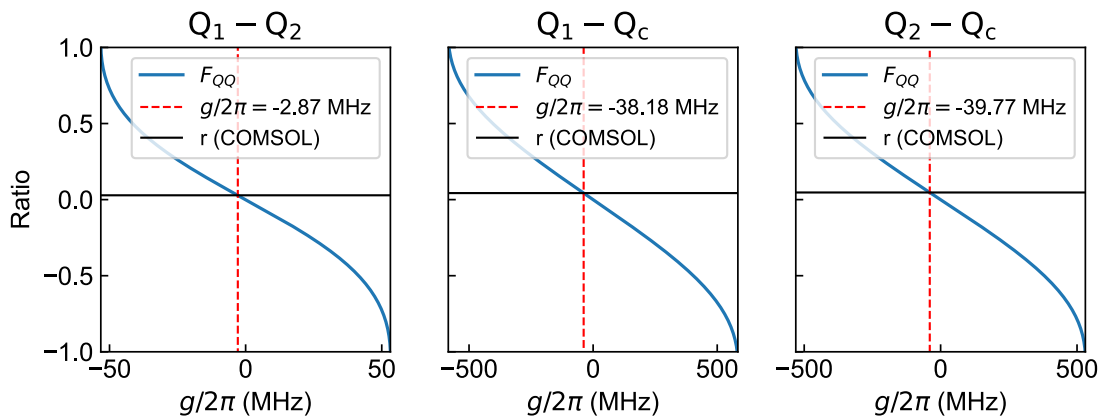
Figure 3.11: Solution of Eq. (3.45) for each coupling pair. The blue solid lines are plots of Eq. (3.47) with the obtained eigenfrequencies $\omega_1' = 2\pi f_1'$ and $\omega_2' = 2\pi f_2'$. The black solid lines are the current ratio computed by COMSOL. The intersections of the red dashed lines indicate the solutions.
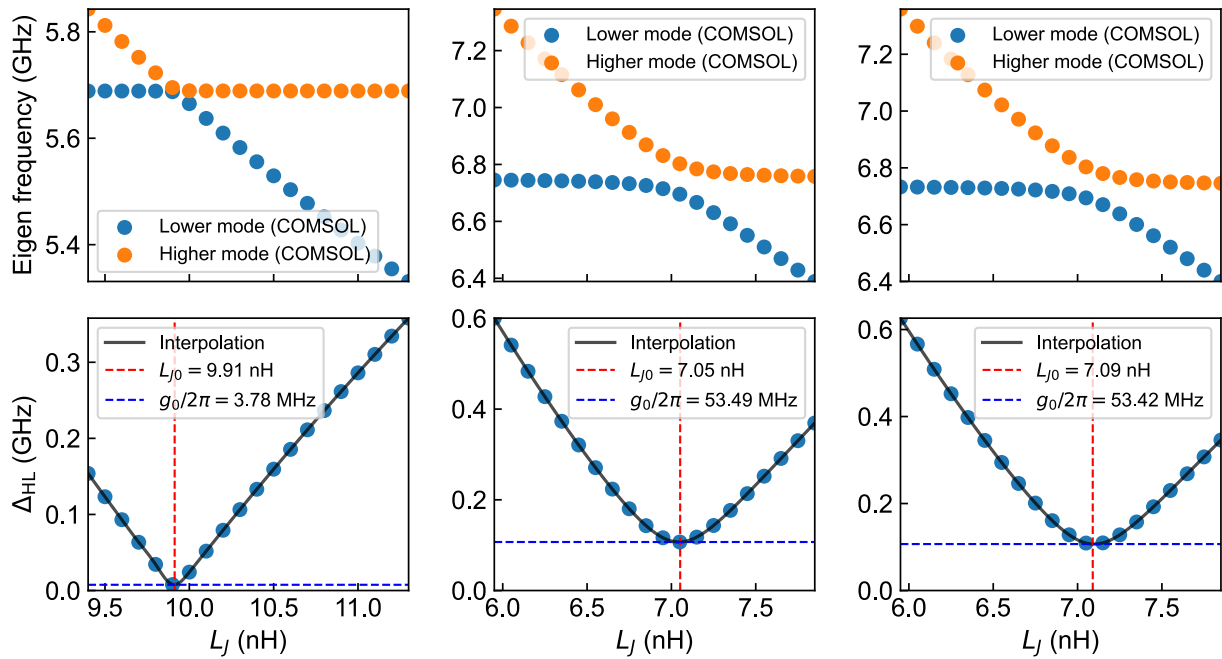
Figure 3.12: Computed normal mode splittings. The larger design value of L_{Ji} is swept for each plot. The intersections of the red and blue dashed lines indicate the coupling constants under resonance conditions. $\Delta_{\mathrm{HL}} = $ (Higher mode) $-$ (Lower mode).

3.3   Sample fabrication

This section describes sample fabrication processes. As outlined in Figs. 3.13(a)–(g), the main fabrication process consists of the following four steps:

1. Photolithography for CPW and other circuit patterns.

2. Dry etching.

3. Electron beam (EB) lithography for Josephson junction masks.

4. Josephson junction formation.

It is crucial to clean the wafer entirely after each step to ensure high-quality superconducting circuits. After the dry etching process and the photoresist is removed, a significant amount of organic residues, such as deformed photoresist caused by the heat during dry etching, are left on the wafer. It is important to remove these organic residues by ashing and HF acid cleaning.
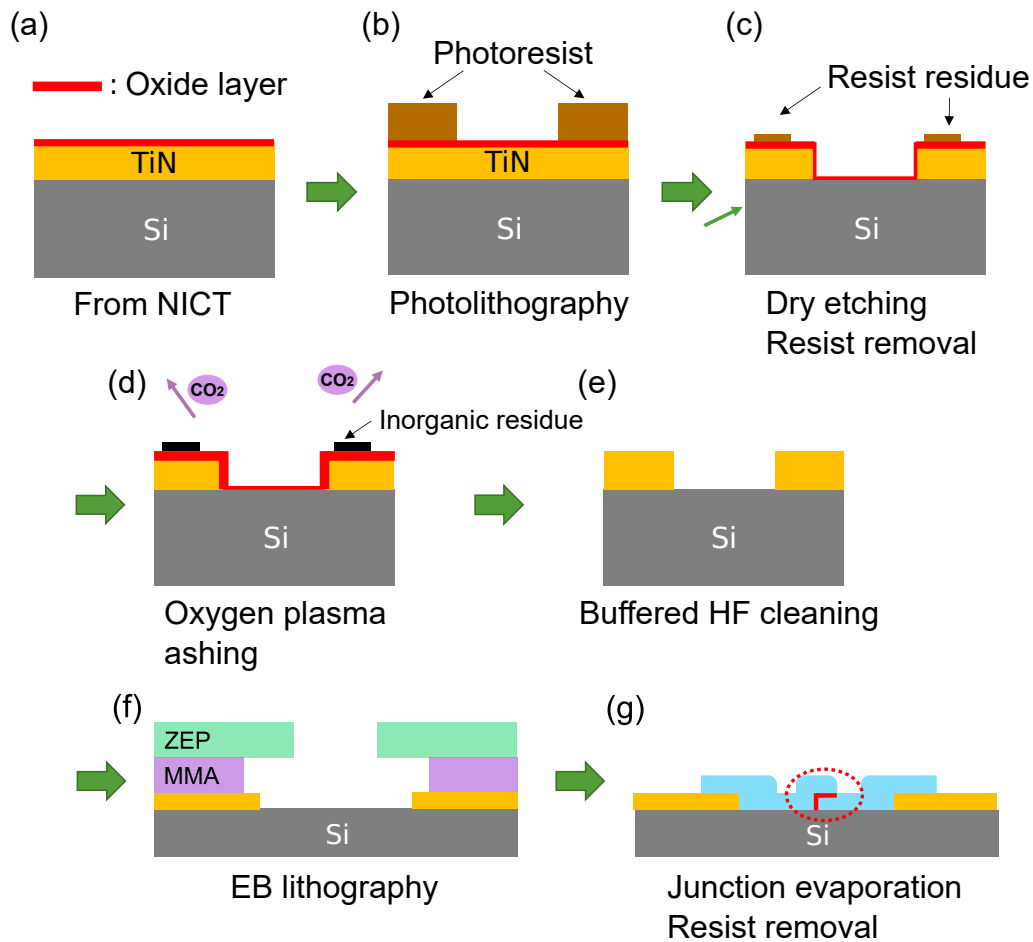
Figure 3.13: Schematic of a sample preparation process. (a) A thin natural oxide layer is present on TiN when the substrate arrives from NICT. (b) Preparing a photoresist mask for circuit patterns by photolithography. (c) The dry etching forms the circuit patterns, and the photolithography mask is removed. (d) Ashing burns off organic matter, including resist residues, to uniformly oxidize the wafer surface. (e) Washing away the oxide film and residues by HF acid cleaning. (f) Forming an EB-resist mask for Josephson junctions by EB lithography. (g) Josephson junctions fabricated by shadow evaporation technique.

Chapter 4

Experimental setup

In the following sections, we describe the experimental setup and the devices we use.

4.1 Measurement setup and samples

The transmons and the resonators are fabricated on a high-resistivity Si substrate. They are made from a sputtered and lithographically-patterned TiN film, and $Al/AlO_x/Al$ Josephson junctions evaporated and lifted off with the in-situ bridge-free bandage technique.

First, the standard design CAD for the transmon performance evaluation is shown in Fig. 4.1. In this sample, four transmon qubits are coupled to the transmission line via a readout resonator. The readout resonator frequencies are in 7–8 GHz. In addition, the readout resonators' dispersive shifts and external coupling constants are typically less than 1 MHz, and the qubit energy relaxation through the readout line is negligible. As shown in Fig. 4.2(a), the input line of the dilution refrigerator has about 54-dB attenuation at 8 GHz including the cable loss. Also, it has an eccosorb filter, an 8-GHz lowpass filter, and an extra 10-dB attenuator. The sample is mounted inside a three-layer magnetic shield and cooled to ∼10 mK. Microwave pulses are generated by the single sideband modulation (SSB) [Figs. 4.2(b) and (c)]. The reflection pulses of the readout resonators are amplified with a low-noise HEMT amplifier at the 4-K stage and demodulated to IQ signals for the data processing [Fig. 4.2(d)]. Note that this setup is also used to evaluate lumped element resonators shown in Fig. 4.3(a)–(d). Due to mesh issues, numerical calculation with COMSOL is difficult for lumped element resonators. We swept the capacitor pad size and length of the meander inductor to find a desirable resonator design.

Next, the design CAD for the coupler-assisted SWAP interaction experiment is shown in Fig. 4.4. In this sample, the two data transmons are capacitively coupled to the fixed-frequency transmon coupler, and each transmon has a readout resonator. The data transmon also has a Purcell filter. As shown in Fig. 4.5(a), each input line of the dilution refrigerator has about 56-dB attenuation at 8 GHz including the cable loss. Each input line also has an eccosorb filter, an 8-GHz lowpass filter, and an extra 6-dB (20-dB) attenuator for the qubit (resonator) drive line. The sample is mounted inside a three-layer magnetic shield and cooled to ∼15 mK. Microwave pulses are generated by the single sideband modulation (SSB) [Figs. 4.5(b) and (c)]. The reflection pulses of the readout resonators are amplified with a low-noise HEMT amplifier at the 4-K stage and demodulated to IQ signals for the data processing [Fig. 4.5(d)]. The readout resonator frequencies are $\omega_r^1/2\pi \simeq 7.436$ GHz, $\omega_r^2/2\pi \simeq 7.375$ GHz and $\omega_r^c/2\pi \simeq 7.551$ GHz, respectively. The dispersive shifts of the readout resonators are typically around 1 MHz, and the qubit energy relaxation through the readout line is negligible.

Figure 4.1: Example of CAD image for the transmon performance evaluation.
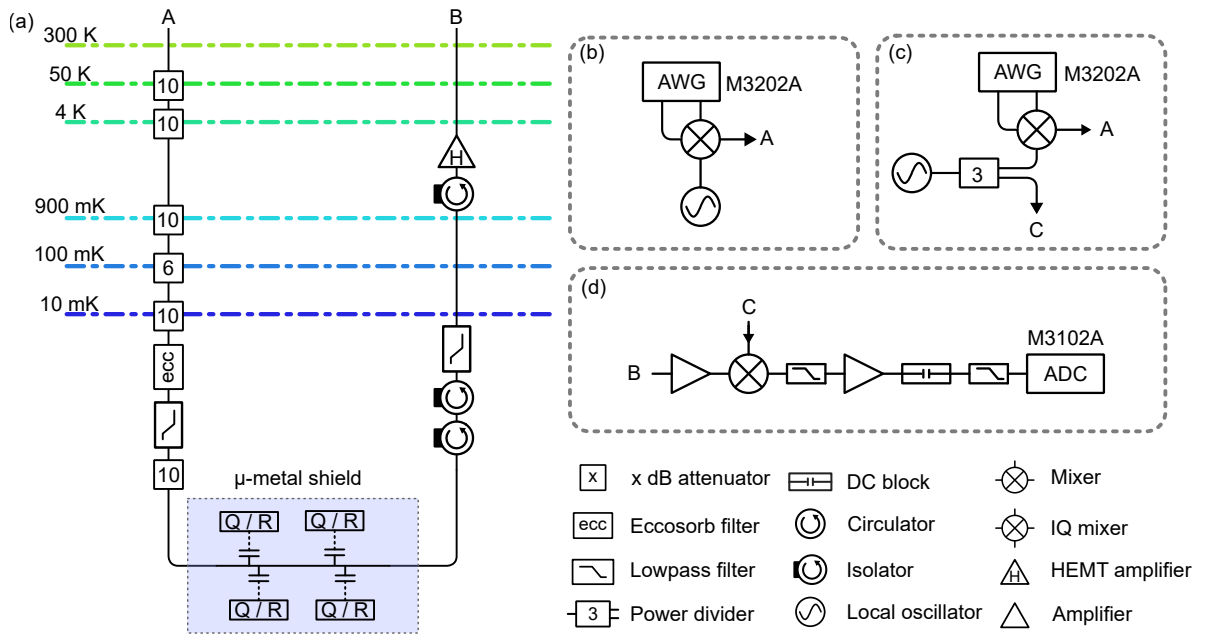
Figure 4.2: Wiring setup for the transmon and lumped element resonator performance evaluation experiment. (a) Connections from the sample chip to ports A-B at room temperature. The qubit control drive and readout drive share the input line. (b) Pulse-generating systems for qubit control. (c) Pulse-generation systems for qubit readout. (d) Readout system.
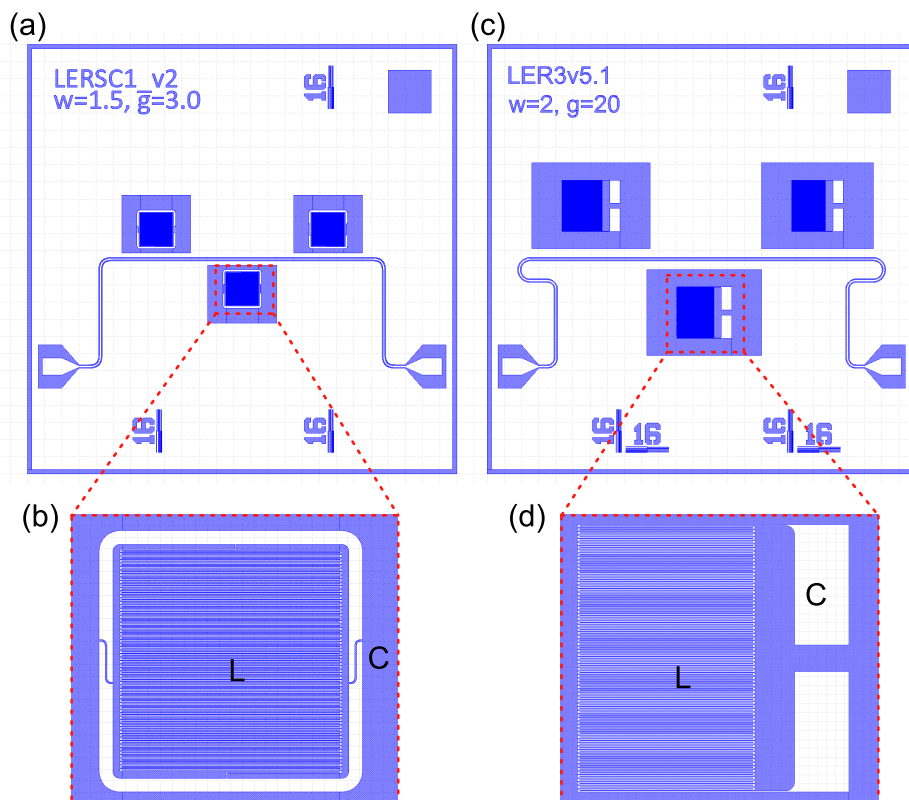
Figure 4.3: Example of CAD image for the lumped element resonator design optimization. (a) The initial resonator pattern long meander inductance is surrounded by outer capacitance pads. (b) Enlarged view of the lumped element resonator pattern. (c) Second-generation lumped element resonator pattern. The meander inductor and capacitor are separated for a more transmon-like design. (d) Enlarged view of the lumped element resonator pattern.
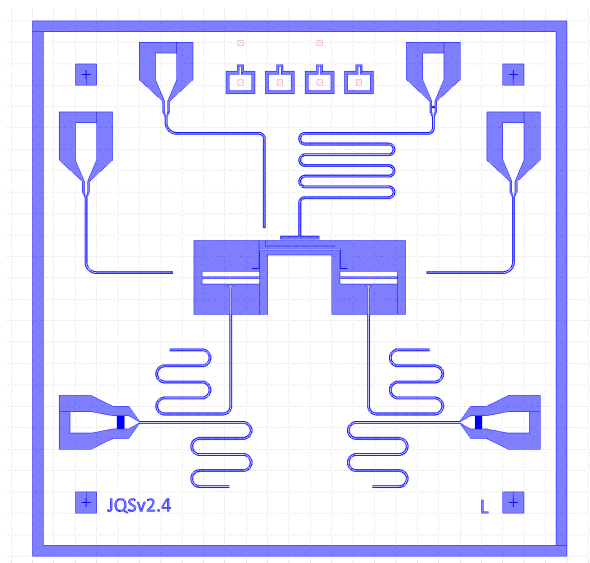
Figure 4.4: Example of CAD image for the coupler-assisted SWAP interaction experiment.
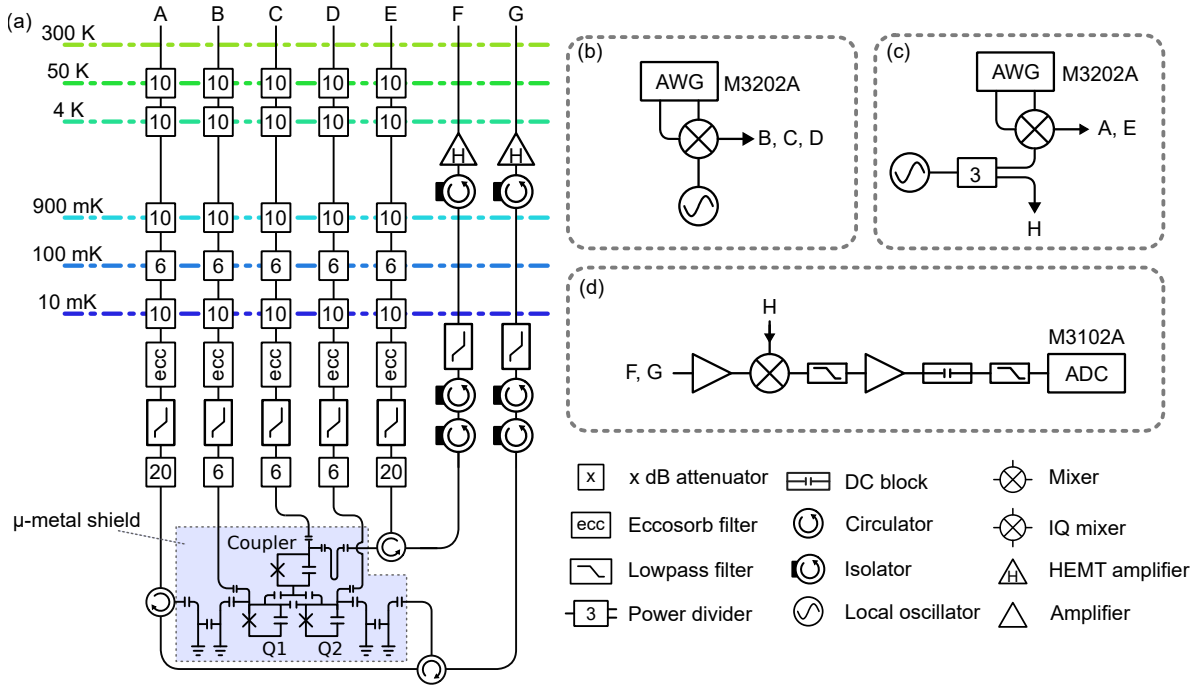
Figure 4.5: Wiring setup for the coupler-assisted SWAP interaction experiment. (a) Connections from the sample chip to ports A-G at room temperature. (b) Pulse-generating systems for qubit control. (c) Pulse-generation systems for qubit readout. (d) Readout system.

The final design CAD shown in Fig. 4.6 is for the artificial spin-dependent force experiment. In this sample, the cubic transmon is capacitively coupled to the host lumped element resonator to store bosonic states, and the cubic transmon has a readout resonator and Purcell filter. The sample is mounted inside a three-layer magnetic shield and cooled to $\sim$15 mK. As shown in Fig. 4.6(a), the input lines A and C have about 56-dB attenuation at 8 GHz including the cable loss. For the input line B, the 10 mK stage attenuator is replaced with a 0-dBm attenuator because a strong drive strength is needed to activate the artificial spin-dependent force interaction. In this experiment, we use a lumped element Josephson parametric amplifier (LJPA) for the single-shot readout, which is also mounted inside a three-layer magnetic shield. Since LJPA requires a strong pump microwave drive to work, we use a low attenuation (13-dB, including the cable loss) input line D. As shown in Figs. 4.7(b), microwave pulses are generated by fully digital arbitrary waveform generators (AWGs) sharing a 2.4 GHz clock signal. The reflection pulses of the readout resonators are amplified with a low-noise HEMT amplifier at the 4-K stage and demodulated by a digital downconverter (DCN) also sharing the 2.4 GHz clock signal. The demodulated signal is digitized by an analog-to-digital converter (ADC). The 2.4 GHz clock signal gives pulse generation and acquisition components high phase coherence. To bias the cubic transmon and LJPA, the DC current sources are used [Figs. 4.7(c)]. The readout resonator frequency and external coupling are $\omega_r/2\pi \simeq 7.575$ GHz and $\kappa_r^{\text{ext}}/2\pi \simeq 2$ MHz, respectively. The dispersive shifts of the readout resonators are around 1.5 MHz, and the qubit energy relaxation through the readout line is negligible tanks to the Purcell filter.
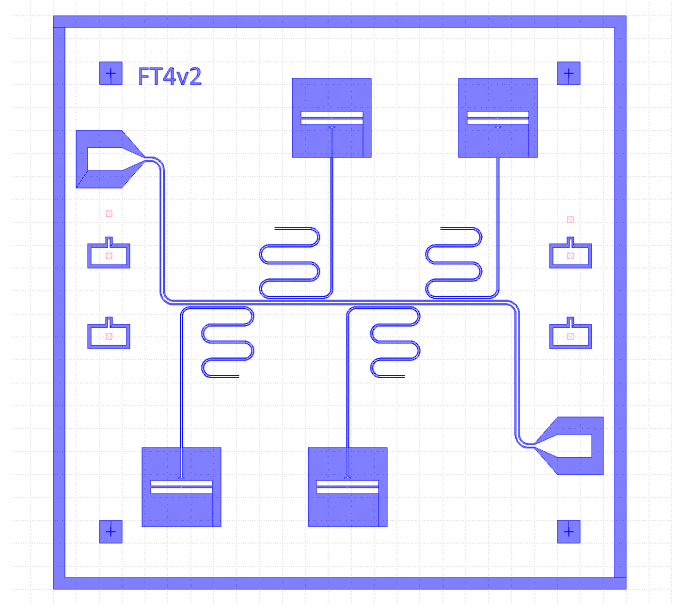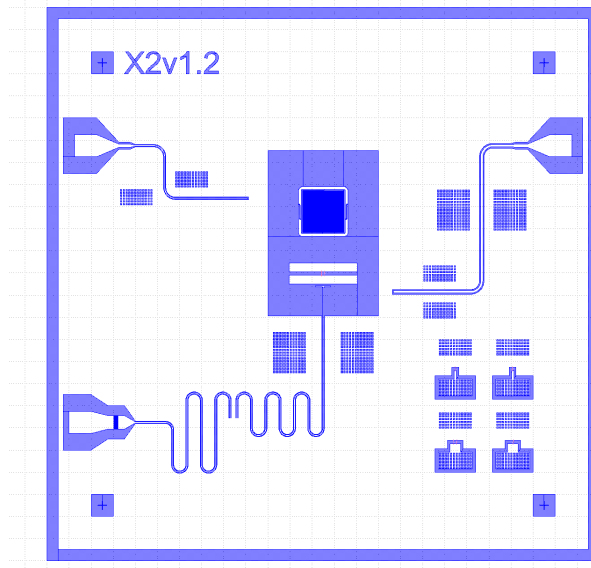
Figure 4.6: Example of CAD image for the artificial spin-dependent force experiment.
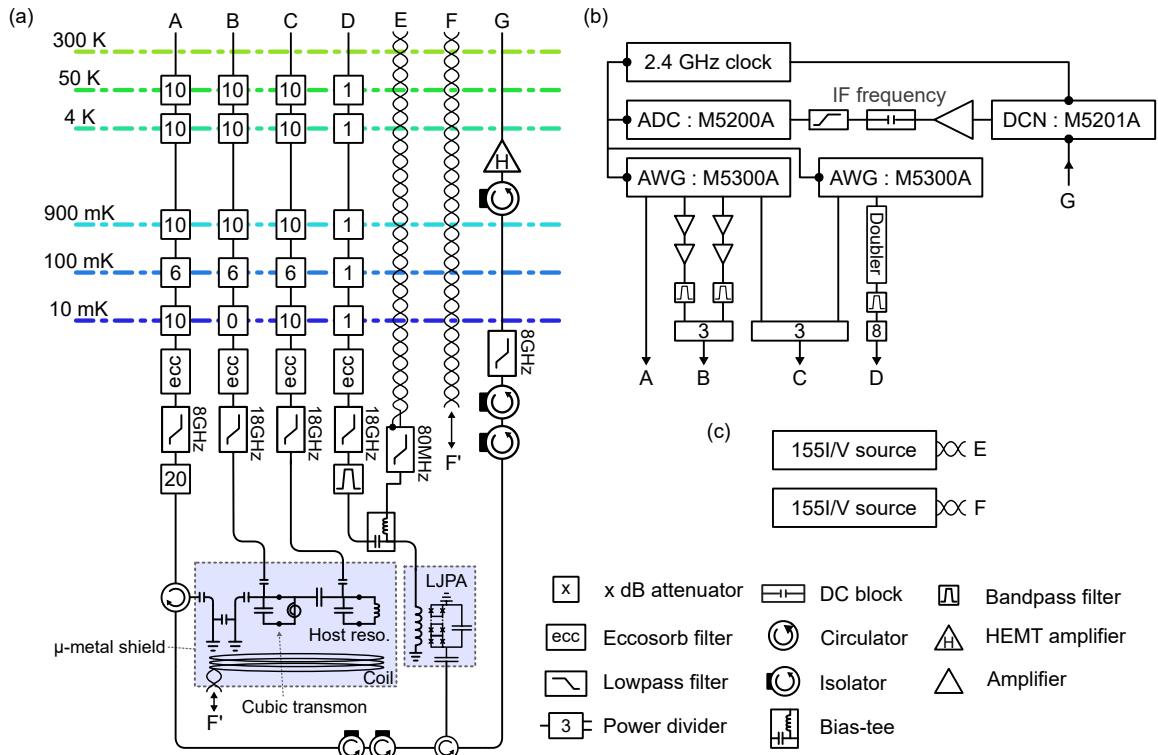
Figure 4.7: Wiring setup for the artificial spin-dependent force experiment. (a) Connections from the sample chip to ports A-G at room temperature. (b) Pulse generation and acquisition systems for control and readout. (c) DC current sources to set the magnetic bias of the cubic transmon and LJPA.
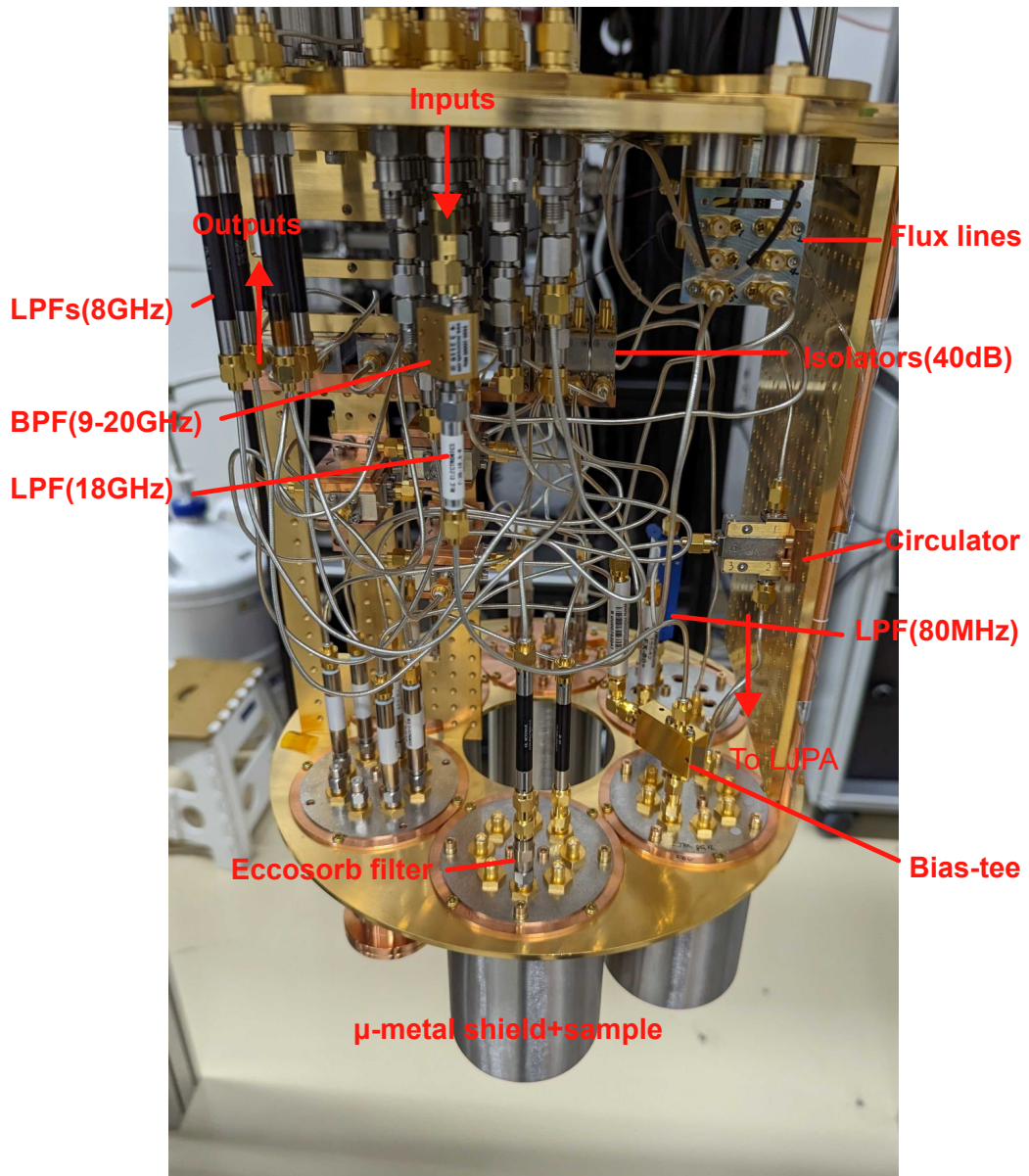
Figure 4.8: Photograph of an example of the cryogenic wiring.

4.2 Signal processing

This section describes how to generate microwave pulses and process acquired waveforms.

4.2.1 Microwave pulse generation

As shown in Fig. 4.9, the IQ-mixer has an asymmetric structure with two mixers inside. For the LO port, the incoming signal is first divided into the port I and the port Q branches, ideally with equal power. The port Q signal is then phase-shifted by a phase shifter by $\pi/2$. These signals are then multiplied by $I(t)$, $Q(t)$ with an intermediate frequency (IF) at each branch of the IQ-mixer and combined again on the RF port. Then, a signal $S_{\mathrm{RF}}(t)$ is output, and this is represented as follows

$$S_{\mathrm{RF}}(t) = I(t)\cos(\omega_{\mathrm{LO}}t) + Q(t)\cos\left(\omega_{\mathrm{LO}}t + \frac{\pi}{2} + \Delta_\phi\right). \tag{4.1}$$

Here, Δ_ϕ represents that the actual phase shift is not completely $\pi/2$ and corresponds to the relative phase deviation between two branches. The typical value of this phase deviation is $5° \sim 10°$ for Marki products. Next, we explain a calibration procedure for the single side band (SSB) modulation to generate clean microwave pulsed using the IQ-mixer. First, consider waveforms of amplitude A_I, A_Q and frequency ω_{IF} as input signals to the I and Q ports, respectively

$$I(t) = A_I \cos(\omega_{\mathrm{IF}}t + \phi_I), \tag{4.2}$$
$$Q(t) = mA_Q \sin(\omega_{\mathrm{IF}}t + \phi_Q). \tag{4.3}$$

Here, m is a scale parameter, and ideally $m = 1$. In this case, $S_{\mathrm{RF}}(t)$ can be written as follows

$$S_{\mathrm{RF}}(t) = A_I \cos(\omega_{\mathrm{IF}}t + \phi_I)\cos(\omega_{\mathrm{LO}}t) \tag{4.4}$$
$$+ mA_Q \sin(\omega_{\mathrm{IF}}t + \phi_Q)\cos\left(\omega_{\mathrm{LO}}t + \frac{\pi}{2} + \Delta_\phi\right). \tag{4.5}$$

In the calibration process, the input amplitudes, A_I and A_Q, are first adjusted to be $A_I = mA_Q = A$. In most cases in our laboratory, A is about 1.0 V. Then, from product to sum formulas, we obtain

$$2S_{\mathrm{RF}}(t) = A\cos(\omega_+ t + \phi_I) + \cos(\omega_- t - \phi_I) \tag{4.6}$$
$$+ A\cos(\omega_+ t + \phi_Q + \Delta_\phi) - \cos(\omega_- t - \phi_Q + \Delta_\phi), \tag{4.7}$$

where $\omega_\pm = \omega_{\mathrm{LO}} \pm \omega_{\mathrm{IF}}$. If you want to use ω_+ (Up-conversion) as an output frequency, set $\phi_I = \phi_Q - \Delta_\phi$ to obtain the following equation from sum to product formulas,

$$S_{\mathrm{RF}}(t) = A\cos\left(-\frac{\Delta_\phi}{2}\right)\cos\left(\omega_+ t + \phi_I + \frac{\Delta_\phi}{2}\right). \tag{4.8}$$

The calculations up to this point are valid even if A is time-dependent, so pulse shaping can be performed.

4.2.2 Waveform processing and digital filter

Next, we describe a handling method for time-series signals from the sample, such as the response from the resonators. The return signal is analog, and acquiring it as a digital
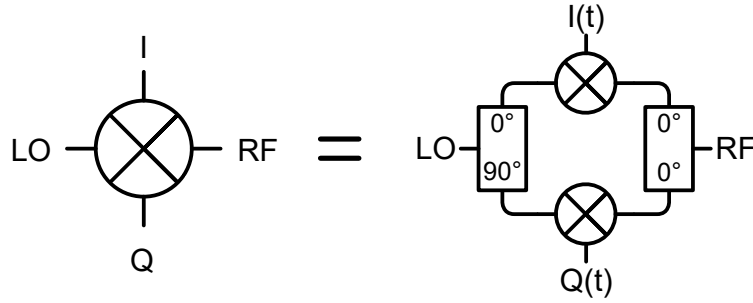
Figure 4.9: Circuit symbol and internal schematics of the IQ mixer.

signal is necessary to process the signal and know the quantum state of the sample. For this purpose, the analog-to-digital converter (ADC), also known as the data acquisition module (DAQ), is used. In this study, we mainly use M3102A manufactured by Keysight. Since the sampling frequency of this product is 500 MSa/sec, it is difficult to read correctly unless the main frequency component of the signal is approximately 250 MHz or less, half the sampling frequency. This frequency is also called Nyquist frequency. Therefore, it is necessary to convert the signal frequency down to the ω_{IF} frequency by the mixer before inputting the signal to the ADC. This is expressed by the following equation

$$
\begin{aligned}
R(t) &= A_{\mathrm{IF}}(t)\cos(\omega_+ t + \phi_{\mathrm{IF}}(t))\cos(\omega_{\mathrm{LO}}t), \\
&= A_{\mathrm{IF}}(t)\{\cos(\omega_{\mathrm{IF}}t + \phi_{\mathrm{IF}}(t)) + \cos((\omega_+ + \omega_{\mathrm{LO}})t + \phi_{\mathrm{IF}}(t))\}.
\end{aligned} \tag{4.9}
$$

Here, $R(t)$ is an output of the mixer passed through a low-pass filter to cut a sum frequency, and only a differential frequency ω_{IF} components are input to the ADC. The input signal $IF(t)$ is written as follows

$$
IF(t) = A_{\mathrm{IF}}(t)\cos(\omega_{\mathrm{IF}}t + \phi_{\mathrm{IF}}(t)). \tag{4.10}
$$

The amplitude and phase of this signal $IF(t)$ contain information from the sample. We next consider processing this signal to obtain amplitude and phase information.

Multiplying the $IF(t)$ signal at time t by $\cos(\omega_{\mathrm{IF}}t)$, $\sin(\omega_{\mathrm{IF}}t)$ and integrating the result $I_a(t)$, $Q_a(t)$, respectively, gives the following equation

$$
I_a(t) = \frac{2}{T_{\mathrm{IF}}} \int_t^{t+T_{\mathrm{IF}}} d\tau\, IF(\tau)\cos(\omega_{\mathrm{IF}}\tau) = A_{\mathrm{IF}}(t)\cos(\phi_{\mathrm{IF}}(t)), \tag{4.11}
$$

$$
Q_a(t) = \frac{2}{T_{\mathrm{IF}}} \int_t^{t+T_{\mathrm{IF}}} d\tau\, IF(\tau)\sin(\omega_{\mathrm{IF}}\tau) = A_{\mathrm{IF}}(t)\sin(\phi_{\mathrm{IF}}(t)), \tag{4.12}
$$

where the subscript a means it is an analog signal. The above operation eliminates the oscillation component, extracting the amplitude and phase components. Here, $T_{\mathrm{IF}} = 2\pi/\omega_{\mathrm{IF}}$. The actual $IF(t)$ obtained by the ADC is a discrete digital value, and performing the above operation is called digital filtering. The integral is computed by replacing the numerical integral with the trapezoidal integral. Therefore, if we denote the sampled digital $IF(t)$ by $IF[t]$, the above equation can be written as follows using the trapezoidal integral formula

$$
I_d[t_n] = \frac{2}{T_{\mathrm{IF}}} \sum_{i=1} \Delta_t \frac{IF[\tau_{i+1}]\cos(\omega_{\mathrm{IF}}\tau_{i+1}) + IF[\tau_i]\cos(\omega_{\mathrm{IF}}\tau_i)}{2} = A_{\mathrm{IF}}[t_n]\cos(\phi_{\mathrm{IF}}[t_n]),
$$
$$\tag{4.13}$$

$$
Q_d[t_n] = \frac{2}{T_{\mathrm{IF}}} \sum_{i=1} \Delta_t \frac{IF[\tau_{i+1}]\sin(\omega_{\mathrm{IF}}\tau_{i+1}) + IF[\tau_i]\sin(\omega_{\mathrm{IF}}\tau_i)}{2} = A_{\mathrm{IF}}[t_n]\sin(\phi_{\mathrm{IF}}[t_n]). \tag{4.14}
$$

Here, Δ_t is the interval between discretized points determined from the sampling frequency, which in most cases in our laboratory is 2ns. The sum is for one period, and $\{t_n\}$ is the time each point was sampled. Thus, the amplitude and phase of the signal $IF[t_n]$ at time t_n are calculated as follows

$$A_{\text{IF}}[t_n] = \sqrt{I_d^2[t_n] + Q_d^2[t_n]}, \tag{4.15}$$

$$\phi_{\text{IF}}[t_n] = \arctan\left(\frac{Q_d[t_n]}{I_d[t_n]}\right). \tag{4.16}$$

In the dispersive readout for discriminating the ground and excited states of a superconducting qubit, the integral intervals of Eqs. (4.11) and (4.12) are replaced by the sampling time T_{samp} as follows

$$\bar{I}_a = \frac{2}{T_{\text{IF}}} \int_t^{t+T_{\text{samp}}} d\tau \, IF(\tau) \cos(\omega_{\text{IF}}\tau), \tag{4.17}$$

$$\bar{Q}_a = \frac{2}{T_{\text{IF}}} \int_t^{t+T_{\text{samp}}} d\tau \, IF(\tau) \sin(\omega_{\text{IF}}\tau), \tag{4.18}$$

where T_{samp} is an integer multiple of the period T_{IF}. Replacing this with numerical integration in the same way, the signal $(\bar{I}_d, \bar{Q}_d)$ is obtained.

Chapter 5

High-quality transmon qubits

Two-dimensional transmon qubits and resonators are indispensable for realizing various quantum technologies, such as quantum computers and sensing using superconducting circuits. In particular, extending the coherence time of these devices is an essential issue in the realization of quantum computers, not only to enable more precise quantum control but also to reduce the requirements on peripheral control devices. Niobium (Nb) thin film is widely used for superconducting circuits. However, dielectric loss due to Nb-oxide generated during fabrication is problematic, as noted in [19–21]. Hydrofluoric (HF) acid cleaning can remove this loss source, but Nb-oxide film re-grows in the air in a few tens of minutes [20]. Aluminum (Al) thin film is also widely used, and its oxide layer is thin and low loss. Still, its chemical stability is poor, making it incompatible with cleaning processes using acid or alkali solutions. To address these issues, we chose a domain-matched epitaxially grown Titanium Nitride (TiN) thin film provided by the Terai group at NICT [22]. TiN is known for a slow oxide film re-growth rate of several months [23] and compatibility with HF acid cleaning thanks to its good chemical stability. Using this, we developed the process for fabricating qubits and resonators described in Chapter 3. Surprisingly, energy relaxation and coherence times exceeding 400 μs were observed for the fixed-frequency transmon qubits fabricated using the process without particular design optimization as shown in Fig. 5.1. These results are state-of-the-art performance as demonstrated in Fig. 5.2.

Based on these results, this chapter reports the results of our efforts to improve the performance of transmon qubits further.

5.1 Background

The main causes of decreasing the energy relaxation and dephasing times of superconducting qubits and resonators are as follows

- Purcell loss due to capacitive and inductive coupling to external circuits.

- Dielectric loss due to organic residues, oxide layers, and amorphous layers on the substrate.

- Resistance loss due to the skin effect of normal metal, which is the material of a sample holder.

- Radiation to parasitic modes.

- Radiation to continuous modes (when packaging is imperfect).

45

Figure 5.1: Measured data of the longest energy relaxation time (T_1) and dephasing time (T_2^e) from our sample. Note that each data was measured using the Tsai-Lab's dilution refrigerator in their sample holder at different cooldowns. The frequency of the transmon is about 4.914 GHz. The author prepared the sample using the same process as in the following experimental results. The orange solid lines fit the results with the exponential decaying function.

Figure 5.2: History of coherence time improvement in superconducting qubits. The charge qubits values are from works [4, 24]. The phase qubit value is from a work [25], and the flux qubit values are from works [26–28], the transmon qubit values are from works [29–36], the c-shunt flux qubit value is from a work [37], and the fluxonium qubit values are from works [38–40].

- Interaction with impurity two-level systems (TLS).

- Quasiparticle excitation due to high-energy particles, infrared radiation, etc.

The Purcell loss can be solved by using a Purcell filter and by making the coupling of the external circuit to the readout resonator sufficiently small during the performance evaluation phase [7, 41, 42]. Radiation into free space can be solved by designing the sample holder with as few gaps as possible [43]. To reduce impurity two-level systems, using the purer material as much as possible and employing a bandage process to avoid damage to the substrate surface [8, 16, 44]. As previously explained, we employ the in-situ bandage method in our fabrication process. To avoid quasiparticle excitation, ensuring sufficient thermal contact between the substrate and sample holder is effective [45, 46], and inserting an infrared absorption filter called an eccosorb filter in the wiring is also effective [47]. As a first step in this study, we focused on dielectric losses resulting from organic residues, oxide layers, and amorphous layers on the substrate [17, 36, 48, 49].

The electric field distribution of the transmon is shown in Fig. 5.3(a). Dielectric losses are on the circuit surface and inside of the substrate. The interfaces on the circuit surface are then divided into three types, as shown in Fig. 5.3(b). The Substrate-Air (SA) interface mainly comprises an oxide material of the substrate. The Metal-Substrate (MS) interface consists of amorphous and substrate oxides. The Metal-Air interface consists of metal oxide. For $i \in \{\mathrm{MS}, \mathrm{MA}, \mathrm{SA}\}$, the internal loss of the transmon can be written as follows

$$\frac{1}{Q} = \frac{1}{2\pi f_{\mathrm{ge}} T_1} = \sum_i p_i \tan \delta_i + \Gamma_0. \tag{5.1}$$

The participation ratio, p_i, represents the ratio of electric field energy at the interface to the transmon's electric field energy. Each layer has a microwave loss tangent, $\tan \delta_i$, and losses near the junction are included in the constant Γ_0 that also accounts for losses in the substrate. f_{ge} and T_1 are the transmon's first excited state frequency and energy relaxation time. As shown in Fig. 5.3(a), The electric field distribution of the transmon has a slow gradient compared to the thickness (1 to 5 nm) of the oxide layers on the surface [17, 36, 48, 49]. Therefore, the electric field can be assumed to have the same direction and magnitude at the top and bottom of the lossy region. Under this situation, the participation ratio of each lossy interface can be expressed as follows [49]

$$p_{\mathrm{SA}} = \frac{\varepsilon_{\mathrm{SA}}^c}{1 + \varepsilon_{\mathrm{sub}}} \frac{\delta}{2a(1-k)K'(k)K(k)} \left[\ln\left(4\frac{1-k}{1+k}\right) - \frac{k\ln(k)}{1+k} + 1 - \ln\left(\frac{\delta}{a}\right) \right], \tag{5.2}$$

$$p_{\mathrm{MS}} = \frac{\varepsilon_{\mathrm{sub}}^2}{\varepsilon_{\mathrm{MS}}^c \varepsilon_{\mathrm{SA}}^c} p_{\mathrm{SA}}, \tag{5.3}$$

$$p_{\mathrm{MA}} = \frac{1}{\varepsilon_{\mathrm{MA}}^c \varepsilon_{\mathrm{SA}}^c} p_{\mathrm{SA}}. \tag{5.4}$$

Here, $k = a/b$ is a geometric parameter of the transmon design from Fig. 5.3(c). $\varepsilon_{\mathrm{sub}} = 11.45$ is the relative dielectric constant of the silicon substrate and $\delta = 3$ nm is the thickness of lossy layers. ε_i^c is a ratio of relative dielectric constants between two surfaces and is set to 5 according to the literature [49], but this value is not important here. Therefore, if the dielectric loss is dominant, the energy relaxation time is expected to increase if the design values of a and b are adjusted within acceptable range to make the participation ratio small. Fig. 5.4 shows the results of sweeping the participation ratios for each geometric parameter.
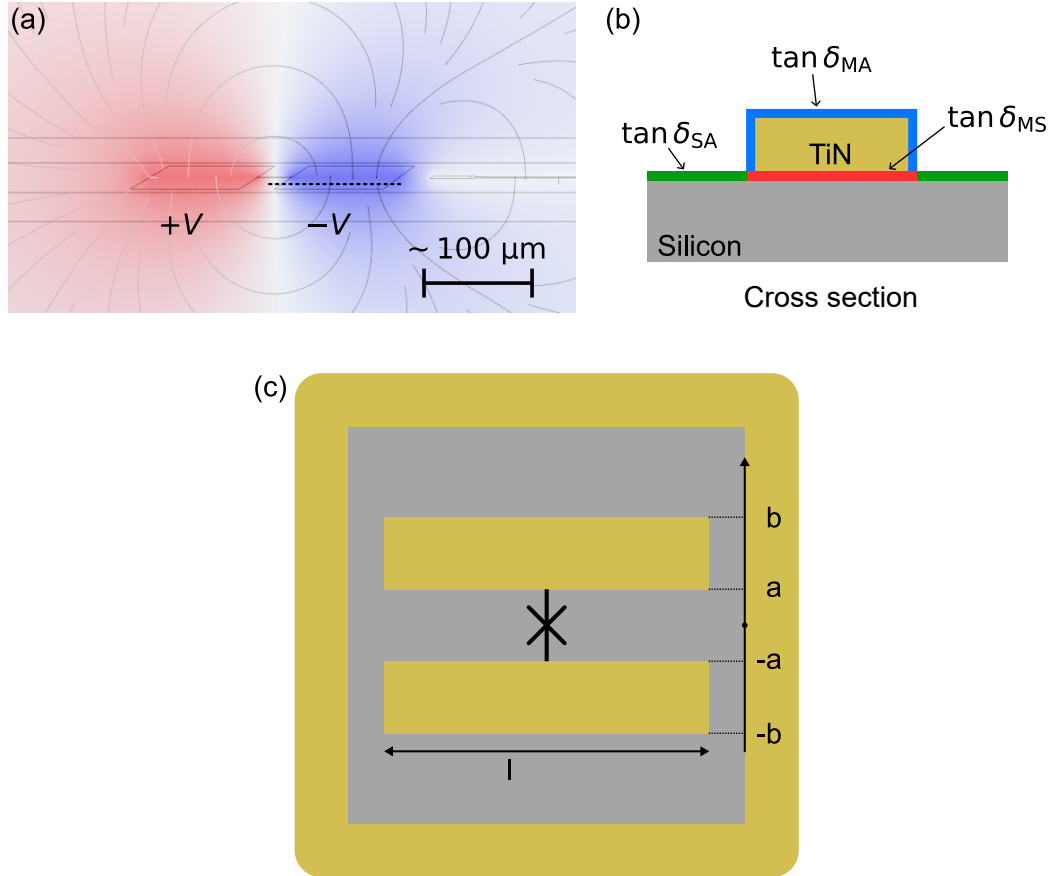
Figure 5.3: (a) Example of electric field distribution when a transmon mode is excited. (b) Cross section of the electrode corresponding to the black dot line in (a). Dielectric losses exist at the Substrate-Air (SA, green), Metal-Air (MA, blue), and Metal-Substrate (MS, red) interfaces and inside the silicon substrate. (c) Definition of the design parameters of the transmon.
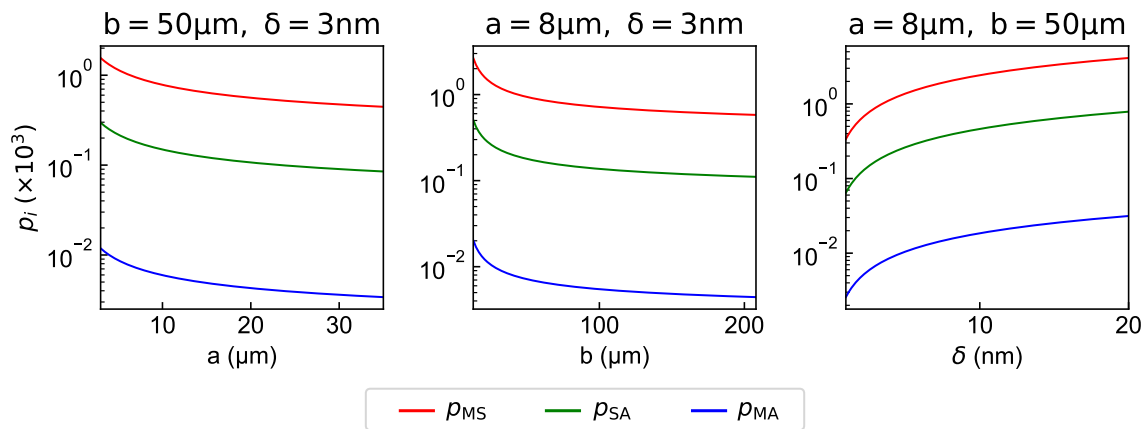
Figure 5.4: Dependence of the participation ratios on geometric parameters. We have set ε_i^c to 5 for three regions: SA, MS, and MA.
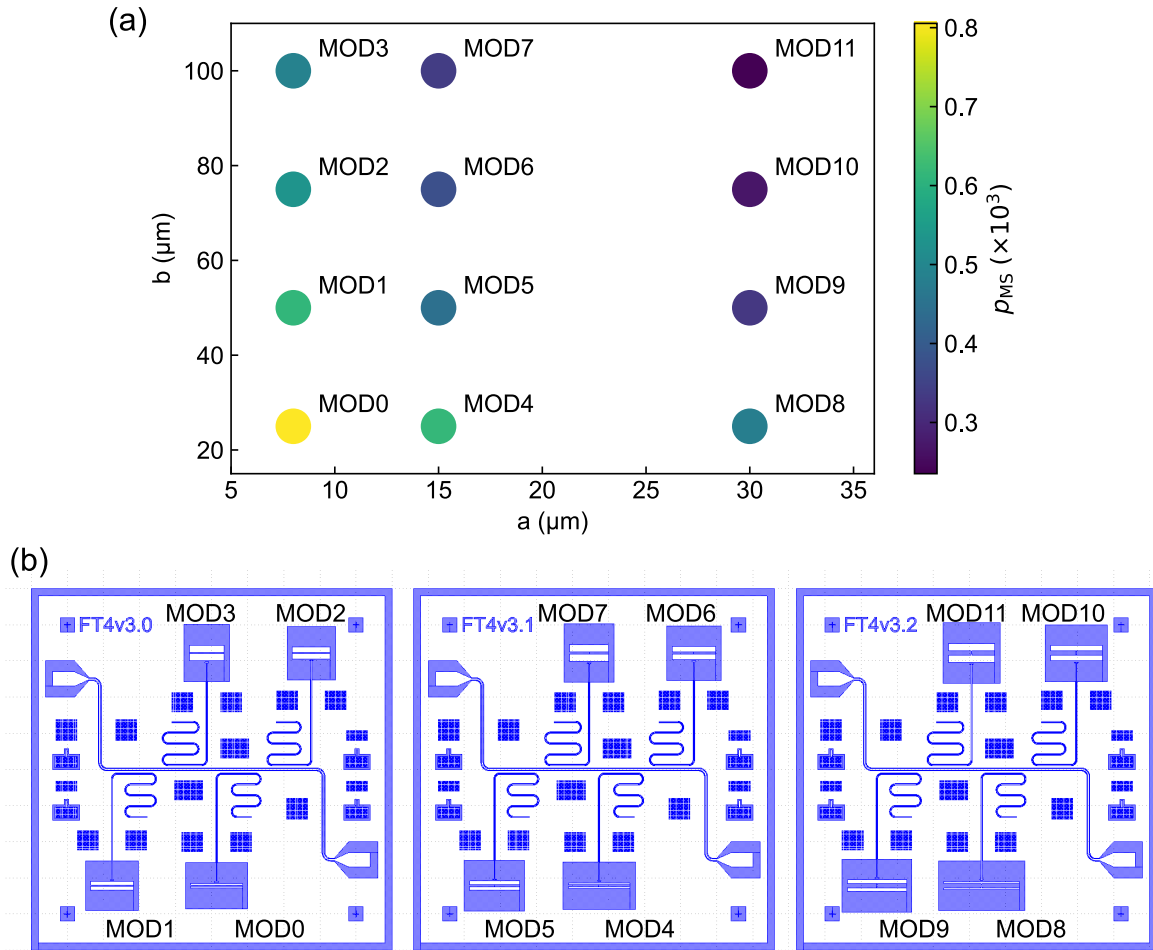
Figure 5.5: (a) Design value and magnitude of PR(p_{MS}) for each transmon. (b) CAD patterns for the fabrication. Twelve different transmons were fabricated on three separate chips.

5.2 Experiment

To confirm that the participation ratio (PR) can be used as a guideline for design optimization, we designed and fabricated 12 different types of transmons with varying PR as shown in Fig. 5.5. Fig. 5.6 shows the experimental results. This experiment has no linear dependence on PR as expected from Eq. (5.1).

5.3 Discussion

The best samples achieved state-of-the-art values, while it is currently difficult to discuss their dependence on the PR for further performance improvement. The result could be due to the possibility that any of the energy mitigation factors discussed above are still dominant and the impact of PR has been masked. After taking measurements, we conducted a detailed analysis of the sample holder, and we noticed that the quality factor of the transmon heavily relies on the counterbore's radius beneath the chip as shown in Fig. 5.9(a). In the numerical simulation using COMSOL, we consider the resistance loss of entire walls due to the skin effect, excluding the air- and superconductor-boundary conditions as shown in Fig. 5.7. In this situation, we swept the radius of the counterbore hole as shown in Fig. 5.8 and obtained the result shown in Fig. 5.9.
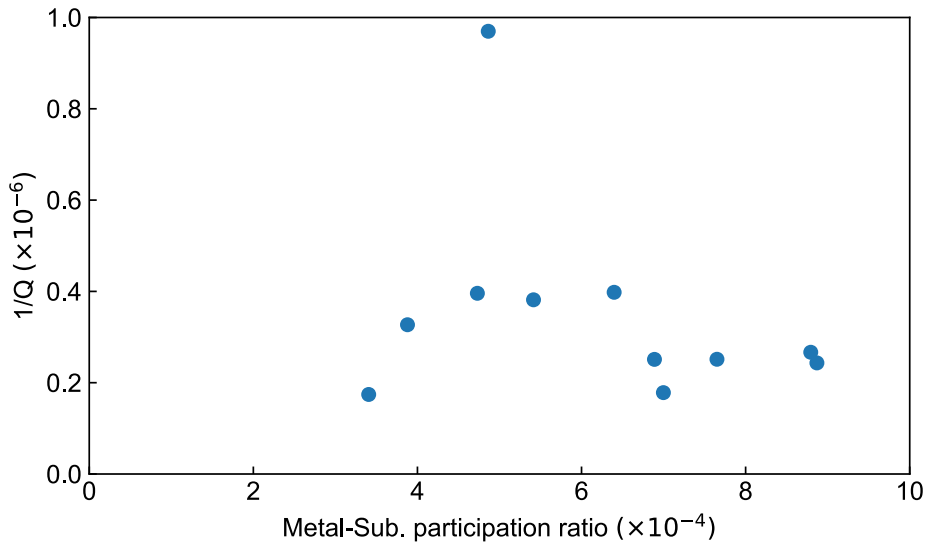
Figure 5.6: (a) Design value and magnitude of $\mathrm{PR}(p_{\mathrm{MS}})$ for each transmon. (b) CAD patterns for the fabrication. Twelve different transmons were fabricated on three separate chips.

These effects were not considered when designing the samples, and the chip space of the PCB has a margin of 100 μm to load a chip smoothly. In addition, the alignment between the transmon and the counterbored hole can easily vary by 200 μm due to the about 100 μm of mounting and machining accuracy of the PCB and jigs. Initially, the counterbore hole is designed to increase the frequencies of the silicon substrate modes and to keep the lossy boundary below the chip away from the bottom of the substrate. However, it was found that the transmon performance can quickly change depending on the position of the hole's edge when the chip size is 5 mm. We plan to avoid this issue by increasing the size of the chip and situating the transmon near the center. Then, we will sweep the design value and measure the energy relaxation time again in the future.
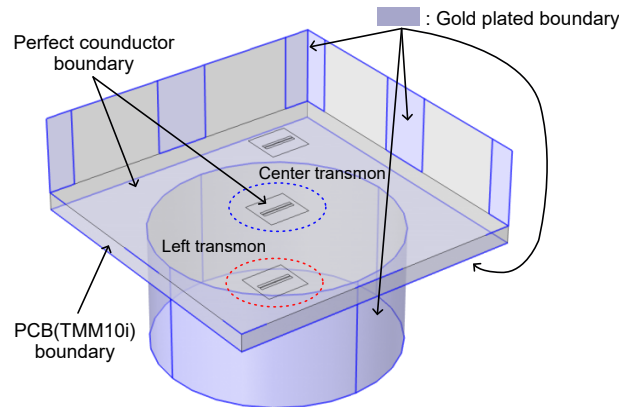
Figure 5.7: Situation of COMSOL simulation. The blue shaded areas are gold plated and considered impedance boundary conditions with a gold conductivity at 1 K, $\sigma = 4.5 \times 10^9$ S/m [50]. Since the side walls of the Si substrate are in contact with the PCB, the loss tangent of 0.002 is specified for TMM10i, the dielectric layer of the PCB. The superconducting thin films of the transmon electrodes and ground planes are assumed to be perfect conductors. Other boundary conditions are vacuum (no loss). The boundary condition of the lid (not shown) is also gold.
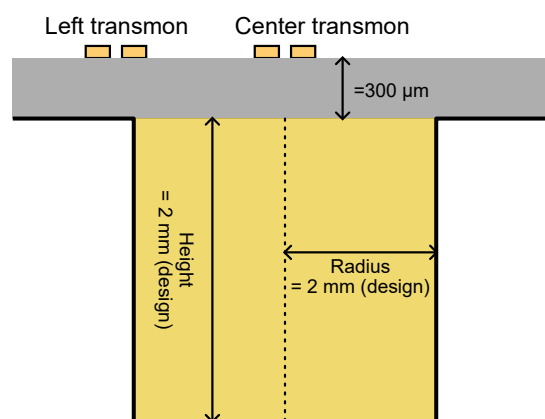
Figure 5.8: Location of the transom on the chip and the counterbored hole (false scaled). The center of the chip and the counterbore hole are fixed, and the radius of the counterbore hole is swept.
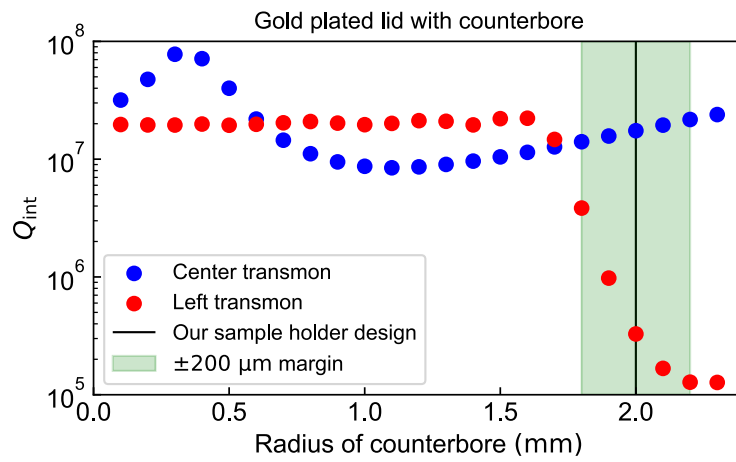
Figure 5.9: Simulated quality factors of transmons using the 3D-eigenvalue solver of COMSOL. The minimum mesh size is 1 μm, about five times smaller than the smallest structure (Josephson junction area). Blue and red dots are quality factors of the transmons located at the center and lower left, as shown in Fig. 5.7, respectively. The black line is the design value of the counterbored hole. The green shaded area indicates the region where the displacement of 200 μm deviates from the design.

Chapter 6

Coupler-assisted SWAP interaction

Superconducting circuits are one of the leading platforms toward realization of fault-tolerant quantum computing [51, 52]. Among various types of qubits, fixed-frequency transmon [7] is a promising building block thanks to its long coherence time and small wiring overhead. For the architecture using fixed-frequency transmons, various all-microwave two-qubit gates have been proposed [10, 53–59], and the cross-resonance (CR) gate is the most commonly-used entangling gate [53, 60–62]. In those schemes, however, weak anharmonicity of transmons results in a residual static ZZ interaction, which causes coherent errors and reduces the fidelity of operations. Therefore, it is of importance to suppress the residual interaction while maintaining the gate operation speed. A widely-adopted method for the purpose is to set the detuning between neighboring transmons to be in the so-called straddling regime, i.e., within the limited anharmonicity [7], though there remain some unwanted higher-order transitions to be avoided. The so-called frequency-crowding problem hinders the straightforward design of the circuits [63, 64]. Recently, this problem has been addressed partially via frequency tuning using post-fabrication techniques such as laser annealing [65–68], but further tolerance in design parameters is still desirable.

Here, we propose and experimentally demonstrate a drive-efficient single-excitation exchange interaction between two transmons that allows all-microwave controlled-Z (CZ) gate over a wide range of detuning between data transmons. In this scheme, the interaction is activated by applying a microwave drive to a coupler transmon whose third-order nonlinearity plays a central role. The process can be understood as four-wave mixing involving three qubits and a drive microwave photon. We have therefore named it Coupler-Assisted Swap (CAS) interaction or transition. Note that a similar mechanism is used to exchange a single photon between two cavities [69].

Remarkably, the CAS transition relies neither on the less-coherent higher energy levels outside the qubit subspace nor on the direct transverse coupling between the data transmons. At the same time, the latter can in turn be utilized for the suppression of unwanted ZZ coupling [62, 70]. This also widens the choice of the qubit detuning in the device design.

6.1   Theory

The circuit under consideration [Figs. 6.1(a) and (b)] consists of three fixed-frequency transmons, with the total Hamiltonian being modeled as coupled Duffing oscillators under the rotating-wave approximation,

$$\hat{H}/\hbar = \sum_i \left(\omega_i \hat{a}_i^\dagger \hat{a}_i + \frac{\alpha_i}{2} \hat{a}_i^\dagger \hat{a}_i^\dagger \hat{a}_i \hat{a}_i \right) + \sum_{i \neq c} g_{ic}(\hat{a}_i^\dagger \hat{a}_c + \hat{a}_i \hat{a}_c^\dagger), \tag{6.1}$$
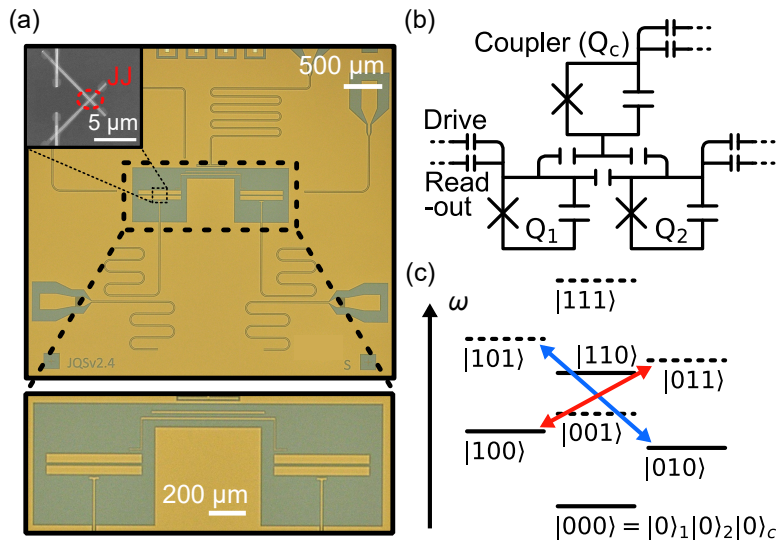
Figure 6.1: (a) Optical images of a fabricated superconducting circuit (top) and three coupled transmons (bottom). Most of the structures are made from TiN electrodes (yellow) on a Si substrate (gray). Inset: Scanning electron micrograph of an $Al/AlO_x/Al$ Josephson junction fabricated with the in-situ bandage technique [16]. (b) Equivalent circuit diagram of the coupled transmon system, where readout resonators, Purcell filters, and drive lines are omitted. Only the coupling capacitors connected to them are depicted. Q_1, Q_2, and Q_c represent the two data qubits and one coupler qubit, respectively. (c) Energy-level diagram of the system eigenstates $|ijk\rangle = |i\rangle_1 |j\rangle_2 |k\rangle_c$ ($i, j, k \in \{0, 1\}$) truncated to the first excited state of each transmon. The blue and red arrows are the CAS transitions activated by microwave drives. The dashed energy levels involve the single excitation of the coupler.

where $\hbar$ is the reduced Planck constant, ω_i and α_i ($i \in \{1, 2, c\}$) are the fundamental frequency and anharmonicity of each transmon, $\hat{a}_i$ and $\hat{a}_i^\dagger$ are the annihilation and creation operators, and g_{ic} is the transverse coupling strength between the data transmon Q_i and the coupler transmon Q_c. Here we assume the dispersive regime $|g_{ic}/\Delta_{ic}| \ll 1$, where $\Delta_{ic} = \omega_i - \omega_c$. For the moment, we omit the direct coupling between the data qubits, g_{12}, and consider up to the third excited state of each transmon.

To induce the interaction between the data qubits, we apply a microwave drive

$$\hat{H}_d/\hbar = \Omega_d \cos \omega_d t \left(\hat{a}_c^\dagger + \hat{a}_c\right) \tag{6.2}$$

to the coupler qubit, where ω_d and Ω_d are the drive frequency and amplitude, respectively. To find an analytical expression of the induced CAS interaction strength, we expand the drive term to the second order of g_{ic} using the Schrieffer-Wolff transformation [See Supplemental Material]. Then, we obtain the effective drive term in the Hamiltonian,

$$\hat{H}_d' \approx \hat{H}_d + [\hat{S}, \hat{H}_d] + \frac{1}{2}[\hat{S}_1, [\hat{S}_1, \hat{H}_d]], \tag{6.3}$$

where the anti-Hermitian operator $\hat{S} = \hat{S}_1 + \hat{S}_2$ fulfills the conditions

$$[\hat{H}_0, \hat{S}_1] + \hat{O}_1 = 0, \tag{6.4}$$

$$[\hat{H}_0, \hat{S}_2] + \hat{O}_2 = 0. \tag{6.5}$$

Here, $\hat{O}_1$ is the off-diagonal part of Eq. (6.1), corresponding to the coupling term, and $\hat{H}_0$ is the rest. $\hat{O}_2$ is the off-diagonal part of $\frac{1}{2}[\hat{O}_1, \hat{S}_1]$. The effective drive term, Eq. (6.3), due to the third-order nonlinearity of the coupler, contains many transition matrix elements between eigenstates in the Hilbert space spanned by the three transmons. Among them, we focus on the CAS transitions between data qubits assisted by the single-photon excitation of the nonlinear coupler, such as $|010\rangle \leftrightarrow |101\rangle$ and $|100\rangle \leftrightarrow |011\rangle$, respectively illustrated by the blue and red arrows in Fig. 6.1(c), where $|ijk\rangle = |i\rangle_1 |j\rangle_2 |k\rangle_c$ ($i, j, k \in \{0, 1\}$). Here, we refer to them as the blue and red CAS transitions at the frequencies of ω_b and ω_r, respectively. We also assume $\omega_1 > \omega_2$ without loss of generality. From Eq. (6.3), analytical expressions for the drive-induced oscillation frequencies are calculated under the rotating-wave approximation as

$$\Omega_b \approx 2\langle 010|\hat{H}_d'|101\rangle/\hbar$$
$$= \frac{2g_{1c}g_{2c}\alpha_c\Omega_d}{\Delta_{12}(\omega_c - \omega_1 + \alpha_c)(\omega_c - \omega_2)}, \tag{6.6}$$
$$\Omega_r \approx 2\langle 100|\hat{H}_d'|011\rangle/\hbar$$
$$= \frac{-2g_{1c}g_{2c}\alpha_c\Omega_d}{\Delta_{12}(\omega_c - \omega_2 + \alpha_c)(\omega_c - \omega_1)}, \tag{6.7}$$

respectively for the blue and red CAS transitions, where $\Delta_{12} = \omega_1 - \omega_2$. The CAS-based CZ gate can be realized by applying a resonant 2π-pulse of the blue (red) CAS transition, where the state $|010\rangle$ ($|100\rangle$) acquires the geometric phase of π after a round trip [71].

6.2   Experiment

In the experiment, we use a circuit consisting of three capacitively coupled fixed-frequency transmons [7], two $\lambda/4$ coplanar-waveguide (CPW) readout resonators and Purcell filters [41] for data transmons, and one $\lambda/2$-CPW readout resonator for the coupler transmon [Fig. 6.1(a)]. The device parameters are the following: The fundamental frequencies of the data transmons and the coupler transmon are $\omega_1/2\pi \simeq 5.641$ GHz, $\omega_2/2\pi \simeq$
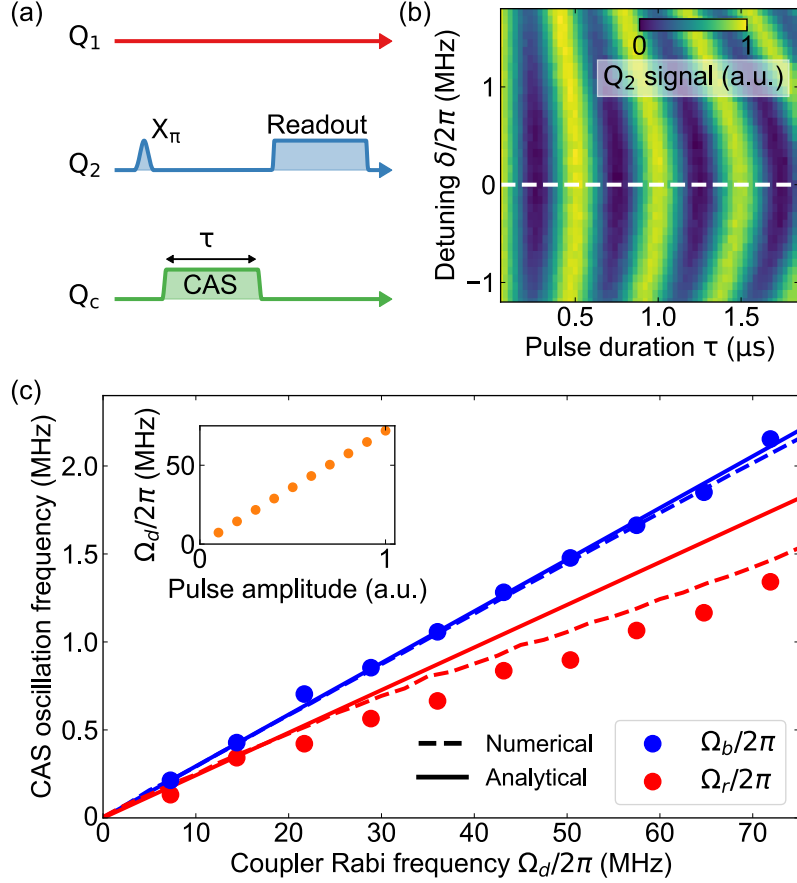
Figure 6.2: (a) Pulse sequence for the data transmons, Q_1 and Q_2, and the coupler transmon Q_c to measure the CAS oscillation frequency between the states indicated by the blue arrow in Fig. 6.1(c). To activate the transition, we prepare Q_2 in the first excited state with a π pulse, and then apply a drive pulse to the coupler. (b) Chevron pattern of the blue CAS transition as a function of the detuning $\delta = \omega_d - \omega_b$ and the pulse duration τ. The white dashed line, $\delta = 0$, shows the resonance condition for the blue CAS transition at $\omega_b/2\pi \simeq 6.4207$ GHz. The data is obtained for the coupler drive amplitude $\Omega_d/2\pi = 72$ MHz. Note that the blue CAS transition frequency ω_b depends on Ω_d through the ac Stark shift and the associated correlated oscillations of the excited-state populations of the three transmons are separately observed [See Supplemental Material]. (c) Blue and red CAS oscillation frequencies obtained from the fitting. The blue and red solid lines are analytical evaluations respectively using Eqs. (6.6) and (6.7) with experimentally-determined parameters. The dashed lines are the numerical simulations based on Eqs. (6.1) and (6.2) using QuTiP [72, 73]. Inset: Ω_d calibration result by driving the fundamental mode of the coupler qubit as a function of the pulse amplitude.

5.507 GHz and $\omega_c/2\pi \simeq 6.317$ GHz, respectively. The third-order nonlinearities of the transmons are $\alpha_1/2\pi \simeq -300$ MHz, $\alpha_2/2\pi \simeq -303$ MHz and $\alpha_c/2\pi \simeq -381$ MHz, and the transverse coupling strengths between the data transmons and the coupler transmon are $g_{1c}/2\pi \simeq 40$ MHz and $g_{2c}/2\pi \simeq 31$ MHz. The direct transverse coupling between data transmons is estimated to be $g_{12}/2\pi \simeq 1.9$ MHz by fitting the measurement result of the ZZ interaction, and the static ZZ interaction strength between data transmons is estimated as $\xi_0/2\pi \simeq -1.5$ kHz [See Supplemental Material]. The transmons, Q_1, Q_2 and Q_c, have energy relaxation times T_1 of $95\,\mu$s, $108\,\mu$s and $15\,\mu$s, Ramsey dephasing times T_2^* of $76\,\mu$s, $81\,\mu$s and $15\,\mu$s, and echo dephasing times T_2^e of $88\,\mu$s, $166\,\mu$s and $18\,\mu$s, respectively. Part of the reason for the lower coherence of the coupler transmon is presumably due to its narrower electrodes and concentrated electric field [74]. This can be improved by design modifications.

For single-qubit gates, we use a Gaussian pulse with its FWHM $\sigma = 7.5$ ns, total gate length 4σ, and with derivative removal by adiabatic modulation (DRAG) [75]. For the CAS transitions, we apply to the coupler a flat-top drive pulse with Gaussian-shaped edges of $\sigma = 10$ ns and a total edge length of 4σ.

We first measure the CAS oscillation frequencies as a function of the drive amplitude Ω_d. As shown in Fig. 6.2(a), for the blue CAS transition, we prepare the system in $|010\rangle$ and then apply a coupler drive with a given Ω_d and with various drive frequencies and pulse lengths. By fitting the resulting oscillations in the excited state population of Q_2 [Fig. 6.2(b)], we obtain the oscillation frequency Ω_b, which is plotted with blue dots in Fig. 6.2(c) as a function of Ω_d. Similarly, Ω_r for the red CAS transition is obtained.

To check the validity of our theoretical model, we also plot in Fig. 6.2(c) the analytically obtained values from Eqs. (6.6) and (6.7) and the numerical ones from Eqs. (6.1) and (6.2). For the blue CAS transition, our model is in good agreement with the experimental result. For the red CAS transition, the numerical calculation is also in good agreement with the experimental result, but the analytical model shows a deviation in the strong drive regime. This could be an off-resonant effect of a single-photon transition ($|110\rangle \leftrightarrow |201\rangle$) and two-photon transitions ($|000\rangle \leftrightarrow |002\rangle$, $|010\rangle \leftrightarrow |102\rangle$) near ω_r. The blue CAS oscillation frequency fits better as there are no near disturbing transitions on the higher frequency side of ω_c because of the negative anharmonicity of the transmon. This can be an advantage for relaxing the frequency crowding problem.

We next implement the CZ gate using the blue CAS transition. We first determine the relation between the CAS drive detuning and the pulse duration by fitting the chevron pattern with the drive amplitude $\Omega_d/2\pi = 75$ MHz, which is slightly larger than the experiments presented in Fig. 6.2 and the resulting blue CAS oscillation frequency is about 2.2 MHz. We then calibrate the amount of controlled phase shift using the Joint Amplification of ZZ (JAZZ) sequence [76, 77] shown in Fig. 6.3(a). In this sequence, Q_2 is detected in the excited state when the amount of the controlled phase shift is π and the final measurement angle ϕ is 0. By sweeping ϕ and fitting the result with a cosine function, the amount of the control phase is obtained from the phase shift of the cosine function. Figure 6.3(b) shows the obtained phase shift as a function of the CAS drive detuning. The optimal drive frequency and flat-top duration are obtained by interpolating the result. The associated local phase shift induced by the CAS drive on each qubit is evaluated and canceled with a virtual-Z gate [79] to implement the CAS-based CZ gate. Through the interleaved randomized benchmarking (IRB) [80] of the calibrated CAS-based CZ gate, a fidelity of 97.8(6)% is obtained [Fig. 6.3(d)]. The master-equation simulation with our device parameters yields 97.8% fidelity for the CZ gate, which is mainly limited by the short coherence time of the coupler qubit. This implies that the CAS-based CZ gate can be improved further by optimizing the design parameter and coherence time of the
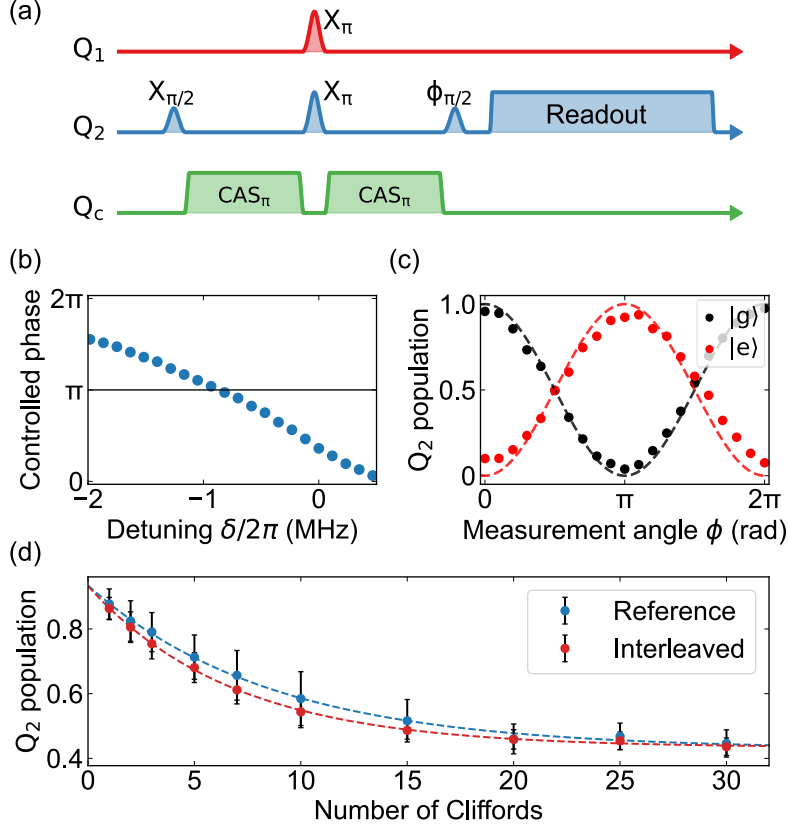
Figure 6.3: (a) Pulse sequence for measuring the control phase using the Joint Amplifica-tion of ZZ (JAZZ) protocol [76, 77]. The measurement angle ϕ is swept to find an optimal CAS drive frequency for the CZ gate. (b) Controlled phase measured as a function of $\delta = \omega_d - \omega_b$, where $\omega_b/2\pi \simeq 6.4157$ GHz for the drive amplitude of $\Omega_d/2\pi = 75$ MHz. For each drive frequency, we adjust the pulse length so that the coupler returns to the ground state. (c) Ramsey fringes measured with the calibrated detuning of the blue CAS drive. A π phase shift is observed depending on the states of the control transmon Q_1. The vertical axis is the signal of Q_2 normalized to the responses of the ground and excited states of Q_2. The black and red dashed curves represent the functions of the ideal CZ gate. (d) Inter-leaved randomized benchmarking (IRB). Blue and red dots are the averaged experimental results of the reference RB and IRB, respectively. The number of randomly-generated RB sequences used is 30, and the error bars represent 95% confidence. Dashed lines are fitting curves to the decay model. The horizontal axis is the number of Clifford gates applied. All single-qubit Clifford gates consist of two $X_{\pi/2}$ gates and three virtual-Z gates, and the length of the CZ gate is 504 ns. Thus, the average duration of the two-qubit Clifford gate is 945 ns, where each spacing between two successive pulses is set to 6 ns [78].
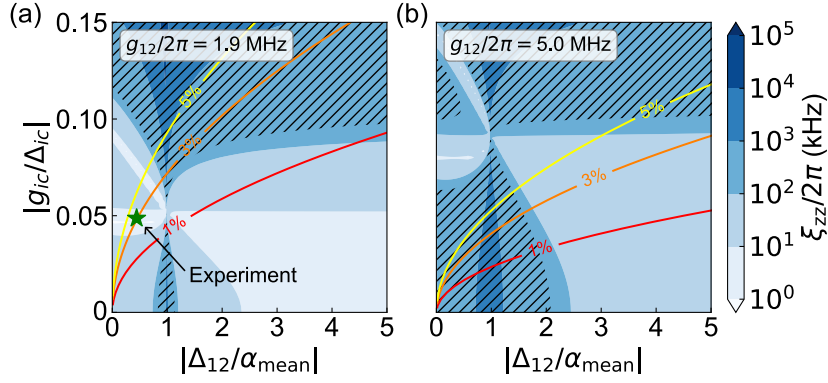
Figure 6.4: Residual ZZ interaction strength ξ_{ZZ} and the drive efficiency η_b of the blue CAS transition as a function of the detuning Δ_{12} and transverse coupling strength g_{ic} normalized by the mean anharmonicity $\alpha_{\mathrm{mean}} = (\alpha_1 + \alpha_2)/2$ and detuning Δ_{ic}, $(i \in \{1, 2\})$, respectively. Here, ξ_{ZZ} is calculated through numerical diagonalization of Eq. (6.1) (filled contour plot) using (a) the current and (b) prospective design parameters with the direct transverse coupling g_{12}. The drive efficiency is defined as $\eta_b = \Omega_b/\Omega_d$ from Eq. (6.6) (contour line plot). As the prospective design parameters, we set $(\omega_c - \omega_1)/2\pi = 0.6$ GHz, $\omega_2/2\pi = 5.0$ GHz, and $\alpha_i/2\pi = (-0.20, -0.20, -0.45)$ GHz for $i = (1, 2, c)$. The sweep parameters are ω_1 and $g_{1c}/\Delta_{1c} = g_{2c}/\Delta_{2c}$, and the shaded areas indicate the residual ZZ interaction strength larger than 150 kHz. The green star in (a) indicates the condition in the current experiment.

coupler.

6.3 Discussion

Finally, using Figs. 6.4(a) and (b), we discuss dependencies of the residual ZZ interaction strength between the data qubits, ξ_{ZZ}, and the drive efficiency of the blue CAS-based CZ gate rate, $\eta_b = \Omega_b/\Omega_d$, on the current and prospective design parameters. Here, we numerically diagonalize Eq. (6.1) to calculate the residual ZZ-interaction strength when the coupler is in the ground state. Note that in these calculations, the term $g_{12}(\hat{a}_1^\dagger \hat{a}_2 + \hat{a}_1 \hat{a}_2^\dagger)$, which has been ignored so far, is added to Eq. (6.1) to see the effect of direct coupling. As reported in previous studies [62, 70], the direct coupling g_{12} can suppress the residual ZZ interaction by canceling the one mediated by the coupler. As shown in Fig. 6.4(a), the straddling regime ($|\Delta_{12}/\alpha_{\mathrm{mean}}| < 1$) gives high drive efficiency and low residual ZZ interaction for the parameter set. On the other hand, we can also achieve practical performance far outside the straddling regime by selecting appropriate values of parameters, especially of g_{12}. In Fig. 6.4(b), we set $g_{12}/2\pi = 5$ MHz as an example. This parameter set enables implementation of the blue CAS-based CZ gates of 100–200 ns for $\Omega_d/2\pi = 200$ MHz in a wide range of the detuning ($2 \lesssim \Delta_{12}/\alpha_{\mathrm{mean}} \lesssim 4$) between the data transmons while keeping the residual ZZ coupling <100 kHz. The coherent error due to the residual ZZ interaction during the non-commuting single-qubit gates can be mitigated with an optimal-control pulse [81, 82] or a composite pulse robust to frequency shift [83, 84]. We can also apply an active residual ZZ interaction cancellation using an off-resonant microwave drive near the blue CAS transition [See Supplemental Material] or coupler-qubit transition [85].

Chapter 7

Spin-dependent force in a circuit-QED system

Achieving logical qubits requires significant overhead for physical and peripheral control systems. Bosonic codes have been proposed as an alternative to address this issue. According to their encoding procedures, a qubit is encoded into a multi-level system, such as a harmonic oscillator. Errors that occur in an encoded quantum state of the harmonic oscillator can be corrected by conditional manipulation using an auxiliary qubit, and it is possible to achieve a logical coherence time that exceeds the coherence time of any of the elements that make up the system. This is called break-even, as demonstrated in recent studies [86, 87]. They utilized a three-dimensional superconducting resonator and a transmon to achieve this breakthrough.

The conditional displacement gate plays an important role in the framework of bosonic codes. Recently, it has been regularly implemented by enhancing a weak cross-Kerr interaction by irradiating a pump tone into the resonator [86, 88, 89]. The cross-Kerr interaction is a valuable control resource and simple to implement but can act as a bit-flip error propagation channel during conditional gate operations. In addition, the pump tone increases the average number of photons in the resonator to 100–1000, amplifying the decoherence and self-Kerr term contributing to coherent errors. To address these issues, we present results on implementing the conditional displacement gate by harnessing the second-order nonlinearity of the cubic transmon [10], which is integrated into a planar superconducting circuit. In this approach, the resonator state follows the shortest path in its phase space, effectively decoupling the cross-Kerr interaction during conditional gate operations. In addition, it does not require a strong and resonant pump tone to the resonator. Using this gate, we also demonstrate the creation of cat states and squeezed vacuum states through modular measurements with post-selection. Please refer to the supplementary material for detailed performance comparisons between our and conventional methods.

7.1 Theory

Spin-dependent force [90] originally referred to an interaction between an ion's internal states and vibrational modes. One notable application of a spin-dependent force is the Mølmer-Sørensen gate [91], which is a high-fidelity implementation of the two-qubit gate in trapped ion systems [92, 93]. The time evolution caused by a spin-dependent force can be written as follows

$$\hat{U}_{\text{SDF}}(t) = |\uparrow\rangle\langle\uparrow|\hat{D}(\alpha(t)) + |\downarrow\rangle\langle\downarrow|\hat{D}(-\alpha(t)), \tag{7.1}$$

which can be interpreted as a displacement of a harmonic oscillator depending on an interacting spin state. Such time evolution can be realized using red- and blue-sideband transitions as follows

$$\text{Red-sideband transition} \; : \; |g, n+1\rangle \leftrightarrow |e, n\rangle,$$
$$\text{Blue-sideband transition} \; : \; |g, n\rangle \leftrightarrow |e, n+1\rangle.$$

These are also known as Jaynes-Cummings (JC) and anti-Jaynes-Cummings (anti-JC) interactions. The corresponding Hamiltonians are respectively as follows

$$\hat{H}_{\mathrm{r}}/\hbar = \Omega_r\big(\hat{a}\hat{\sigma}_+ + \hat{a}^\dagger\hat{\sigma}_-\big), \tag{7.2}$$

$$\hat{H}_{\mathrm{b}}/\hbar = \Omega_b\big(\hat{a}\hat{\sigma}_- + \hat{a}^\dagger\hat{\sigma}_+\big), \tag{7.3}$$

where Ω_r and Ω_b are the transition rates of the red- and blue-sideband, respectively. Assuming that $\Omega_r = \Omega_b \equiv \Omega_{\mathrm{SDF}}$, we can obtain a resource interaction of a spin-dependent force as follows

$$\hat{H}_{\mathrm{SDF}} = \hat{H}_{\mathrm{r}}/\hbar + \hat{H}_{\mathrm{b}}/\hbar = \sqrt{2}\Omega_{\mathrm{SDF}}\hat{\sigma}_x\hat{x}, \tag{7.4}$$

where $\hat{x} = \frac{\hat{a}+\hat{a}^\dagger}{\sqrt{2}}$ is a dimensionless position operator for the harmonic oscillator.

Two main ways to realize these interactions in superconducting circuits are parametric driving of DC-SQUID [94, 95] or combining an element with second-order nonlinearity such as a SNAIL with microwave driving via a capacitively coupled drive line [10, 96]. For the former, if the mutual inductance between the DC-SQUID and the 50Ω inductively coupled drive line ranges from 500 to 1500 fH, a power of -10 to -20 dBm is needed at the cryogenic temperature [95]. This results in high wiring costs and heating issues for the dilution refrigerator. On the other hand, the latter requires a DC bias, but only a power of -50 to -60 dBm is required at the cryogenic temperature when the coupling to the capacitive drive line is 100 Hz, which is relatively low power. Therefore, we implemented JC and anti-JC interactions using a SNAIL.

7.1.1   Derivation of spin-dependent force

As shown in Figs. 7.1(a) and (b), the circuit being considered consists of an ancillary cubic transmon, a host resonator for storing bosonic states, a readout resonator, and a Purcell filter. Ignoring the readout circuits, the system Hamiltonian can be modeled as follows

$$\hat{H}/\hbar = \omega_h\hat{a}^\dagger\hat{a} + \omega_{\mathrm{CT}}\hat{b}^\dagger\hat{b} + g_3\big(\hat{b}^\dagger + \hat{b}\big)^3 + g_4\big(\hat{b}^\dagger + \hat{b}\big)^4 + g_0(\hat{a}^\dagger\hat{b} + \hat{a}\hat{b}^\dagger), \tag{7.5}$$

where $\hbar$ is the reduced Planck constant, ω_h and ω_q are the fundamental frequencies of the host resonator and cubic transmon, respectively. $\hat{a}$ ($\hat{a}^\dagger$) and $\hat{b}$ ($\hat{b}^\dagger$) are the annihilation (creation) operator for the host resonator and cubic transmon, and g_0 is the transverse coupling strength between these modes. Ignoring two- and three-photon transition terms in the above Hamiltonian, we obtain the following Hamiltonian

$$\hat{H}/\hbar \approx \omega_h\hat{a}^\dagger\hat{a} + \omega_q\hat{b}^\dagger\hat{b} + \beta\big(\hat{b}^\dagger\hat{b}\hat{b} + \hat{b}^\dagger\hat{b}^\dagger\hat{b}\big) + \frac{\alpha}{2}\hat{b}^\dagger\hat{b}^\dagger\hat{b}\hat{b} + g_0(\hat{a}^\dagger\hat{b} + \hat{a}\hat{b}^\dagger), \tag{7.6}$$

where $\omega_q = \omega_{\mathrm{CT}} - \alpha$, $\alpha = 12g_4$, $\beta = 3g_3$ are introduced. To find an analytical expression of the sideband transition rates, we start by block diagonalizing the Hamiltonian to the second order of β/ω_q and g_0/Δ using the Schrieffer-Wolff transformation. The resulting Hamiltonian is

$$\hat{H}_{\mathrm{eff}} = \hat{H}_0 + \frac{1}{2}[\hat{S}_1, \hat{V}] + [\hat{S}_2, \hat{H}_0]. \tag{7.7}$$

Here, $\hat{H}_0$ is the diagonal part of Eq. (7.6), and $\hat{V}$ is the rest, corresponding to the transverse coupling and cubic nonlinearity terms. Anti-Hermitian operators $\hat{S}_1$ and $\hat{S}_2$ are given as solutions of the following equations

$$[\hat{H}_0, \hat{S}_1] + \hat{V} = 0, \tag{7.8}$$

$$[\hat{H}_0, \hat{S}_2] + \hat{O}_2 = 0, \tag{7.9}$$

where $\hat{O}_2$ is the off-block diagonal part of $\frac{1}{2}[\hat{S}_1, \hat{V}]$. We consider up to the third level for the cubic transmon, and the explicit forms of $\hat{S}_1$ and $\hat{S}_2$ are as follows

$$\hat{S}_1/\hbar = \frac{g_0}{\Delta}|e\rangle\langle g|\hat{a} + |f\rangle\langle e|\left(\frac{\sqrt{2}g_0}{\Delta + \alpha}\hat{a} + \frac{\sqrt{2}\beta}{\omega_q + \alpha}\right) - h.c., \tag{7.10}$$

$$\hat{S}_2/\hbar = |f\rangle\langle g|\left(\frac{\sqrt{2}\alpha g_0^2\hat{a}^2}{2\Delta(\alpha + \Delta)(\alpha + 2\Delta)} + \frac{\sqrt{2}\beta g_0(\alpha + \omega_r)\hat{a}}{2\Delta(\alpha + \omega_q)(\alpha + 2\Delta - \omega_r)}\right) - h.c., \tag{7.11}$$

where $\Delta = \omega_q - \omega_r$. Furthermore, the two-level approximation for the cubic transmon yields the following Hamiltonian

$$\hat{H}_{\mathrm{eff}}/\hbar \approx (\tilde{\omega}_r + \chi\hat{\sigma}_z)\hat{a}^\dagger\hat{a} - \frac{\tilde{\omega}_q}{2}\hat{\sigma}_z + g_{\mathrm{rp}}|e\rangle\langle e|(\hat{a} + \hat{a}^\dagger). \tag{7.12}$$

Here, $\tilde{\omega}_r = \omega_r + \frac{g_0^2}{\Delta+\alpha}$ and $\tilde{\omega}_q = \omega_r - \frac{g_0^2}{\Delta} + \frac{2\beta^2}{\omega_q+\alpha}$ are the Lamb-shifted host resonator and cubic transmon frequencies, respectively. $g_{\mathrm{rp}} = \frac{\beta g_0(2\alpha + 2\Delta - \omega_r)}{(\alpha+\omega_q)(\alpha+\Delta)}$ is an artificial radiation pressure interaction due to the cubic nonlinearity of the SNAIL. $\chi = \frac{g_0^2\alpha}{\Delta(\Delta+\alpha)}$ is the dispersive shift. To activate the sideband transitions shown in Fig. 7.1(c), we apply a microwave drive

$$\hat{H}_d/\hbar = \Omega_d \cos(\omega_d t + \phi_d)(\hat{b}^\dagger + \hat{b}), \tag{7.13}$$

to the cubic transmon. Here, Ω_d, ω_d, and ϕ_d are the drive amplitude, frequency, and phase, respectively. By using the BCH formula and transforming the drive terms with $\hat{S}_1$ and $\hat{S}_2$, we obtain the following effective drive terms

$$\hat{H}'_d \approx \hat{H}_d + [\hat{S}_1 + \hat{S}_2, \hat{H}_d] + \frac{1}{2}[\hat{S}_1, [\hat{S}_1, \hat{H}_d]],$$

$$\approx \hbar\Omega_d \cos(\omega_d t + \phi_d)(\eta_r\hat{\sigma}_-\hat{a}^\dagger + \eta_b\hat{\sigma}_-\hat{a}) + h.c.. \tag{7.14}$$

For the second line, the two-level approximation is used. η_b and η_r represent transition efficiencies of the red- and blue-sideband transitions and can be written as follows

$$\eta_r = \frac{\beta g_0}{(\omega_q - \alpha)(\Delta - \alpha)}\left(\frac{2(\Delta - \alpha)}{\omega_r + 2\Delta - \alpha} - \frac{2\alpha}{\Delta} + 1\right), \tag{7.15}$$

$$\eta_b = \frac{-\beta g_0}{(\omega_q - \alpha)(\Delta - \alpha)}. \tag{7.16}$$

Therefore, by setting $\omega_d = \tilde{\omega}_q - \tilde{\omega}_r$ or $\omega_d = \tilde{\omega}_q + \tilde{\omega}_r$, we can activate the JC and anti-JC interactions in the rotating frame. Moreover, by irradiating microwaves of these frequencies simultaneously, the resource Hamiltonian for the spin-dependent force in the rotating frame can be realized as follows

$$\hat{H}_{\mathrm{SDF}} = \frac{\Omega'}{2}(e^{-i\phi_r}\hat{\sigma}_-\hat{a}^\dagger + e^{-i\phi_b}\hat{\sigma}_-\hat{a}) + h.c.,$$

$$= \frac{\sqrt{2}\Omega'}{2}\hat{\sigma}_{\phi_\Sigma}\hat{x}_{\phi_\Delta}, \tag{7.17}$$

$$\hat{\sigma}_{\phi_\Sigma} = \hat{\sigma}_x \cos\phi_\Sigma + \hat{\sigma}_y \sin\phi_\Sigma, \tag{7.18}$$

$$\hat{x}_{\phi_\Sigma} = \hat{x}\cos\phi_\Delta + \hat{p}\sin\phi_\Delta, \tag{7.19}$$

where we assume the same rates for red- and blue-sideband transitions. $\hat{x} = \frac{\hat{a}+\hat{a}^\dagger}{\sqrt{2}}$ and $\hat{p} = \frac{\hat{a}-\hat{a}^\dagger}{\sqrt{2}i}$ are dimensionless position and momentum operators for the host resonator, respectively. In addition, relative phases between the red- and blue-sideband microwave drives are introduced as $\phi_\Sigma = -\frac{\phi_r+\phi_b}{2}$ and $\phi_\Delta = -\frac{\phi_r-\phi_b}{2}$. The rotating wave approximation can eliminate the last term for Eq. (7.12). However, the dispersive coupling cannot be eliminated, and Eq. (7.17) is modified in the rotating frame as follows

$$\hat{H}'_{\mathrm{SDF}}/\hbar = \chi\hat{\sigma}_z\hat{a}^\dagger\hat{a} + \frac{\sqrt{2}\Omega'}{2}\hat{\sigma}_{\phi_\Sigma}\hat{x}_{\phi_\Delta}. \tag{7.20}$$

The first and second terms are non-commutative, and the dispersive interaction is a source of coherent errors. To address the problem, we decouple the dispersive interaction by adding a drive tone to the carrier transition ($|g\rangle \leftrightarrow |e\rangle$). Then, we consider the following Hamiltonian

$$\hat{H}_{\mathrm{rc}}/\hbar = \chi\hat{\sigma}_z\hat{a}^\dagger\hat{a} + \frac{\Omega_c}{2}(\hat{\sigma}_x\cos\phi_c + \hat{\sigma}_y\sin\phi_c)$$
$$+ \frac{\Omega_r}{4}\big((\hat{a}^\dagger e^{i\phi_r} + \hat{a}e^{-i\phi_r})\hat{\sigma}_x + (\hat{a}^\dagger e^{i\phi_r} - \hat{a}e^{-i\phi_r})\hat{\sigma}_y\big), \tag{7.21}$$
$$= \chi\hat{\sigma}_z\hat{a}^\dagger\hat{a} + \frac{\Omega_c}{2}(\hat{\sigma}_x\cos\phi_c + \hat{\sigma}_y\sin\phi_c) + \frac{\sqrt{2}\Omega_r}{4}(\hat{\sigma}_x\hat{x}_{\phi_r} + \hat{\sigma}_y\hat{p}_{\phi_r}). \tag{7.22}$$

Here, Ω_c and ϕ_c are the drive amplitude and phase of the carrier transition. Using the following unitary matrix

$$\hat{P} = \frac{1}{\sqrt{2}}\begin{pmatrix} -e^{i\phi_c} & 1 \\ e^{i\phi_c} & 1 \end{pmatrix}, \tag{7.23}$$

we transform the basis so that the second term is diagonalized as follows

$$\hat{H}^+_{\mathrm{rc}}/\hbar = \hat{P}\hat{H}_{\mathrm{rc}}\hat{P}^\dagger/\hbar,$$
$$= \chi(\hat{\sigma}_x\cos\phi_c - \hat{\sigma}_y\sin\phi_c)\hat{a}^\dagger\hat{a} - \frac{\Omega_c}{2}\hat{\sigma}_z$$
$$- \frac{\sqrt{2}\Omega_r}{4}\big((\hat{\sigma}_z\cos\phi_c - \hat{\sigma}_y\sin\phi_c)\hat{x}_{\phi_r} + (\hat{\sigma}_z\sin\phi_c + \hat{\sigma}_y\cos\phi_c)\hat{p}_{\phi_r}\big). \tag{7.24}$$

Then, moving to the reference frame rotating at the Rabi frequency Ω_c and applying the rotating wave approximation, we obtain the following effective Hamiltonian

$$\hat{H}^+_{\mathrm{SDF}}/\hbar \approx -\frac{\sqrt{2}\Omega_r}{4}\hat{\sigma}_z(\hat{x}_{\phi_r}\cos\phi_c + \hat{p}_{\phi_r}\sin\phi_c), \tag{7.25}$$

where $\Omega_c \gg \Omega_r$ and $\Omega_c \gg \chi$ are assumed. Returning to the original rotating frame by inverse unitary transformations, the above Hamiltonian can be written as follows

$$\hat{H}^{\mathrm{eff}}_{\mathrm{SDF}}/\hbar = \frac{1}{2}(\hat{\sigma}_x\cos\phi_c + \hat{\sigma}_y\sin\phi_c)\left[\Omega_c + \frac{\sqrt{2}\Omega_r}{2}(\hat{x}_{\phi_r}\cos\phi_c + \hat{p}_{\phi_r}\sin\phi_c)\right]. \tag{7.26}$$

As an example, if $\phi_c = 0$, the above can be written as follows

$$\hat{H}^{\mathrm{eff}}_{\mathrm{SDF}}/\hbar = \frac{\Omega_c}{2}\hat{\sigma}_x + \frac{\sqrt{2}\Omega_r}{4}\hat{\sigma}_x\hat{x}_{\phi_r}, \tag{7.27}$$

and the spin-dependent force is realized. Note that the first and second terms are commutative; thus, the first term does not affect the time evolution of the spin-dependent force.
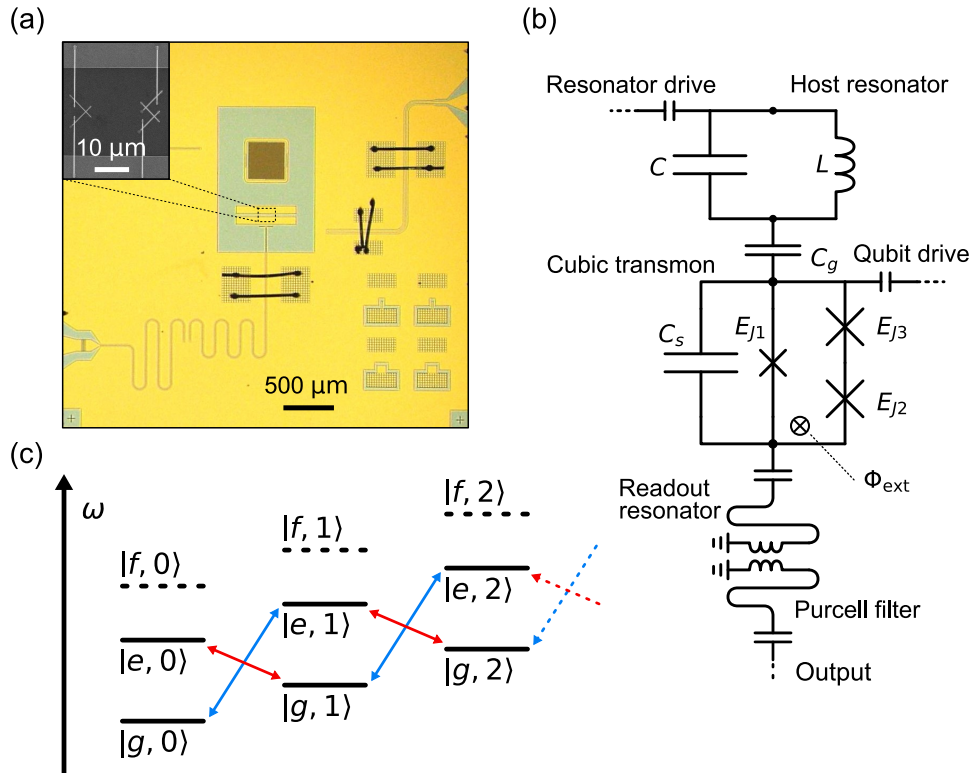
Figure 7.1: (a) Optical images of a fabricated superconducting circuit. Most structures are made from TiN electrodes (yellow) on a Si substrate (gray). Inset: Scanning electron micrograph of $Al/AlO_x/Al$ Josephson junctions fabricated with the in-situ bandage technique [16]. (b) Equivalent circuit diagram, where drive lines are omitted and only the coupling capacitors connected to them are depicted. (c) Energy-level diagram of the system eigenstates $|i, j\rangle = |i\rangle_q |j\rangle_h$, where $i \in \{g, e, f\}$ is a label for the eigenstates of the cubic transmon and j is a label for the Fock states of the host resonator. The blue and red arrows are red- and blue-sideband transitions activated by microwave drives. The dashed energy levels are not actively used in the experiment.

7.1.2   Tomography method for bosonic states

This chapter will demonstrate the spin-dependent force implementation by generating a cat state and squeezed vacuum states by the measurement backaction. State tomography on these bosonic states is needed to evaluate the generated states in a harmonic oscillator. Thus, two methods are described here, one measuring a characteristic function [97] and the other using a sideband Rabi oscillation [98, 99].

Characteristic function tomography

The characteristic function for the single harmonic oscillator is defined as the expectation value of the displacement operator as follows

$$
\begin{aligned}
\mathcal{C}(\alpha) &= \langle \hat{D}(\alpha) \rangle, \\
&= \mathrm{Tr}\left[\hat{D}(\alpha)\hat{\rho}_\mathrm{h} \right], \\
&= \mathrm{Tr}\left[\cos\left(\sqrt{2}\hat{\Omega}\right)\hat{\rho}_\mathrm{h} \right] + i\mathrm{Tr}\left[\sin\left(\sqrt{2}\hat{\Omega}\right)\hat{\rho}_\mathrm{h} \right].
\end{aligned}
\tag{7.28}
$$

where $\hat{\Omega} = \mathrm{Im}[\alpha]\hat{x} - \mathrm{Re}[\alpha]\hat{p}$ is introduced [See Supplemental Material for further details], and $\hat{\rho}_\mathrm{h}$ is a state of the harmonic oscillator. The Wigner function can be obtained from the characteristic function using a two-dimensional Fourier transformation as follows [97]

$$
W(\beta) = \frac{1}{\pi^2} \int \mathcal{C}(\alpha)e^{\beta\alpha^* - \beta^*\alpha}d^2\beta.
\tag{7.29}
$$

Thus, the characteristic function is a complete description of the quantum state of the single harmonic oscillator. Using an auxiliary qubit and the spin-dependent force, the characteristic function can be measured with the circuit shown in Fig. 7.2. For two initial states of the auxiliary qubit, the expectation values of the z-basis measurements are given by

$$
\langle \hat{\sigma}_z \rangle =
\begin{cases}
\mathrm{Tr}\left[\cos\left(\sqrt{2}\hat{\Omega}\right)\hat{\rho}_\mathrm{h} \right], & \text{for } \hat{R}_x(0)|g\rangle_\mathrm{q} = |g\rangle_\mathrm{q}, \\[2mm]
\mathrm{Tr}\left[\sin\left(\sqrt{2}\hat{\Omega}\right)\hat{\rho}_\mathrm{h} \right], & \text{for } \hat{R}_x(\pi/2)|g\rangle_\mathrm{q} = |+i\rangle_\mathrm{q}.
\end{cases}
\tag{7.30}
$$

where we assumed that the initial state is the product state, and $\hat{R}_x(\theta) = \cos(\theta/2)\hat{I} + i\sin(\theta/2)\hat{\sigma}_x$ is a single qubit gate for arbitrary x-axis rotation. Therefore, the characteristic function (7.28) can be fully characterized by running this circuit for each initial state of the auxiliary qubit.
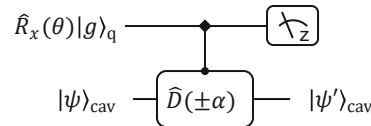

Figure 7.2: Characteristic function measurement circuit.

Fock basis tomography

The next method uses the dependence of the sideband transition rate on the number of photons in the resonator. Assuming that the photon number distribution of the resonator

is $\{P_n\}$, the following equation expresses the red-sideband Rabi oscillation of the auxiliary qubit,

$$P_g(t) = \frac{1}{2}\left[1 + \sum_n P_n \cos\left(\sqrt{n}\Omega_r t\right)e^{-\gamma_n t}\right].$$

(7.31)

Here, γ_n is the photon number-dependent decoherence rate. Thus, as shown in Fig. 7.3, it is possible to estimate the photon number distribution of the resonator by measuring the sideband Rabi oscillations of the auxiliary qubit after displacing the resonator state by several amplitudes [98, 99].
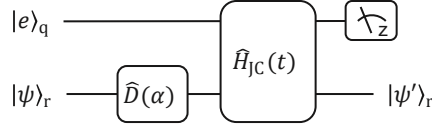
Figure 7.3: Fock basis tomography circuit.

7.1.3 State preparation

Here, we describe a method for manipulating states in the resonator and preparing specific states using a spin-dependent force. For the cat state preparation, when the spin-dependent force is applied to the ground state of the system, the following state can be obtained from Eq. (7.1),

$$|g\rangle\frac{|\alpha\rangle + |-\alpha\rangle}{2} + |e\rangle\frac{|\alpha\rangle - |-\alpha\rangle}{2}.$$

(7.32)

Thus, when the auxiliary qubit is measured in the ground state, the cat state can be prepared as follows

$$|+\text{cat}\rangle = \frac{|\alpha\rangle + |-\alpha\rangle}{2}.$$

(7.33)

In the following experiment, only the data measured in the ground state in the first measurement by running the circuit shown in Fig. 7.4 are used for tomography data processing.
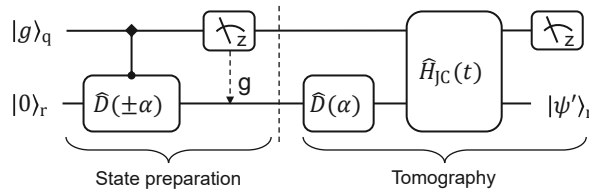
Figure 7.4: Cat state preparation and Fock basis tomography circuit.

Next, we describe how to prepare the squeezed vacuum state. For simplicity, we assume that the initial state is the product state and the auxiliary qubit is in the ground state. The back action to the resonator when the auxiliary qubit is measured in the ground state after applying the spin-dependent force can be written as follows

$$\frac{\hat{D}(\alpha) + \hat{D}(-\alpha)}{2} = \cos\left(\sqrt{2}(\text{Im}[\alpha]\hat{x} + \text{Re}[\alpha]\hat{p})\right)$$

(7.34)

$$= \cos\left(\sqrt{2}\hat{\Omega}\right).$$

(7.35)

Repeating this measurement N times as shown in Fig. 7.5, the state of the resonator can be written as follows

$$|\psi^N\rangle_r = \cos^N\left(\sqrt{2}\alpha\hat{x}\right)|0\rangle_r, \tag{7.36}$$

where α is assumed to be an imaginary number. Assuming that $|\alpha|$ is sufficiently smaller than 1, the periodicity of the cosine function can be neglected, and the state of the resonator is gradually squeezed with the number of measurements as shown in Fig. 7.6. Note that we assume that the auxiliary qubit is measured in the ground state at each repetition. In addition, from Eq. (7.28), the expectation value of the z-basis measurement of the auxiliary qubit can be written as follows

$$\langle\hat{\sigma}_z\rangle = \mathrm{Tr}\left[\cos\left(\sqrt{2}\alpha\hat{x}\right)|\psi^N\rangle\langle\psi^N|_r\right]. \tag{7.37}$$

Thus, the probability of measuring the auxiliary qubit in the ground state increases as the squeeze level increases.
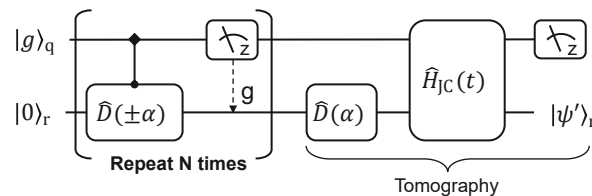
Figure 7.5: Squeezed vacuum state preparation and Fock basis tomography circuit.
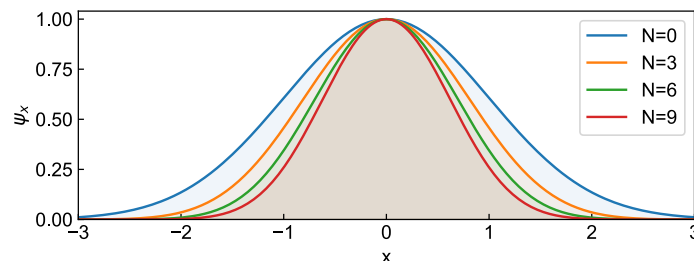
Figure 7.6: Normalized wave functions of the resonator states in position basis. The initial state is the vacuum state. N is the number of repetitions shown in Fig. 7.5. Here, the amplitude of a spin-dependent force is $|\alpha| = 0.3$.

7.2   Experiment

In the experiment, we use a circuit consisting of a capacitively coupled cubic transmon and a lumped element host resonator. For state discrimination of the cubic transmon, we use a $\lambda/4$ coplanar-waveguide (CPW) readout resonator and a Purcell filter as shown in Figs. 7.1(a) and (b). Table 7.1 lists the measured parameters.

We first measure the red- and blue-sideband Rabi oscillation frequencies changing the drive amplitude A_d as shown in Figs. 7.7(a) and (b). In the experiment, we prepare the system in $|e, 0\rangle$ for the red-sideband transition and then apply a microwave drive to the cubic transmon also, sweeping drive frequency and pulse length. By fitting the resulting oscillations in the excited state population, we obtain the oscillation frequencies Ω_r as shown in Fig. 7.8. Similarly, by preparing the system in $|g, 0\rangle$ and applying a microwave

drive to the cubic transmon, the oscillation frequencies Ω_b for the blue-sideband transition are obtained.

The original plan was to implement the spin-dependent force using only the red and blue sideband transitions. However, as mentioned above, the dispersive coupling acts as a coherent error, making calibration difficult. Therefore, we changed the method and implemented a spin-dependent force using the red-sideband and carrier transitions, as explained above. The experimental carrier Rabi frequency to implement the spin-dependent force is about 30 MHz, and the Rabi frequency of the red-sideband transition is about 1.0 MHz. Resonant microwave drives are simultaneously applied to these transitions to induce the spin-dependent force. Although their resonance frequencies could deviate from the separately evaluated frequencies due to the ac Stark shift, the carrier transition is fast enough and the resonance condition shift is negligible compared to the shift of the red-sideband transition frequency. Therefore, as shown in Figs. 7.9 (a) and (b), we measured the population of the auxiliary qubit for the initial states $|g\rangle$ and $|e\rangle$ while changing the red-sideband drive frequency. In the case of an ideal spin-dependent force, if it is strong enough, the auxiliary qubit and the resonator are maximally entangled, and the visibility of the qubit signal disappears. This phenomenon is experimentally observed, as shown in Fig. 7.9 (c). In the figure, the solid lines show the ideal numerical simulation results depending on the initial states. However, the experimental values differ from the ideal cases, most likely due to the strong carrier drive and the small nonlinearity of the cubic transmon, causing the two-level approximation to be on the verge of breaking.

Next, the sequence shown in Fig. 7.10 (a) is conducted for more accurate calibration, sweeping the carrier transition and red-sideband transition drive frequencies and pulse lengths. The red-sideband drive phase of the second half of the spin-dependent force is inverted, and this sequence should be an identity operation. The system ground state is the initial state for this experiment. The optimal drive frequencies result in the slowest rate of purity decay. The black lines in Figs. 7.10 (b) and (c) represent this condition.

To calibrate the displacement length of the resonator, we conduct the sequence shown in Fig. 7.3 and fit the resulting photon number-dependent Rabi oscillations by the following equation

$$P_g(t) = \frac{A}{2} \left[1 + \sum_n P'_n \cos\left(\sqrt{n}\Omega'_r t\right) e^{-\gamma' t/\sqrt{n}} \right]. \tag{7.38}$$

Here, the photon number distribution $\{P'_n\}$ is generated from the following density operator

$$\hat{D}(\alpha')\hat{\rho}_{\text{th}}\hat{D}^\dagger(\alpha'), \tag{7.39}$$

where $\hat{\rho}_{\text{th}}$ is the thermal state of the resonator, and the number of thermal photons is $n_{\text{th}} = 0.045(16)$ from the red-sideband Rabi oscillation when no drive is applied to the resonator. In addition, the fitting variables α', A, Ω'_r, and γ'_n are displacement length, visibility, fundamental frequency, and decay rate of the red-sideband Rabi oscillation, respectively. Fig. 7.11 (a) and (b) show the calibration results and an example of the fitting result when the pulse amplitude is $A_d = 0.56$.

Using the previous results, Fig. 7.12 shows the Fock basis tomography result of the cat state generated by executing the sequence in Fig. 7.4. The average photon number is about 1.8.

Finally, the results of squeezed vacuum state generation by repeated modular measurements are shown in Figs. 7.13 and 7.14. For data processing, only the results are used when the auxiliary qubit is observed in the ground state for each measurement. As squeezing continues, the probability of being observed in the excited state decreases as

Table 7.1: Measured sample parameters used for the experiments.

Cubic transmon		
Flux bias point	Φ_{ext}	$-0.2 \times \Phi_0$
$|g\rangle$–$|e\rangle$ transition frequency	$\tilde{\omega}_q/2\pi$	6577 MHz
Anharmonisity	$\alpha/2\pi$	-154 MHz
$|g\rangle$–$|e\rangle$ energy relaxation time	T_1	61 ± 12 μs
$|g\rangle$–$|e\rangle$ ramsey dephasing time	T_2^*	8 ± 1 μs
$|g\rangle$–$|e\rangle$ echo dephasing time	T_2^e	21 ± 1 μs
Single-qubit gate length (gaussian)	$T_{\text{g}} := 2\sigma$	20 ns
Single-qubit average gate fidelity	F_{avg}	0.9973(4)
$|g\rangle$–$|e\rangle$ assignment fidelity (post selected)	F_{a}	0.9973
$|g\rangle$–$|e\rangle$ QND fidelity (post selected)	F_{QND}	0.9905
$|e\rangle$ thermal excitation	P_e^{th}	0.005
Host resonator		
Resonator frequency (dressed)	$\tilde{\omega}_h/2\pi$	4322 MHz
Dispersive shift	$\chi_{\text{qh}}/2\pi$	-61 kHz
$|0\rangle$–$|1\rangle$ energy relaxation time	T_1	63 ± 7 μs
$|0\rangle$–$|1\rangle$ ramsey dephasing time	T_2^*	96 ± 22 μs
Thermal photon number	n_{th}	0.045 ± 0.016
Readout resonator		
Resonator frequency (dressed)	$\tilde{\omega}_r/2\pi$	7575 MHz
Dispersive shift	$\chi_{\text{qr}}/2\pi$	-1.9 MHz
Resonator external decay rate	$\kappa_{\text{ext}}/2\pi$	1.5 MHz
Readout pulse length	T_r	200 ns
Readout pulse integration window	T_{samp}	500 ns

expected. In addition, Fock basis tomography was also performed for $N =4$, 7, and 10, and finally, about 6 dB squeezing was confirmed.

7.3　Discussion

We have realized a spin-dependent force in the planar superconducting circuit using the three-wave mixed interaction provided by SNAIL. In addition, we used this spin-dependent force to prepare cat and squeezed vacuum states.

　　The method used in this study employs the carrier transition to decouple the dispersive coupling. However, the carrier transition rate must be sufficiently large compared to the red-sideband transition rate. This has the side effect that the two-level approximation is no longer valid due to the weak nonlinearity of the cubic transmon. A solution to this problem is to use the blue-sideband transition simultaneously. Since the red- and blue-sideband transitions can realize a spin-dependent force without any approximation, the condition that the carrier transition rate is sufficiently large relative to the sideband transition rate is no longer necessary, and the carrier transition rate should be large only for dispersive coupling. For more detailed discussions, please refer to the supplementary materials. We plan to conduct further experiments with this strategy in the future.
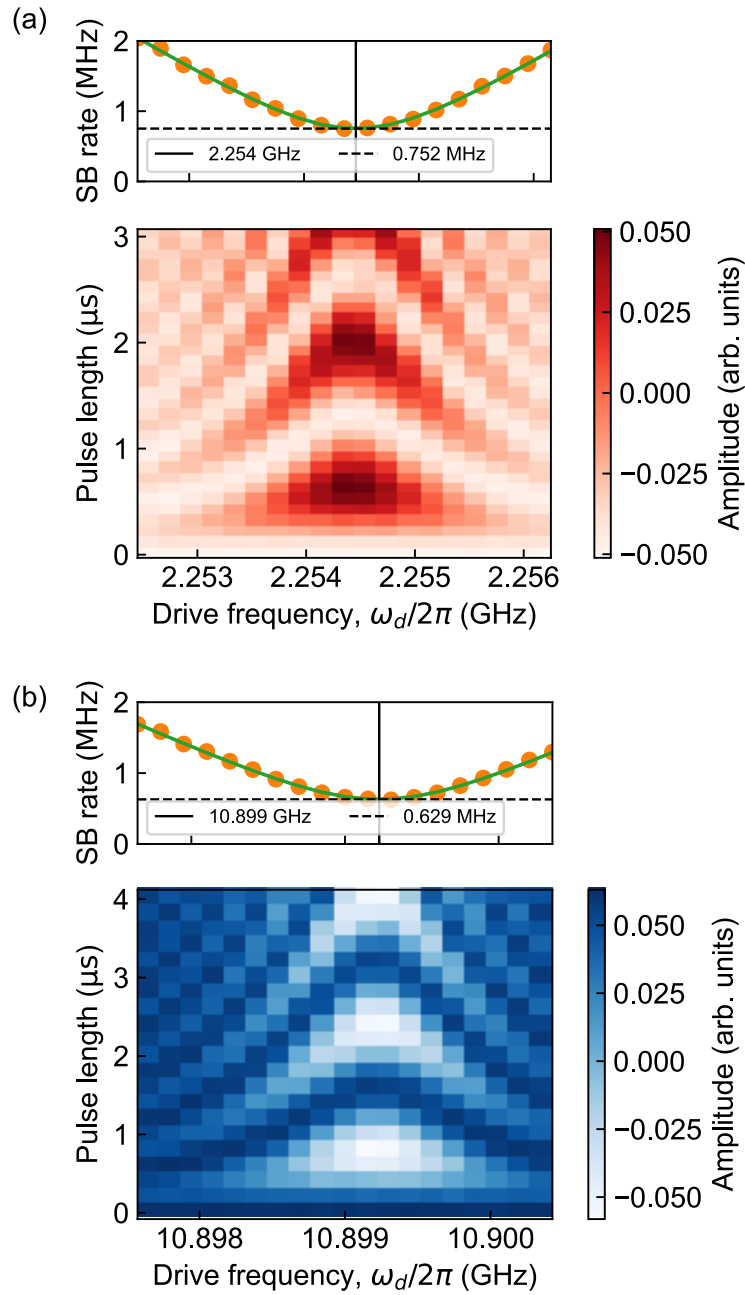
Figure 7.7: Chevron patterns of the red- and blue-sideband transitions as a function of the ω_d and the drive pulse length. The black solid and dashed lines in each upper panel represent the resonance condition and its corresponding oscillation frequency, and the green line shows the fitting result by $\sqrt{\Delta_d^2 + \Omega_i^2}$, $i \in \{\text{r}, \text{b}\}$, where $\Delta_d = \omega_i - \omega_d$. (a) Result for the red-sideband transition. (b) Result for the red-sideband transition.
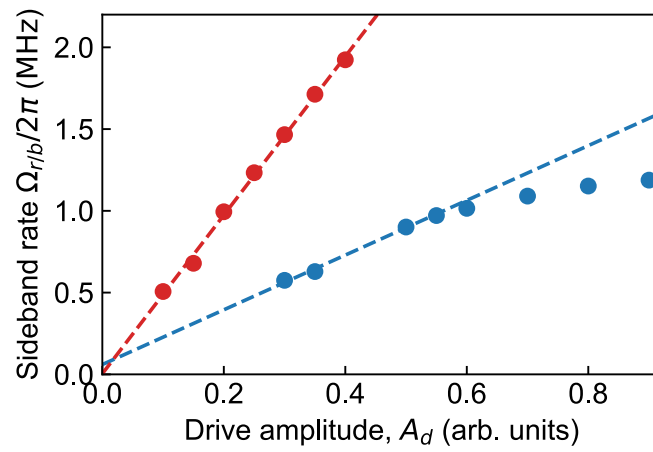
Figure 7.8: Dependence of sideband transition rates on drive amplitude. Red points indicate experimental values for the red-sideband transitions. The blue points indicate experimental values for the blue-sideband transitions. The dashed red line is the linear fit result. The dashed blue line is the linear fit result using the first three points.
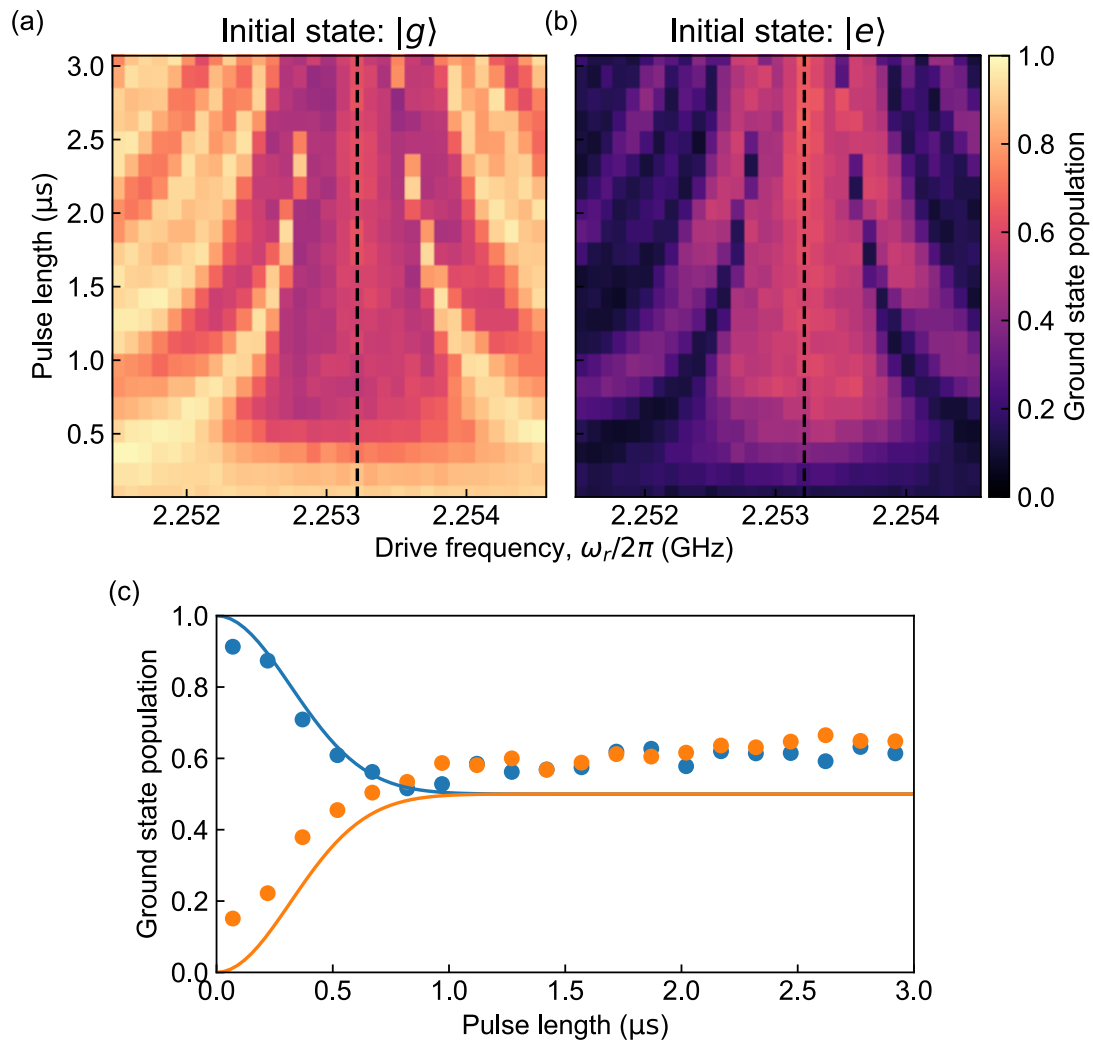
Figure 7.9: Calibration of the ac Stark shifted red-sideband transition frequency. The initial state of the resonator is the ground state and the auxiliary qubit is prepared in the ground (a) or first excited state (b). (c) Time evolution with the calibrated red-sideband transition frequency. The blue and orange points correspond to the black dashed lines in (a) and (b). The blue and orange solid lines show the simulation results of the time evolution with the ideal spin-dependent force, neglecting the dispersive coupling.
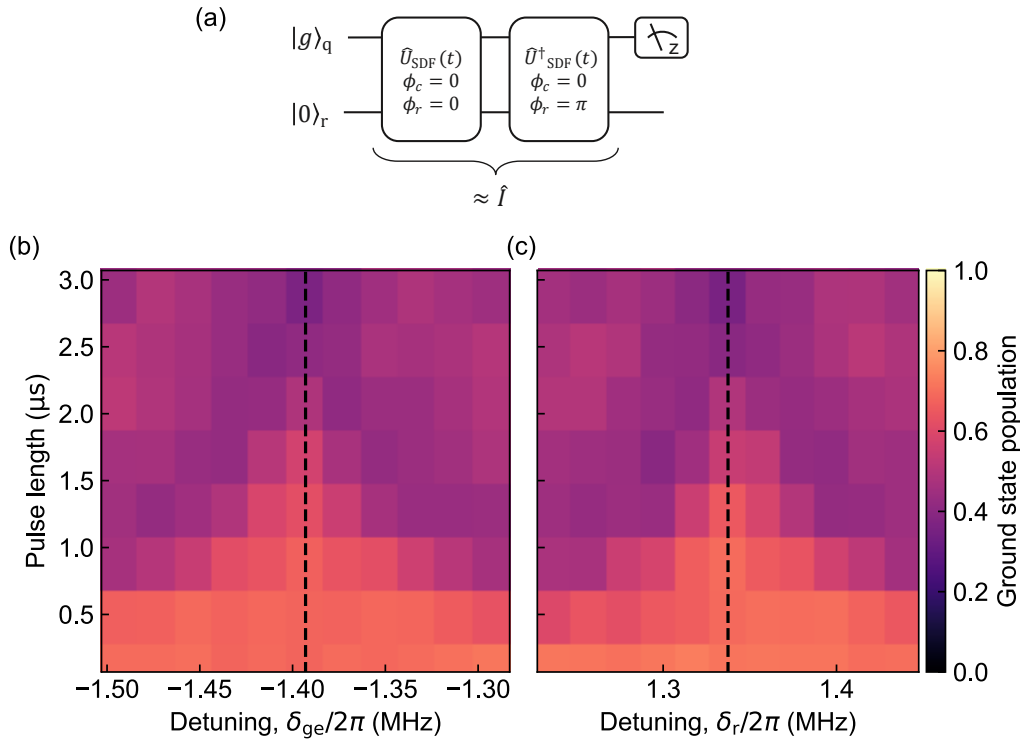
Figure 7.10: Accurate carrier and red-sideband transition frequency calibration results. (a) Gate Sequence. Measuring the probability of the auxiliary qubit returning to the ground state by applying spin-dependent force and its inverse to the ground state of the system. Results of detuning from the individual calibration results for the carrier (b) and red-sideband (c) transition frequencies.
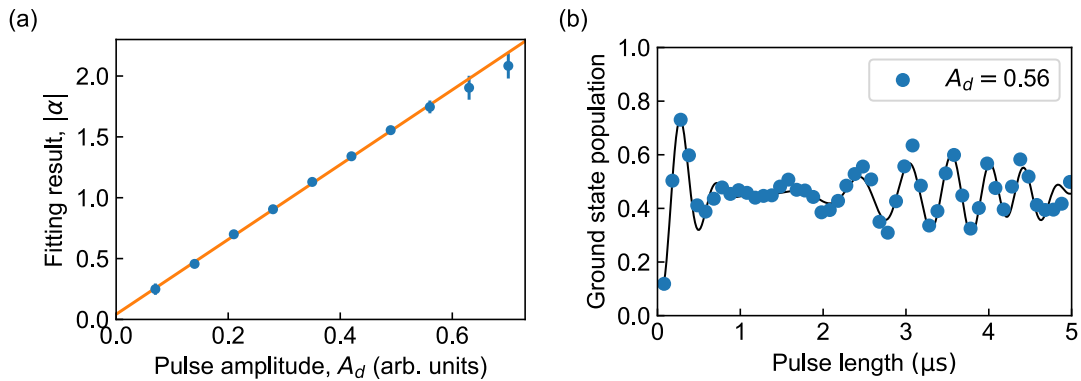
Figure 7.11: (a) Relation between the local displacement and microwave pulse amplitude, A_d, applying to the resonator. (b) Example of the fitting result by the photon number dependent Rabi oscillation function when the amplitude $A_d = 0.56$.
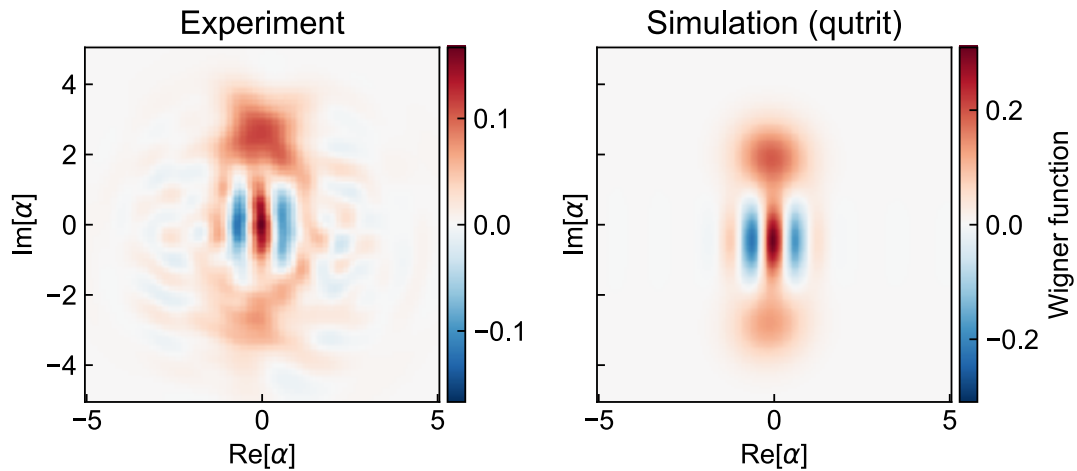
Figure 7.12: Results of the cat state generation (left) and simulation (right) with experimental parameters. For the experiment, the pulse amplitudes for the displacement operations are A_d =(0, 0.15, 0.5), and the state is estimated from a total of 18 traces with six different phase sweeps, (0, 1/3, 2/3, 3/3, 4/3, 5/3) × π, for each amplitude. For the simulation, one hundred Fock levels are assumed for the resonator and three for the auxiliary cubic transmon.
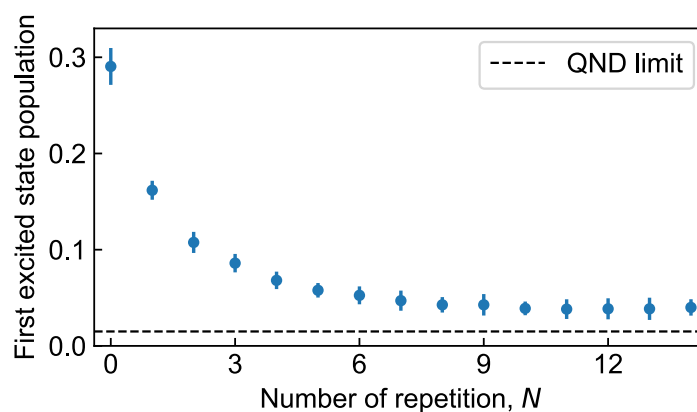
Figure 7.13: Relation between the number of modular measurement repetitions, N, and the auxiliary qubit first excited state population. The dashed line indicates the limit determined from the QND and the assignment readout fidelity, $1 - F_a \times F_{QND} \approx 0.015$.
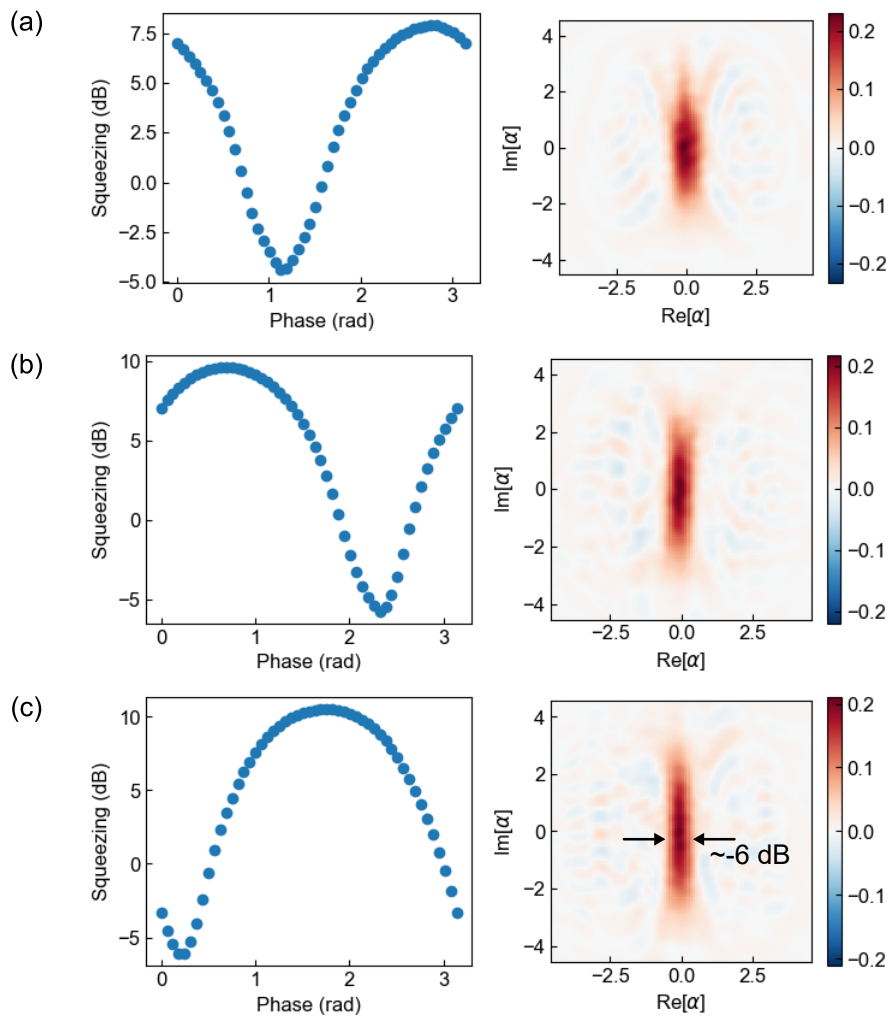
Figure 7.14: Fock basis tomography results for repetitions, (a) $N = 4$, (b) $N = 7$, (c) $N = 10$. For panels (a)–(c), the left panel shows the squeezing level obtained by fitting with a Gaussian function by projecting the axes while rotating them around the origin.

Chapter 8

Conclusion and prospects

8.1 High-quality transmon qubits

We have successfully fabricated state-of-the-art quality transmon qubits using TiN thin films grown at high temperatures on silicon substrates. This positive outcome is believed to result from the favorable characteristics of the interface between silicon and TiN thin film, which is due to the domain-matched epitaxial growth of TiN thin film. The interface between the air and TiN thin film is of good quality because the TiN thin film does not easily re-oxidize in air. However, despite our attempts to optimize the design for better performance, we were unable to obtain any results that could guide us in improving the design. One of the possible reasons for this is that the electromagnetic shielding of the sample holder is not sufficient the energy loss due to radiation to the continuum field is not negligible, and the loss around the Josephson junction may have been dominant.

To solve these problems and improve further, we will continue the electromagnetic field analysis of the sample holder and attempt to optimize the design. In addition, it would be effective to investigate the frequency dependence of the energy relaxation time using frequency-tunable transmons to identify the problems with the current sample holder.

8.2 Coupler-assisted SWAP interaction

We have investigated and analytically modeled the four-wave-mixing interaction among three superconducting qubits under a microwave drive. Using the interaction, we demonstrated the coupler-assisted-swap-based control-Z gate between two fixed-frequency transmons mediated by a fixed-frequency transmon coupler. The drive efficiency of the gate has a practical value in a wide parameter range, providing an alternative solution to the frequency crowding problem and a new design paradigm for superconducting quantum processors. Moreover, a physically efficient parity measurement could be realized by measuring the coupler after a pulse sequence of simultaneous π-pulses to the blue and red CAS transitions. An alternative pulse sequence of two π-pulses to the blue (red) CAS transition sandwiching π-pulses to the data qubits would also work.

In the future, we plan to conduct a more detailed analysis of design parameters to better understand the correlation between designable parameters, frequency collision, and gate fidelity. We will leverage this understanding to develop an architecture accommodating more physical qubits. In addition, although we did not consider actively measuring couplers in this thesis, we would like to consider the implementation of error-correcting codes that actively use parity measurements that can be realized by measuring couplers.

8.3   Spin-dependent force in a circuit-QED system

We have realized the spin-dependent force using the three-wave mixing interaction provided by SNAIL with the planar superconducting circuit. We also found that decoupling the dispersive interaction by adding the carrier drive is important for this realization in the circuit-QED system. In addition, we prepared cat and squeezed vacuum states using this spin-dependent force and demonstrated state tomography.

While we have shown that it is possible to control the resonator state without relying on the dispersive interaction, the performance of the auxiliary qubit is not as good as that of the system using the dispersive interaction due to the frequency tunability. It is necessary to redesign the system to separate the three-wave mixing interaction from the qubit and use it independently from the auxiliary qubit in the future.

List of publications

S. Shirai, Y. Okubo, K. Matsuura, A. Osada, Y. Nakamura, and A. Noguchi, "All-microwave manipulation of superconducting qubits with a fixed-frequency transmon coupler", Phys. Rev. Lett. **130**, 260601 (2023).

Appendix A

Unitary transformations

A.1 Baker-Campbell-Hausdorff formula

We first introduce a useful formula known as the Baker-Campbell-Hausdorff (BCH) formula, which holds for any two operators $\hat{S}$ and $\hat{H}$

$$e^{\hat{S}}\hat{H}e^{-\hat{S}} = \hat{H} + [\hat{S}, \hat{H}] + \frac{1}{2!}[\hat{S}, [\hat{S}, \hat{H}]] + \cdots$$

$$= \sum_{n=0}^{\infty} \frac{1}{n!}\mathcal{C}_{\hat{S}}^n[\hat{H}], \tag{A.1}$$

where

$$\mathcal{C}_{\hat{S}}^0[\hat{H}] = \hat{H},$$
$$\mathcal{C}_{\hat{S}}^1[\hat{H}] = [\hat{S}, \hat{H}],$$
$$\mathcal{C}_{\hat{S}}^2[\hat{H}] = [\hat{S}, [\hat{S}, \hat{H}]],$$
$$\mathcal{C}_{\hat{S}}^3[\hat{H}] = [\hat{S}, [\hat{S}, [\hat{S}, \hat{H}]]],$$
$$\ldots,$$
$$\mathcal{C}_{\hat{S}}^n[\hat{H}] = [\underbrace{\hat{S}, [\hat{S}, [\hat{S}, \ldots,}_{n \text{ times}} \hat{H}]]]. \tag{A.2}$$

A.2 Frame change

Here, we introduce a method for converting a Hamiltonian defined in one frame to a representation in another expressed by a unitary operator. As a starting point, we consider the Schrödinger equation

$$i\hbar\frac{d}{dt}|\psi(t)\rangle = \hat{H}|\psi(t)\rangle. \tag{A.3}$$

Then, using the unitary operator $\hat{R}(t)$, we transform the state $|\psi(t)\rangle$ as follows

$$|\psi'(t)\rangle = \hat{R}(t)|\psi(t)\rangle. \tag{A.4}$$

When we act $\hat{R}^\dagger(t)$ on the equation from the left and substitute into the Schrödinger equation, we obtain the following equation:

$$i\frac{d}{dt}|\psi'\rangle = \left(\hat{R}\hat{H}\hat{R}^\dagger - i\hat{R}\frac{d}{dt}\hat{R}^\dagger\right)|\psi'\rangle, \tag{A.5}$$

where the time dependencies of operators and states are omitted. Thus, we obtain a new Hamiltonian in the frame defined by $\hat{R}$ as follows

$$\hat{R}\hat{H}\hat{R}^{\dagger} - i\hat{R}\frac{d}{dt}\hat{R}^{\dagger} \equiv \hat{H}'. \tag{A.6}$$

When $\hat{R}$ is independent of time, the second term on the left-hand side becomes zero, and this Hamiltonian satisfies the Schrödinger equation.

A.3   Rotatig frame transformation

Here, we introduce the rotating frame transformation, one of the most commonly used frame transformations, using the harmonic oscillator Hamiltonian $\hat{H}_c = \omega_c \hat{a}^{\dagger}\hat{a}$ as an example. With the frame transformation operator $\hat{R} = e^{i\omega t \hat{a}^{\dagger}\hat{a}}$, the annihilation operator $\hat{a}$ is transformed as follows using the BCH formula (A.1)

$$\begin{aligned}
\hat{R}\hat{a}\hat{R}^{\dagger} &= \hat{a} + i\omega t[\hat{a}^{\dagger}\hat{a}, \hat{a}] + \frac{(i\omega t)^2}{2!}[\hat{a}^{\dagger}\hat{a}, [\hat{a}^{\dagger}\hat{a}, \hat{a}]] + \dots, \\
&= a + i\omega t(-1)\hat{a} + \frac{(i\omega t)^2}{2!}(-1)^2\hat{a} + \dots, \\
&= a\sum_{n=0}^{\infty}\frac{(-i\omega t)^n}{n!} = \hat{a}e^{-i\omega t},
\end{aligned} \tag{A.7}$$

where $[\hat{a}^{\dagger}\hat{a}, \hat{a}] = -\hat{a}$ is used. Following the same procedure, we obtain $\hat{R}\hat{a}^{\dagger}\hat{R}^{\dagger} = \hat{a}^{\dagger}e^{i\omega t}$. With these results and Eq. (A.6), the Hamiltonian of the harmonic oscillator is transformed as follows

$$\hat{R}\hat{H}_c\hat{R}^{\dagger} = \omega_c\hat{R}\hat{a}^{\dagger}\hat{R}^{\dagger}\hat{R}\hat{a}\hat{R}^{\dagger} - i\hat{R}\frac{d}{dt}\hat{R}^{\dagger} \tag{A.8}$$

$$= (\omega_c - \omega)\hat{a}^{\dagger}\hat{a} \equiv \hat{H}'_c, \tag{A.9}$$

where $\hbar = 1$ is assumed and $\hat{R}^{\dagger}\hat{R} = \hat{I}$ is used. If $\omega_c = \omega$, the transformed Hamiltonian $\hat{H}'_c$ is zero, and time evolution seems to stop in this frame. This helps simplify the analysis in many situations.

A.4   Displacement transformation

This section describes the displacement transformation. This transformation can remove coherent (linear) drive terms from a driven Hamiltonian. The displacement operator is defined as

$$\hat{D}(\alpha) = e^{\alpha\hat{a}^{\dagger} - \alpha^*\hat{a}}, \tag{A.10}$$

where α is a complex value. Using $[\alpha^*\hat{a} - \alpha\hat{a}^{\dagger}, \hat{a}] = \alpha$ and BCH formula (A.1), we obtain the unitary transformations as follows

$$\hat{D}^{\dagger}\hat{a}\hat{D} = \hat{a} + \alpha, \tag{A.11}$$

$$\hat{D}^{\dagger}\hat{a}^{\dagger}\hat{D} = \hat{a}^{\dagger} + \alpha^*. \tag{A.12}$$

A.5 Schrieffer-Wolff transformation

This section summarizes the Schrieffer-Wolff transformation, an essential theoretical tool for analyzing circuit-QED systems, based on the literature [100, 101]. We consider the following Hamiltonian with order parameter λ

$$\hat{H} = \hat{H}_0 + \lambda\hat{V}. \tag{A.13}$$

Here, $\hat{H}_0$ and $\hat{V}$ are an unperturbed exactly solvable Hamiltonian and a perturbative term, respectively. Then, we choice the ansatz of $\hat{S}$ in $\hat{U} = e^{-i\hat{S}}$ as follows

$$\hat{S} = \lambda\hat{S}_1 + \lambda^2\hat{S}_2 + \lambda^3\hat{S}_3 + \cdots, \tag{A.14}$$

where $\hat{S}_i$ must be a Hermitian operator. Substituting Eqs. (A.13) and (A.14) into the BCH formula (A.1), we obtain the equation as follows

$$\begin{aligned}
e^{\hat{S}}(\hat{H}_0 + \lambda\hat{V})e^{-\hat{S}} = \hat{H}_0 \\
+ \lambda^1\left(i[\hat{S}_1, \hat{H}_0] + \hat{V}\right) \\
+ \lambda^2\left(i[\hat{S}_2, \hat{H}_0] - \frac{1}{2}[\hat{S}_1, [\hat{S}_1, \hat{H}_0]] + i[\hat{S}_1, \hat{V}]\right) \\
+ \lambda^3\left(i[\hat{S}_3, \hat{H}_0] - \frac{i}{6}[\hat{S}_1, [\hat{S}_1, [\hat{S}_1, \hat{H}_0]]]\right. \\
\left. -\frac{1}{2}\left([\hat{S}_1, [\hat{S}_2, \hat{H}_0]] + [\hat{S}_2, [\hat{S}_1, \hat{H}_0]]\right) + i[\hat{S}_2, \hat{V}] - \frac{1}{2}[\hat{S}_1, [\hat{S}_1, \hat{V}]]\right) \\
+ \mathcal{O}(\lambda^4).
\end{aligned} \tag{A.15}$$

To simplify this equation, we use the following notations

$$e^{\hat{S}}(\hat{H}_0 + \lambda\hat{V})e^{-\hat{S}} = \sum_{m=0}^{\infty} \hat{H}^{(m)}, \tag{A.16}$$

$$\hat{H}^{(m)} = i[\hat{S}_m, \hat{H}_0] + \hat{H}_x^{(m)}, \tag{A.17}$$

$$\hat{H}_x^{(m)} = -i[\hat{S}_m, \hat{H}_0] + \sum_{\boldsymbol{l}\in G_m} \mathcal{C}_{\mathrm{S_{arr}}}^{\mathrm{len}(\boldsymbol{l})}[\hat{H}_0] + \sum_{\boldsymbol{l}\in G_{m-1}} \mathcal{C}_{\mathrm{S_{arr}}}^{\mathrm{len}(\boldsymbol{l})}[\hat{V}], \tag{A.18}$$

where $\boldsymbol{l}$ is a permutation of n elements chosen from $\{1, 2, \ldots, m\}$ with repetition, and G_m is a subset of $\{\boldsymbol{l}\}_m$ whose elements sum to m. In other words, $m = \sum_{i\in\boldsymbol{l}} i$ for all $\boldsymbol{l} \in G_m$. Additionally, if $\boldsymbol{l} = (j_1, j_2, \ldots)$, then $\mathrm{S_{arr}} = (\hat{S}_{j_1}, \hat{S}_{j_2}, \ldots)$. With these definitions, $\mathcal{C}_{\mathrm{S_{arr}}}^{\mathrm{len}(\boldsymbol{l})}[A]$ can be computed as follows

$$\mathcal{C}_{\mathrm{S_{arr}}}^{\mathrm{len}(\boldsymbol{l})}[A] = \frac{i^{\mathrm{len}(\boldsymbol{l})}}{\mathrm{len}(\boldsymbol{l})!}\underbrace{[\hat{S}_{j_1}, [\hat{S}_{j_2}, [\hat{S}_{j_3}, \ldots, A]]]}_{\mathrm{len}(\boldsymbol{l})\ \mathrm{times}}, \ \boldsymbol{l} = (j_1, j_2, j_3, \ldots). \tag{A.19}$$

At each order m, $\hat{H}_x^{(m)}$ is a function of only $(\hat{S}_1, \hat{S}_2, \ldots, \hat{S}_{m-1})$, one can be computed since we assume lower order $(\hat{S}_1, \hat{S}_2, \ldots, \hat{S}_{m-1})$ are known. Now, since our goal is to obtain a block-diagonal term $\hat{H}^{(m)}$ for each order, we assume the following form

$$\hat{H}^{(m)} = \hat{H}_1^{(m)} \oplus \hat{H}_2^{(m)} \oplus \cdots \oplus \hat{H}_\mu^{(m)} \oplus \cdots, \tag{A.20}$$

where μ is the index of the subspace to be block-diagonalized. $\hat{H}_\mu^{(m)}$ can be written using the projection operator on a subspace μ as follows

$$\hat{H}_\mu^{(m)} = \hat{P}_\mu \hat{H}^{(m)} \hat{P}_\mu. \tag{A.21}$$

Similarly, using these projection operators $\hat{P}_\mu$ and $\hat{P}_\nu$, we introduce the following equations

$$\hat{S}_m^{\mu,\nu} = \hat{P}_\mu \hat{S}_m \hat{P}_\mu, \tag{A.22}$$

$$\hat{H}_{x_{\mu,\nu}}^{(m)} = \hat{P}_\mu \hat{H}_x^{(m)} \hat{P}_\mu. \tag{A.23}$$

Using these equations, we can systematically compute $\hat{S}_m^{\mu,\nu}$ at each order m as follows

$$\hat{S}_m^{\mu,\nu} = \mathrm{mat}\left(\left(\hat{H}_\mu^{(0)} \otimes \hat{I}_\nu - \hat{I}_\mu \otimes \hat{H}_\nu^{(0)T}\right)^{-1} \times \mathrm{vec}\left(-i\hat{H}_{x_{\mu,\nu}}^{(m)}\right)\right), \tag{A.24}$$

where $\mathrm{vec}(|a\rangle\langle b|) = |a\rangle \otimes |b\rangle$.

Appendix B

Model of external drive

Typically, quantum systems require external access for control, such as CPW, optical fiber, or similar tools. In this specific case, we assume that the control line is a one-dimensional waveguide that is coupled to the harmonic oscillator at the position of $r = 0$, and the Hamiltonian models this system is following [102]

$$
\hat{H}/\hbar = \underbrace{\omega_c \hat{a}^\dagger \hat{a}}_{\text{Harmonic oscillator}} + \underbrace{\int_{-\infty}^{\infty} d\omega \, \omega \hat{b}_\omega^\dagger \hat{b}_\omega}_{\text{1-D waveguide}} + \underbrace{\sqrt{\frac{\kappa_e}{2\pi}} \int_{-\infty}^{\infty} d\omega \left(\hat{a}^\dagger \hat{b}_\omega + \hat{a} \hat{b}_\omega^\dagger \right)}_{\text{Interaction}}, \tag{B.1}
$$

where ω is the continuous angular frequency of a photon mode with the energy $E_k = \hbar\omega_k$ in the waveguide, and $\hat{b}_\omega$ satisfies $[\hat{b}_\omega, \hat{b}_{\omega'}^\dagger] = \delta(\omega - \omega')$. Thus, $\hat{b}_\omega$ has the unit of $1/\sqrt{2\pi \cdot \text{Hz}}$. In addition, we assumed that the harmonic oscillator and waveguide interaction is weak and can be modeled by the Markov process [12, 102]. Then, we move on to the rotating frame with the second term of Eq. (B.1) as follows

$$
\hat{H}_r/\hbar = \omega_c \hat{a}^\dagger \hat{a} + \sqrt{\frac{\kappa_e}{2\pi}} \int_{-\infty}^{\infty} d\omega \left(\hat{a}^\dagger \hat{b}_\omega e^{-i\omega t} + \hat{a} \hat{b}_\omega^\dagger e^{i\omega t} \right). \tag{B.2}
$$

Now assume that the one-dimensional waveguide is excited to the coherent state with an amplitude β_ω and is in an initial state that can be written as a product state $\rho_c \otimes |\beta_\omega\rangle\langle\beta_\omega|$. Therefore, we consider the above Hamiltoani in the displaced frame using the displacement operator $\hat{D}(-\beta_\omega) = \exp(-\beta_\omega \hat{b}_\omega^\dagger + \beta_\omega^* \hat{b}_\omega)$, and obtain the transformed Hamiltonian as follows

$$
\begin{aligned}
\hat{H}_r'/\hbar = {}& \omega_c \hat{a}^\dagger \hat{a} + \sqrt{\frac{\kappa_e}{2\pi}} \int_{-\infty}^{\infty} d\omega \left(\hat{a}^\dagger \hat{b}_\omega e^{-i\omega t} + \hat{a} \hat{b}_\omega^\dagger e^{i\omega t} \right) \\
& - \sqrt{\frac{\kappa_e}{2\pi}} \int_{-\infty}^{\infty} d\omega \left(\hat{a}^\dagger \beta_\omega e^{-i\omega t} + \hat{a} \beta_\omega^* e^{i\omega t} \right).
\end{aligned} \tag{B.3}
$$

For simplicity, we assume that the waveguide is excited with a single frequency tone, ω_d. Thus, the coherent amplitude β_ω can be written as $\beta\delta(\omega - \omega_d)$, and we obtain the following equation

$$
\begin{aligned}
\hat{H}_r'/\hbar = {}& \omega_c \hat{a}^\dagger \hat{a} + \sqrt{\frac{\kappa_e}{2\pi}} \int_{-\infty}^{\infty} d\omega \left(\hat{a}^\dagger \hat{b}_\omega e^{-i\omega t} + \hat{a} \hat{b}_\omega^\dagger e^{i\omega t} \right) \\
& - \sqrt{\frac{\kappa_e}{2\pi}} \left(\hat{a}^\dagger \beta e^{-i\omega_d t} + \hat{a} \beta^* e^{i\omega_d t} \right).
\end{aligned} \tag{B.4}
$$

Since the unit of β_ω should be $\sqrt{2\pi \cdot \mathrm{Hz}}$ as well as $\hat{b}_\omega$, the number of photons present in the waveguide per unit time is $|\beta|^2/2\pi = P_d/\hbar\omega_d$, where P_d is the input drive power. Using this relation, we can rewrite Eq. (B.4) as follows

$$
\hat{H}'_r/\hbar = \omega_c \hat{a}^\dagger \hat{a} + \sqrt{\frac{\kappa_e}{2\pi}} \int_{-\infty}^{\infty} d\omega \left(\hat{a}^\dagger \hat{b}_\omega e^{-i\omega t} + \hat{a} \hat{b}_\omega^\dagger e^{i\omega t} \right)
$$
$$
- \sqrt{\frac{\kappa_e P_d}{\hbar\omega_d}} \left(\hat{a}^\dagger e^{-i\omega_d t} + \hat{a} e^{i\omega_d t} \right). \tag{B.5}
$$

Finally, assuming the strong drive power and small external coupling limit, we obtain the following effective drive Hamiltonian

$$
\hat{H}_{\mathrm{eff}}/\hbar = \omega_c \hat{a}^\dagger \hat{a} - \frac{\Omega}{2} \left(\hat{a}^\dagger e^{-i\omega_d t} + \hat{a} e^{i\omega_d t} \right), \tag{B.6}
$$

where $\Omega = 2\sqrt{\frac{\kappa_e P_d}{\hbar\omega_d}}$.

Appendix C

Supplemental material for "Coupler-assisted SWAP interaction"

C.1 Derivation of equations

As described in the main text, the system and drive Hamiltonians we consider are

$$\hat{H} = \hat{H}_0 + \hat{H}_c \tag{C.1}$$

$$\hat{H}_0/\hbar = \sum_i \left(\omega_i \hat{a}_i^\dagger \hat{a}_i + \frac{\alpha_i}{2} \hat{a}_i^\dagger \hat{a}_i^\dagger \hat{a}_i \hat{a}_i \right), \tag{C.2}$$

$$\hat{H}_c/\hbar = \sum_{i \neq c} g_{ic}(\hat{a}_i^\dagger \hat{a}_c + \hat{a}_i \hat{a}_c^\dagger), \tag{C.3}$$

$$\hat{H}_d/\hbar = \Omega_d \cos \omega_d t \left(\hat{a}_c^\dagger + \hat{a}_c \right), \tag{C.4}$$

where $i \in \{1, 2, c\}$. By following the procedure of Schrieffer-Wolff transformation [103], we obtain an anti-Hermitian operator $\hat{S} = \hat{S}_1 + \hat{S}_2$ from the solutions of the following equations,

$$[\hat{H}_0, \hat{S}_1] + \hat{O}_1 = 0, \tag{C.5}$$

$$[\hat{H}_0, \hat{S}_2] + \hat{O}_2 = 0. \tag{C.6}$$

Here, $\hat{O}_1 = \hat{H}_c$ is considered as an off-diagonal perturbation term. We also define the diagonal and off-diagonal terms of $\frac{1}{2}\left[\hat{O}_1, \hat{S}_1\right]$ as $\hat{D}_2$ and $\hat{O}_2$, respectively. To derive the explicit forms of $\hat{S}_1$ and $\hat{S}_2$, we assume that each transmon is a four-level system and algebraically solve Eqs. (C.5) and (C.6) with a Python program. Under this setup, we first derive the CAS transition frequencies in the weak drive amplitude limit. Upon the transformation, the anti-Hermitian operators $\hat{S}_1$ and $\hat{S}_2$ cancel the off-diagonal terms in $\hat{H}$, and we obtain a diagonalized Hamiltonian valid up to the second order of g_{ic},

$$\hat{H}' = \hat{H}_0 + \hat{D}_2. \tag{C.7}$$

With this equation, we derive the analytical expressions of the CAS transition frequencies in the weak drive amplitude limit,

$$
\begin{aligned}
\omega_b' &= \langle 101|\hat{H}'|101\rangle/\hbar - \langle 010|\hat{H}'|010\rangle/\hbar, \\
&= \omega_c + \Delta_{12} + \frac{2g_{1c}^2(\alpha_1 + \alpha_c)}{(\Delta_{1c} - \alpha_c)(\Delta_{1c} + \alpha_1)} - \frac{2g_{2c}^2}{\Delta_{2c}},
\end{aligned} \tag{C.8}
$$

$$
\begin{aligned}
\omega_r' &= \langle 011|\hat{H}'|011\rangle/\hbar - \langle 100|\hat{H}'|100\rangle/\hbar, \\
&= \omega_c - \Delta_{12} + \frac{2g_{2c}^2(\alpha_2 + \alpha_c)}{(\Delta_{2c} - \alpha_c)(\Delta_{2c} + \alpha_2)} - \frac{2g_{1c}^2}{\Delta_{1c}}.
\end{aligned} \tag{C.9}
$$

Next, we derive the effective CAS oscillation frequencies. We move to the reference frame rotating at ω_d and transform the drive Hamiltonian Eq. (C.4) into

$$
\hat{H}_d^r/\hbar \approx \frac{1}{2}\Omega\big(\hat{a}_c^\dagger + \hat{a}_c\big), \tag{C.10}
$$

where we use the rotating-wave approximation. Note that, the form of $\hat{S}$ is the same in the rotating frame. Using the obtained $\hat{S}$ and the Baker-Campbell-Hausdorff formula, we expand the drive Hamiltonian Eq. (C.10) as

$$
\begin{aligned}
e^{\hat{S}}\hat{H}_d^r e^{-\hat{S}} &= \hat{H}_d^r + \left[\hat{S}, \hat{H}_d^r\right] + \frac{1}{2!}\left[\hat{S}, \left[\hat{S}, \hat{H}_d^r\right]\right] + \cdots, \\
&\approx \hat{H}_d^r + \left[\hat{S}_1 + \hat{S}_2, \hat{H}_d^r\right] + \frac{1}{2!}\left[\hat{S}_1, \left[\hat{S}_1, \hat{H}_d^r\right]\right] \equiv \hat{H}_d'^r.
\end{aligned} \tag{C.11}
$$

In the last line of the formula, we keep only the terms up to the second order of g_{ic} by assuming $|g_{ic}/\Delta_{ic}| \ll 1$. Finally, we reach the expressions of the effective CAS oscillation frequencies presented in the main text:

$$
\begin{aligned}
\Omega_b &\approx 2\langle 010|\hat{H}_d'^r|101\rangle/\hbar \\
&= \frac{2g_{1c}g_{2c}\alpha_c\Omega_d}{\Delta_{12}(\delta_c - \delta_1 + \alpha_c)(\delta_c - \delta_2)}, \\
&= \frac{2g_{1c}g_{2c}\alpha_c\Omega_d}{\Delta_{12}(\omega_c - \omega_1 + \alpha_c)(\omega_c - \omega_2)},
\end{aligned} \tag{C.12}
$$

$$
\begin{aligned}
\Omega_r &\approx 2\langle 100|\hat{H}_d'^r|011\rangle/\hbar \\
&= \frac{-2g_{1c}g_{2c}\alpha_c\Omega_d}{\Delta_{12}(\delta_c - \delta_2 + \alpha_c)(\delta_c - \delta_1)}, \\
&= \frac{-2g_{1c}g_{2c}\alpha_c\Omega_d}{\Delta_{12}(\omega_c - \omega_2 + \alpha_c)(\omega_c - \omega_1)},
\end{aligned} \tag{C.13}
$$

where $\delta_i = \omega_i - \omega_d$, $(i \in \{1, 2, c\})$. Moreover, we derive an analytical expression of the ac-field-dependent ZZ coupling induced by the ac Stark shift. For concreteness, we consider the case where the drive frequency ω_d is off-resonant but close to ω_b. As a first step, we expand the drive Hamiltonian using $\hat{S}$ and then move to the reference frame rotating at ω_b, which is determined by the drive power Ω_d. Applying the rotating-wave approximation and dropping fast oscillating terms, we get the following time-dependent effective drive Hamiltonian

$$
\hat{H}_d^r(t)/\hbar \approx \frac{\Omega_b}{2}\big(|101\rangle\langle 010|e^{-i\delta t} + |010\rangle\langle 101|e^{i\delta t}\big), \tag{C.14}
$$

where $\delta = \omega_d - \omega_b$. For further analysis, we assume a form of system Hamiltonian

$$
\hat{H}_{\text{sys}} = \hat{H}^{(0)} + \hat{H}(t), \tag{C.15}
$$

where $\hat{H}^{(0)}$ is the time-independent part and $\hat{H}(t)$ is the time-periodic part. When $\hat{H}(t)$ has the characteristic frequency ω, it can be expanded in a Fourier series of the form

$$\hat{H}(t) = \sum_{n \neq 0} \hat{H}_n e^{in\omega t}. \tag{C.16}$$

We now apply the van Vleck transformation [104] and obtain the time-averaged Hamiltonian to first order

$$\hat{H}'_{\text{sys}} \approx \hat{H}^{(0)} - \frac{1}{2} \sum_{n \neq 0} \frac{\left[\hat{H}_{-n}, \hat{H}_n\right]}{n\hbar\omega}. \tag{C.17}$$

Comparing Eqs. (C.14) and the last terms of (C.17), we obtain an expression of the ac-field-tunable part of the ZZ coupling,

$$\xi_{\text{ac}} = -\frac{\Omega_b^2}{8\delta}, \tag{C.18}$$

where we assume that the coupler is in the ground state. With this term, the entire ZZ interaction under the off-resonant microwave drive can be expressed as

$$\xi_{\text{ZZ}}(\omega_d, \Omega_d) = \xi_0 - \frac{\Omega_b^2}{8(\omega_d - \omega_b)}, \tag{C.19}$$

where $\xi_0 = \frac{2g_{\text{eff}}^2(\alpha_1+\alpha_2)}{(\Delta_{12}+\alpha_1)(\alpha_2-\Delta_{12})}$ is the static residual ZZ coupling that is valid up to the second order of the effective transverse coupling, $g_{\text{eff}} = \frac{g_{1c}g_{2c}}{2}\left(\frac{1}{\Delta_{1c}} + \frac{1}{\Delta_{2c}}\right) + g_{12}$, between the data qubits.

C.2 Numerical simulation method

As mentioned in the main text, we consider up to the third excited state of each transmon for numerical calculations. To evaluate the CAS oscillation frequency, we numerically diagonalize the Hamiltonian represented in the reference frame rotating at ω_d,

$$\hat{H}_r = \hat{H}_0^r + \hat{H}_c^r + \hat{H}_d^r, \tag{C.20}$$

$$\hat{H}_0^r/\hbar = \sum_i \left(\delta_i \hat{a}_i^\dagger \hat{a}_i + \frac{\alpha_i}{2} \hat{a}_i^\dagger \hat{a}_i^\dagger \hat{a}_i \hat{a}_i\right), \tag{C.21}$$

$$\hat{H}_c^r/\hbar = \sum_{i \neq c} g_{ic}(\hat{a}_i^\dagger \hat{a}_c + \hat{a}_i \hat{a}_c^\dagger) + g_{12}(\hat{a}_1^\dagger \hat{a}_2 + \hat{a}_1 \hat{a}_2^\dagger), \tag{C.22}$$

$$\hat{H}_d^r/\hbar \approx \frac{1}{2}\Omega_d(\hat{a}_c^\dagger + \hat{a}_c). \tag{C.23}$$

Here we take into account the direct coupling g_{12} between the data transmons. For each drive amplitude Ω_d, we sweep the drive frequency ω_d and obtain the resonant CAS oscillation frequencies Ω_b (Ω_r) as the splitting at the anticrossing between the states $|010\rangle$ and $|101\rangle$ ($|100\rangle$ and $|011\rangle$).

Next, we estimate the coherence limit of the average fidelity of the CAS-based CZ gate. We use Eq. (C.20) as the starting point and numerically simulate the JAZZ sequence in Fig. 3(a) in the main text. For the measurement angle 0 in the JAZZ sequence, the population of the state $|110\rangle$ ideally becomes unity at the end of the controlled phase is

π. We thus numerically maximize the $|110\rangle$ population by iteratively solving the time-dependent Schrödinger equation taking account of the flat-top Gaussian pulse shape and obtaining an optimal parameter set of the drive frequency and amplitude. Note that we assume perfect accuracy of the state preparation, measurement, π-pulse, and $\pi/2$-pulse. Using the result, we solve the master equation taking into account the coherence times shown in Table C.1 and reconstruct a noisy quantum channel $\mathcal{E}'_{\mathrm{CZ}}$, which is locally equivalent to a CZ gate, for the entire system. We thus apply local phase rotations to the data qubits with perfect accuracy and obtain the noisy CAS-based CZ gate channel $\mathcal{E}_{\mathrm{CZ}}$. Finally, we express the average gate fidelity of a quantum channel $\mathcal{E}$ using the following equation [105]

$$\bar{F}(\mathcal{E}) = \frac{\mathrm{Tr}[(P_1 \otimes P_1)\mathcal{S}_\mathcal{E}] + \mathrm{Tr}[P_1 \mathcal{E}(P_1)]}{d(d+1)}, \tag{C.24}$$

where P_1 is a projector onto the d-dimensional computational subspace and $\mathcal{S}_\mathcal{E}$ is the superoperator form of the quantum channel $\mathcal{E}$. Using Eq. (C.24), we evaluate the average gate fidelity of $\mathcal{E}_{\mathrm{CZ}}$ considering a composition between two channels $\tilde{\mathcal{E}} = \mathcal{U}_{\mathrm{CZ}} \circ \mathcal{E}_{\mathrm{CZ}}$, where $\mathcal{U}_{\mathrm{CZ}}$ is the ideal CAS-based CZ gate channel. The value obtained is $\bar{F}(\tilde{\varepsilon}) \approx 0.978$.

Table C.1: Coherence times of the qubits.

	T_1 (μs)	T_2^* (μs)	T_2^e (μs)
Data transmon, Q$_1$	95 ± 10	76 ± 10	88 ± 3
Data transmon, Q$_2$	108 ± 6	81 ± 8	166 ± 9
Coupler transmon, Q$_c$	15 ± 1	15 ± 2	18 ± 2

C.3 Supplemental experiments

C.3.1 ac-field tunable ZZ interaction and estimation of the direct coupling

We estimate the direct transverse coupling strength and the residual ZZ interaction strength using the JAZZ experiment described in the main text. Figure C.1(a) shows a pulse sequence, where we constantly apply a relatively weak coupler drive $\Omega_d/2\pi \approx 7.3$ MHz, while sweeping the delay time τ between the echo pulses and the coupler drive detuning from the blue CAS transition, $\delta = \omega_d - \omega_b$. Furthermore, to know the sign as well as the magnitude of the ZZ interaction, the measurement angle ϕ is swept together with τ according to the relation $\phi/\tau = 2\pi \times 100\,\mathrm{kHz}$ as shown in Fig. C.1(b) as an example. Figure C.1(c) shows the measured ZZ interaction strength ξ_{ZZ} depending on the coupler drive detuning. By fitting this modulation with numerically calculated values of the residual ZZ interaction diagonalizing Eq. (C.20), we obtain the direct transverse coupling strength of $g_{12}/2\pi \simeq 1.9\,\mathrm{MHz}$. The bare residual ZZ interaction strength is also estimated to be $\xi_0/2\pi \simeq -1.5\,\mathrm{kHz}$, where all other parameters we use are presented in the main text and g_{12} is the only free parameter.

C.3.2 ac Stark shift of the CAS transitions

In Figs. C.2(a) and (b), we show the experimental results of the ac-Stark-shifted blue and red CAS transition frequencies as a function of the coupler drive amplitude. The CAS transition frequencies are determined by fitting the chevron pattern at each point. We
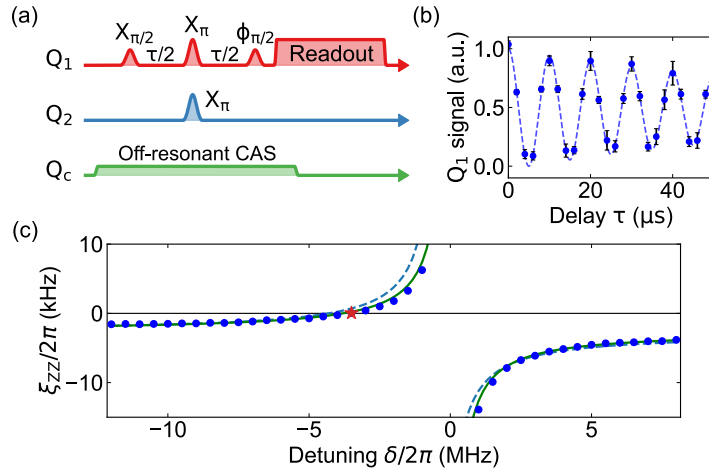
Figure C.1: (a) Pulse sequence for measuring the tunable ZZ interaction strength using the JAZZ protocol. (b) Example of the experimental data obtained with the JAZZ protocol. The data was taken at the red star shown in (c). The dashed line is the fitting curve to an exponentially decaying sinusoidal function. (c) Dependence of the ZZ interaction strength on the drive detuning from the blue CAS transition with a fixed drive power $\Omega_d/2\pi = 7.3$ MHz. The static ZZ interaction is canceled at the condition indicated by the red star. The green solid line shows the fitting result using Eq. (C.19), and the blue dashed line is the numerical fit using the direct coupling g_{12} as the only free parameter.

model the frequency shift with the ac Stark shift of the coupler transmon $\Delta_c^{\mathrm{ac}} = \frac{\alpha_c \Omega_d^2}{2\delta_c(\delta_c+\alpha_c)}$ [106, 107]. Using Eqs. (C.8) and (C.9), we define the analytically evaluated ac-Stark-shifted CAS transition frequencies as

$$\tilde{\omega}_b = \omega_b' + \Delta_c^{\mathrm{ac}}, \tag{C.25}$$

$$\tilde{\omega}_r = \omega_r' + \Delta_c^{\mathrm{ac}}, \tag{C.26}$$

where we ignore the ac Stark shifts of the data transmons, which are negligible compared to Δ_c^{ac}. In Figs. C.2(a) and (b), we see semiquantitative agreement in the weak drive limit. The deviations between the numerical and experimental results at larger drive amplitudes could be explained by the higher-order nonlinear terms dropped in the Duffing-oscillator model [57, 108].

C.3.3 Rabi oscillations in the blue CAS subspace

We measure the associated oscillations of the population of each qubit involved in the blue CAS transition. The pulse sequence used is identical to the one in Fig. 2(a) in the main text except for the qubits to be read out. As predicted by the theoretical model, we observe signals corresponding to the Rabi oscillations between the states $|010\rangle$ and $|101\rangle$.

C.4 Comparison with the CR gate

Lastly, we compare the expected properties of the blue CAS-based CZ gate with those of the CR gate, which is most commonly used in architectures with fixed-frequency transmons. The results are shown in Fig. C.4. In both cases, we see the decrease of the residual ZZ interaction by introducing g_{12} in the regions with large enough g_{ic}/Δ_{ic} for a high drive
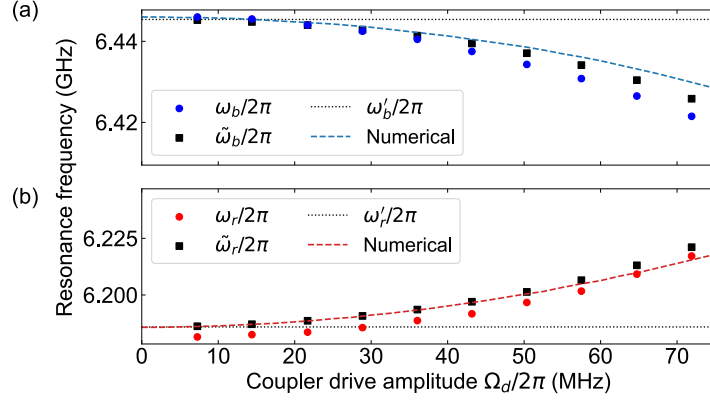
Figure C.2: Resonance frequencies of the (a) blue and (b) red CAS transitions. The filled circles are the experimental results obtained from the fitting of the chevron patterns for each drive amplitude. The filled squares are analytically calculated ac-Srark-shifted CAS transition frequencies [Eqs. (C.25) and (C.26)] using the same parameters as in the experiment. The dotted lines are the analytically evaluated CAS transition frequencies in the limit of the weak drive [Eqs. (C.8) and (C.9)]. The dashed lines are obtained numerically by diagonalizing Eqs. (C.20)–(C.23).

efficiency. However, the CR gate only achieves sufficient drive efficiency η_{CR} in the regime where ξ_{ZZ} rapidly increases with g_{eff}. In contrast, the blue CAS drive efficiency is independent of g_{12} [See Eqs. (C.12) and (C.13)], allowing for the wide range of detuning and coupling strength with large η_{b} and small ξ_{ZZ}.
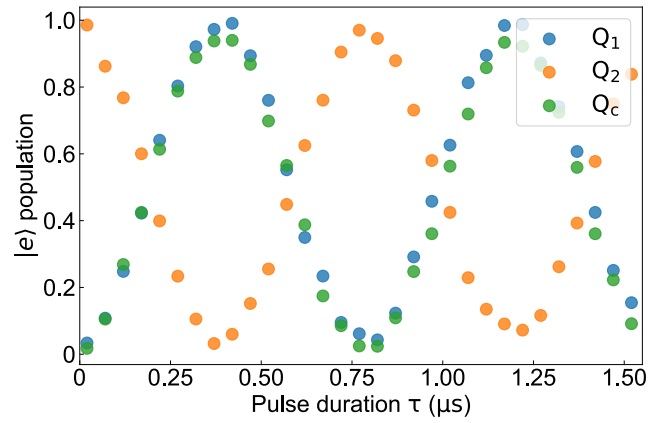
Figure C.3: Associated oscillations of the excited-state population of each transmon involved in the blue CAS transition. The vertical axis is normalized using the response signals of the ground and first-excited states of each transmon, corresponding to the excited state population of each qubit. The horizontal axis is the length of the drive pulse to the coupler transmon. The drive amplitude is $\Omega_d/2\pi \simeq 75\,\mathrm{MHz}$. Note that this data was obtained at a different cooldown from the one for the experiments in the main text.
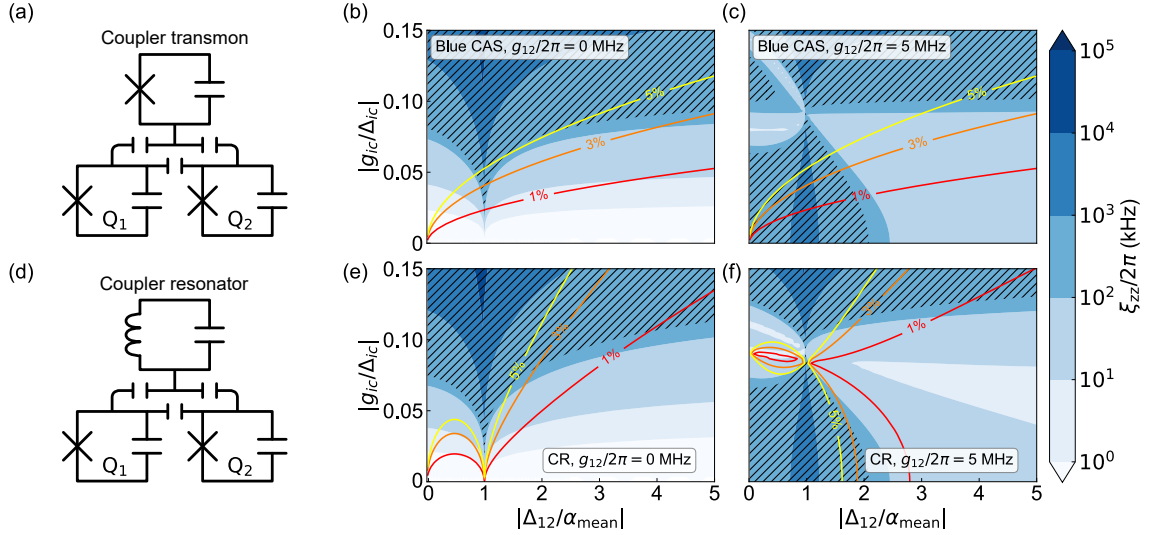
Figure C.4: (a) Circuit diagram to implement the CAS-based gates described in the main text. The residual ZZ interaction strength ξ_{ZZ} (filled contour plot) and the drive efficiency η_b of the blue CAS transition (contour line plot) are shown in (b) without and (c) with [same as in Fig. 4(b)] the direct transverse coupling g_{12}. (d) Typical circuit diagram to implement the CR gate, where we consider a linear coupler (off-resonant LC resonator) as opposed to the transmon coupler in (a). The residual ZZ interaction strength ξ_{ZZ} and drive efficiency η_{CR} of the CR gate, as a function of $|\Delta_{12}/\alpha_{mean}|$ and $|g_{ic}/\Delta_{ic}|$ are shown in (e) without and (f) with the direct transverse coupling g_{12}. Here, ξ_{ZZ} is calculated through numerical diagonalization of Eq. (C.20). The drive efficiency is defined as $\eta_{CR} = 2 \times \frac{2g_{eff}\alpha_1}{\Delta_{12}(\Delta_{12}+\alpha_1)}$ from Eq. (4.26) in Ref. [100]. The additional multiplying factor of 2 explicitly indicates the fact that a $\pi/2$-rotation of the CR gate is locally equivalent to the CNOT gate. For the calculations, we use the same parameters as in the case with the CAS transitions except for the anharmonicities of the linear coupler, $\alpha_c/2\pi = 0$ GHz, and the data transmons, $\alpha_1/2\pi = \alpha_2/2\pi = -0.3$ GHz. The latter value is typical and indeed more favorable for CR gates.

Appendix D

Notes on "Spin-dependent force in a circuit-QED system"

Here, we summarize additional information related to the spin-dependent force experiment. Before entering into individual discussions, we introduce some notations.

We first define the dimensionless quadrature operators for a harmonic oscillator as

$$\hat{x} = \frac{\hat{a}^\dagger + \hat{a}}{\sqrt{2}}, \quad \hat{p} = i\frac{\hat{a}^\dagger - \hat{a}}{\sqrt{2}}. \tag{D.1}$$

These operators satisfy the following commutation relation

$$[\hat{x}, \hat{p}] = i. \tag{D.2}$$

Using the above dimensionless quadrature operators, the creation and annihilation operators can also be written as follows

$$\hat{a} = \frac{\hat{x} + i\hat{p}}{\sqrt{2}}, \quad \hat{a}^\dagger = \frac{\hat{x} - i\hat{p}}{\sqrt{2}}. \tag{D.3}$$

In addition, the displacement operator can be rewritten as

$$\hat{D}(\alpha) = \exp\left[\alpha\hat{a}^\dagger - \alpha^*\hat{a}\right],$$
$$= \exp\left[i\sqrt{2}(\text{Im}[\alpha]\hat{x} - \text{Re}[\alpha]\hat{p})\right], \tag{D.4}$$
$$= \cos\left(\sqrt{2}\hat{\Omega}\right) + i\sin\left(\sqrt{2}\hat{\Omega}\right), \tag{D.5}$$

where $\hat{\Omega} = \text{Im}[\alpha]\hat{x} - \text{Re}[\alpha]\hat{p}$ is introduced.

D.1 Modular measurement

Modular measurement shown in Fig. D.1 is one of the important quantum operations, and here we summarize the derivation of Eq. (7.30) and some notes on modular measurement. Assuming that the initial state is a product state, the state after the conditional displacement gate acts is

$$|\psi'\rangle_{\text{qh}} = \left(|+\rangle\langle+|\hat{D}(\alpha) + |-\rangle\langle-|\hat{D}(-\alpha)\right)|\psi\rangle_{\text{q}} \otimes |\psi\rangle_{\text{h}}, \tag{D.6}$$
$$= \hat{U}_x(\alpha)|\psi\rangle_{\text{q}} \otimes |\psi\rangle_{\text{h}} \tag{D.7}$$
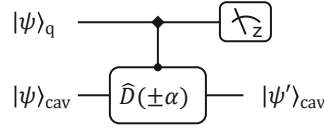
Figure D.1: Modular measurement circuit.

where the suffixes (q: qubit, h: harmonic oscillator) indicate the subsystems to which the states belong. Then, considering the z-basis measurement of the qubit, the measurement operator is $\hat{\sigma}_z \otimes \hat{I}_{\mathrm{h}}$ and the expectation value is

$$\langle \hat{\sigma}_z \rangle = \mathrm{Tr}[\hat{\sigma}_z \otimes \hat{I}_{\mathrm{h}} \hat{U}_x(\alpha) |\psi'\rangle\langle\psi'|_{\mathrm{qh}} \hat{U}_x^\dagger(\alpha)], \tag{D.8}$$

$$= \mathrm{Tr}[\underbrace{\hat{U}_x^\dagger(\alpha) \hat{\sigma}_z \otimes \hat{I}_{\mathrm{h}} \hat{U}_x(\alpha)}_{\equiv \hat{A}} |\psi'\rangle\langle\psi'|_{\mathrm{qh}}]. \tag{D.9}$$

For the last line, we used the cyclic property of the trace. Furthermore, the operator $\hat{A}$ is calculated using the BCH formula as follows

$$\hat{A} = \hat{\sigma}_z + \left(\sqrt{2}\hat{\Omega}\right)\hat{\sigma}_y - \frac{1}{2!}\left(\sqrt{2}\hat{\Omega}\right)^2 \hat{\sigma}_z - \frac{1}{3!}\left(\sqrt{2}\hat{\Omega}\right)^3 \hat{\sigma}_y + \cdots,$$

$$= \cos\left(\sqrt{2}\hat{\Omega}\right)\hat{\sigma}_z + \sin\left(\sqrt{2}\hat{\Omega}\right)\hat{\sigma}_y. \tag{D.10}$$

Thus, depending on the initial state of the qubit, the expectation values of the z-basis measurement are

$$\langle \hat{\sigma}_z \rangle = \begin{cases} \mathrm{Tr}\left[\cos\left(\sqrt{2}\hat{\Omega}\right)|\psi\rangle\langle\psi|_{\mathrm{h}}\right], & \text{for } |\psi\rangle_{\mathrm{q}} = |g\rangle_{\mathrm{q}}, \\[2ex] \mathrm{Tr}\left[\sin\left(\sqrt{2}\hat{\Omega}\right)|\psi\rangle\langle\psi|_{\mathrm{h}}\right], & \text{for } |\psi\rangle_{\mathrm{q}} = |+i\rangle_{\mathrm{q}}, \end{cases} \tag{D.11}$$

and Eq. (7.30) in the main text is reproduced.

D.2 Performance analysis of the conditional displacements

In this section, we compare the performance of conditional displacement gates using cross-Kerr interaction implemented in previous studies [86, 88, 89] and second-order nonlinearity through numerical simulations. From the main text, the Hamiltonian in the reference frame rotating at the pump drive frequency ω_d that realizes the cross-Kerr-based conditional displacement gate is

$$\hat{H}_{\mathrm{cK}}/\hbar = \Delta\hat{a}^\dagger\hat{a} + \chi\hat{a}^\dagger\hat{a}\hat{\sigma}_z + K\hat{a}^\dagger\hat{a}^\dagger\hat{a}\hat{a}, \tag{D.12}$$

where $K = \frac{\alpha_q}{2}\left(\frac{g}{\Delta}\right)^4$, $\Delta = \omega_r - \omega_d$ is a self-Kerr effect strength of the resonator. The last term has been ignored in the main text because it is proportional to the fourth order of $\frac{g}{\Delta}$, which is generally smaller than 100 Hz. However, when a strong pump drive is applied to the resonator, the effect induced by the weak self-Kerr term is enhanced, and ignoring it is not a good approximation. The strong pump drive term in the rotating frame is as follows

$$\hat{H}_p/\hbar = \varepsilon_t\hat{a} + \varepsilon_t^*\hat{a}^\dagger, \tag{D.13}$$

where ε is a time-dependent complex drive amplitude. Applying the displacement transformation to Eqs. (D.12) and (D.13), the full Hamiltonian in the displaced frame is

$$
\begin{aligned}
\hat{H}'_{\mathrm{cK}}/\hbar &= \hat{D}^\dagger(\alpha_t)\hat{H}_{\mathrm{cK}}\hat{D}(\alpha_t)/\hbar + \hat{D}^\dagger(\alpha_t)\hat{H}_p\hat{D}(\alpha_t)/\hbar, \\
&= \Delta\hat{a}^\dagger\hat{a} + \chi(\alpha_t\hat{a}^\dagger + \alpha_t^*\hat{a})\hat{\sigma}_z + \chi|\alpha_t|^2\hat{\sigma}_z + \chi\hat{a}^\dagger\hat{a}\hat{\sigma}_z \\
&\quad + K\left[\hat{a}^\dagger\hat{a}^\dagger\hat{a}\hat{a} + 2\alpha_t\hat{a}^\dagger\hat{a}^\dagger\hat{a} + 2\alpha_t^*\hat{a}^\dagger\hat{a}\hat{a} + \alpha_t^2\hat{a}^\dagger\hat{a}^\dagger + \alpha_t^*\hat{a}\hat{a} + 4|\alpha_t|^2\hat{a}^\dagger\hat{a}\right] \\
&\quad + \hat{a}^\dagger\left[\Delta\alpha_t - \frac{i\kappa}{2}\alpha_t + 2K|\alpha_t|^2\alpha_t + \varepsilon_t - i\dot{\alpha}_t\right] \\
&\quad + \hat{a}\left[\Delta\alpha_t - \frac{i\kappa}{2}\alpha_t + 2K|\alpha_t|^2\alpha_t + \varepsilon_t - i\dot{\alpha}_t\right]^*.
\end{aligned}
\tag{D.14}
$$

The last two linear terms can be eliminated by determining the time-dependent coherent amplitude α_t by solving the following nonlinear differential equation

$$
\Delta\alpha_t - \frac{i\kappa}{2}\alpha_t + 2K|\alpha_t|^2\alpha_t + \varepsilon_t = i\dot{\alpha}_t.
\tag{D.15}
$$

In addition, the term proportional to $\kappa = 1/T_1^{\mathrm{r}}$ corresponds to the displacement introduced by the energy relaxation of the resonator. For simplicity, we assume that the pump drive is resonant to the fundamental frequency of the resonator (i.e., $\Delta = 0$) and that the drive amplitude is a real number (i.e., $\alpha_t = \alpha$) and constant in time. Thus, the Hamiltonian in the displaced frame used in numerical simulations is as follows

$$
\begin{aligned}
\hat{H}^d_{\mathrm{cK}}/\hbar &= \chi(\alpha\hat{a}^\dagger + \alpha^*\hat{a})\hat{\sigma}_z + \chi|\alpha|^2\hat{\sigma}_z + \chi\hat{a}^\dagger\hat{a}\hat{\sigma}_z \\
&\quad + K\left[\hat{a}^\dagger\hat{a}^\dagger\hat{a}\hat{a} + 2\alpha\hat{a}^\dagger\hat{a}^\dagger\hat{a} + 2\alpha^*\hat{a}^\dagger\hat{a}\hat{a} + \alpha^2\hat{a}^\dagger\hat{a}^\dagger + \alpha^*\hat{a}\hat{a} + 4|\alpha|^2\hat{a}^\dagger\hat{a}\right].
\end{aligned}
\tag{D.16}
$$

Here, the first term is the generator of the spin-dependent force, and the gate speed can be increased according to $|\alpha\chi|$ by increasing the strength of the pump drive. In the previous studies, the echo sequence shown in Fig. D.2 is used instead of a single pulse to reduce the effect of low-frequency noise from the auxiliary qubit. This is why it is called the echoed-conditional displacement (ECD) gate.
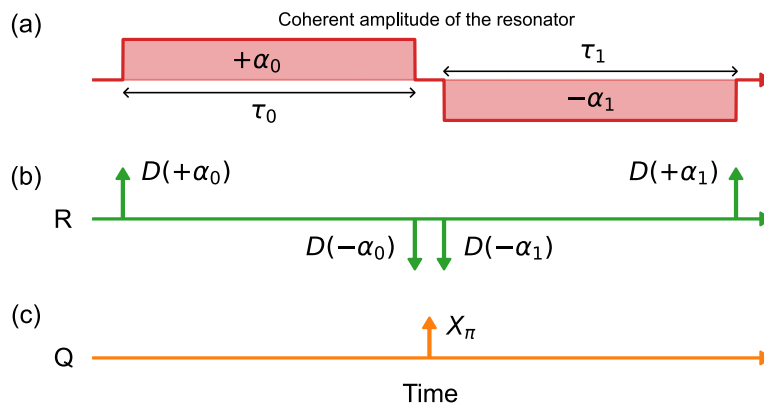
Figure D.2: Echod-conditional displacement gate sequence for numerical simulations. (a) Coherent amplitude during ECD gate. The resonator is instantaneously displaced to a coherent amplitude α and then evolves in time according to the Hamiltonian (D.16). (b) Pump pulse sequence to be applied to the resonator. The pulse duration is zero for simplicity and is assumed to be an ideal pulse (i.e., fidelity is unity). (c) Pulse sequence for the auxiliary qubit. As with the resonator, the pulse duration is zero and is assumed to be an ideal pulse (i.e., fidelity is unity).

Next, in the case of our method, we summarize the Hamiltonian used in the simulation. In a frame rotating at the frequencies of the auxiliary qubit and the resonator, the static Hamiltonian from Eq. (7.12) is as follows

$$\hat{H}_0/\hbar \simeq \chi \hat{a}^\dagger \hat{a} \hat{\sigma}_z + K \hat{a}^\dagger \hat{a}^\dagger \hat{a} \hat{a}, \tag{D.17}$$

where the artificial radiation pressure term is eliminated due to the rotating wave approximation, and this is a good approximation since $|g_{\mathrm{rp}}/\omega_r|$ is usually around 10^{-3}. The self-Kerr term of the resonator is also included as in the ECD case. Now, there can be three drive terms

$$\hat{H}_r/\hbar = \frac{\Omega_{\mathrm{sb}}}{2}\left(e^{-i\phi_r}\hat{\sigma}_-\hat{a}^\dagger + e^{-i\phi_r}\hat{\sigma}_+\hat{a}\right), \tag{D.18}$$

$$\hat{H}_b/\hbar = \frac{\Omega_{\mathrm{sb}}}{2}\left(e^{-i\phi_b}\hat{\sigma}_+\hat{a}^\dagger + e^{-i\phi_b}\hat{\sigma}_-\hat{a}\right), \tag{D.19}$$

$$\hat{H}_c/\hbar = \frac{\Omega_{\mathrm{c}}}{2}\left(e^{-i\phi_c}\hat{\sigma}_- + e^{-i\phi_c}\hat{\sigma}_-\right). \tag{D.20}$$

Here, we consider two setups that combine these drive terms. The first is to use the red-sideband drive and the carrier drive [92] as described in the text, and the pulse sequence is shown in Fig. D.3. The second setup applies all three drives simultaneously [91], and the pulse sequence is shown in Fig. D.4. We will call them SDF-1 and SDF-2 gates, respectively.

Figure D.3: Pulse sequence 1. Each pulse waveform is a perfect square, and the duration is τ. (a) The phase of the red-sideband pulses is $\phi_r = 0$ for both pulses. (b) The phases of the carrier pulses are $\phi_c = 0$, and $\phi_c = \pi$ for the first and second pulses, respectively. This sequence is the rotary echo, which can mitigate the effects of low-frequency noise in the auxiliary qubit.

D.2.1   Numerical simulation

Here, we evaluate the accuracy of the conditional displacement gates realized by respective methods using the introduced Hamiltonians. It is computationally expensive to compute the propagator of the resonator and auxiliary qubit, including dissipation. Therefore, we generate the cat state

$$|+\mathrm{cat}\rangle \propto |\beta\rangle + |-\beta\rangle \tag{D.21}$$

by the conditional displacement gates, compare their quality by numerically solving master equations and obtaining state infideliteis [109] for each displacement length (cat size). For each target displacement length, the state infidelity is minimized. The Nelder-Mead method is used for minimization, and the optimization parameters are described in detail
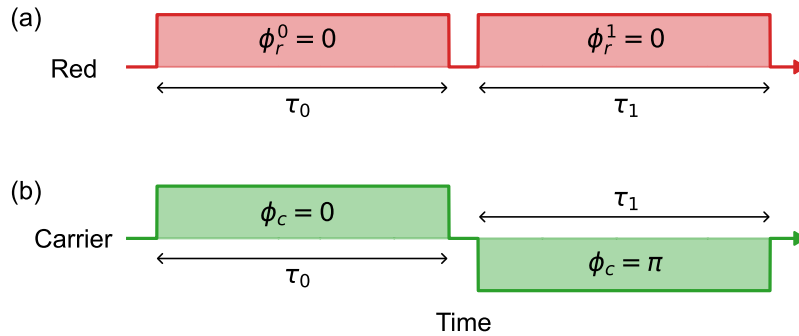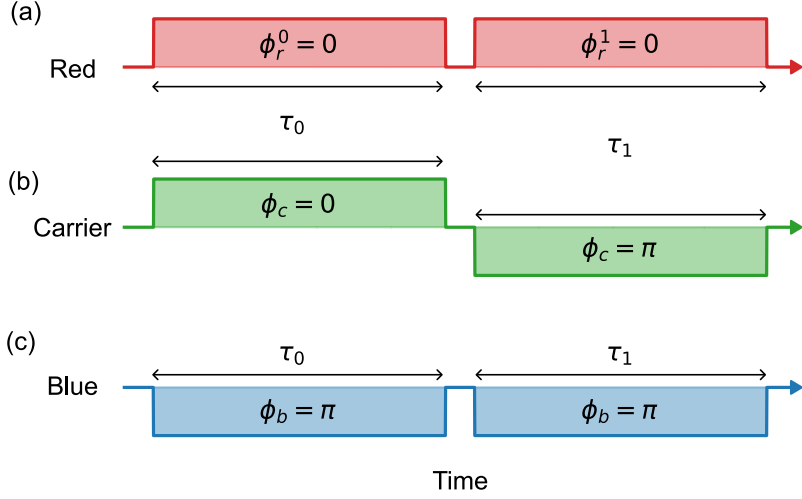
Figure D.4: Pulse sequence 2. Each pulse waveform is a perfect square, and the duration is τ. (a) The phase of the red-sideband pulses is $\phi_r = 0$ for both pulses. (b) The phases of the carrier pulses are $\phi_c = 0$, and $\phi_c = \pi$ for the first and second pulses, respectively. This sequence is the rotary echo, which can mitigate the effects of low-frequency noise in the auxiliary qubit. (c) The phase of the blue-sideband pulses is $\phi_r = \pi$ for both pulses.

later as they are situation-dependent. As an additional common feature, the dissipation rates are calculated from the coherence times as follows

$$\kappa_1 = 1/T_1^{\mathrm{r}}, \tag{D.22}$$
$$\kappa_\phi = 1/T_\phi = 1/T_2^{\mathrm{r}} - 1/2T_1^{\mathrm{r}}, \tag{D.23}$$
$$\gamma_1 = 1/T_1^{\mathrm{q}}, \tag{D.24}$$
$$\gamma_\phi = 1/T_\phi = 1/T_2^{\mathrm{q}} - 1/2T_1^{\mathrm{q}}. \tag{D.25}$$

Echoed-conditional displacement

For the ECD gate, the master equation to be solved is

$$\dot{\rho}_d = -\frac{i}{\hbar}\left[\hat{H}_{\mathrm{cK}}^d(\alpha_i), \hat{\rho}_d\right] + \kappa_1 \mathcal{D}[\hat{a}] + 2\kappa_\phi \mathcal{D}[(\hat{a}^\dagger + \alpha_i^*)(\hat{a} + \alpha_i)] + \gamma_1 \mathcal{D}[\hat{\sigma}_-] + 2\gamma_\phi \mathcal{D}[\hat{\sigma}_z], \tag{D.26}$$

where $\hat{\rho}_d = \hat{D}^\dagger(\alpha)\hat{\rho}\hat{D}(\alpha)$ is a density operator in the displacement frame, and α_i, $i \in \{0, 1\}$ is coherent amplitude during the gate sequence. In addition, $\mathcal{D}[\hat{L}]\hat{\rho} = \hat{L}\hat{\rho}\hat{L}^\dagger - 1/2\{\hat{L}^\dagger\hat{L}, \hat{\rho}\}$ is Lindbladian. The master equation follows the sequence shown in Fig.D.2. The initial state of the first half of the sequence is $|0\rangle_{\mathrm{r}} \otimes |+\rangle_{\mathrm{q}}$, and the initial state of the second half is the final state of the first half calculation multiplied by X_π. The four optimization parameters are $\{\arg \alpha_0, \ \arg \alpha_1, \ \tau_0, \ \tau_1\}$.

Spin-dependent force

For the SDF-1 gate, the master equation to be solved is

$$\dot{\rho} = -\frac{i}{\hbar}\left[\hat{H}_0 + \hat{H}_r + \hat{H}_c, \hat{\rho}\right] + \kappa_1 \mathcal{D}[\hat{a}] + 2\kappa_\phi \mathcal{D}[\hat{a}^\dagger\hat{a}] + \gamma_1 \mathcal{D}[\hat{\sigma}_-] + 2\gamma_\phi \mathcal{D}[\hat{\sigma}_z], \tag{D.27}$$

and for the SDF-2 gate is

$$\dot{\rho} = -\frac{i}{\hbar}\left[\hat{H}_0 + \hat{H}_r + \hat{H}_c + \hat{H}_b, \hat{\rho}\right] + \kappa_1 \mathcal{D}[\hat{a}] + 2\kappa_\phi \mathcal{D}[\hat{a}^\dagger\hat{a}] + \gamma_1 \mathcal{D}[\hat{\sigma}_-] + 2\gamma_\phi \mathcal{D}[\hat{\sigma}_z]. \tag{D.28}$$

Table D.1: Parameter set 1. The numbers in brackets are for the pulse sequence 2.

Parameter	ECD (Break-even) *[86]	ECD	SDF (Our method)
$\lvert\Delta\rvert = \lvert\tilde{\omega}_r - \tilde{\omega}_q\rvert$	2 GHz	2 GHz	2 GHz
$\lvert g/\Delta\rvert$	0.01	0.01	0.02
χ	29 kHz	29 kHz	84 kHz
K	-1 Hz	-1 Hz	-14 Hz
T_1^r	*600 μs	60 μs	60 μs
T_2^r	*$T_1^r \times 1.5$	$T_1^r \times 1.5$	$T_1^r \times 1.5$
T_1^q	*250 μs	50 μs	50 μs
$T_2^{e,q}$	*$T_1^q/1.5$	20 μs	20 μs
$\lvert\alpha\rvert^2$	*150	50, 150, 300	–
Ω_{sb}	–	–	1.0(0.7) MHz
Ω_{c}	–	–	50(10) MHz
Hilbert space dimension	$(50 \times 2)^2$	$(50 \times 2)^2$	$(50 \times 2)^2$

Table D.2: Parameter set 2. The numbers in brackets are for the pulse sequence 2.

Parameter	ECD (Break-even) *[86]	ECD	SDF (Our method)
$\lvert\Delta\rvert = \lvert\tilde{\omega}_r - \tilde{\omega}_q\rvert$	2 GHz	2 GHz	2 GHz
$\lvert g/\Delta\rvert$	0.01	0.01	0.02
χ	29 kHz	29 kHz	84 kHz
K	-1 Hz	-1 Hz	-14 Hz
T_1^r	*600 μs	100 μs	100 μs
T_2^r	*$T_1^r \times 1.5$	$T_1^r \times 1.5$	$T_1^r \times 1.5$
T_1^q	*250 μs	100 μs	100 μs
$T_2^{e,q}$	*$T_1^q/1.5$	100 μs	100 μs
$\lvert\alpha\rvert^2$	*150	50, 150, 300	–
Ω_{sb}	–	–	1.0(0.7) MHz
Ω_{c}	–	–	50(10) MHz
Hilbert space dimension	$(50 \times 2)^2$	$(50 \times 2)^2$	$(50 \times 2)^2$

The master equations follow the sequences shown in Fig.D.3, and D.4, respectively. For both cases, the initial state of the first half of the sequence is $\lvert 0\rangle_r \otimes \lvert 0\rangle_q$, and the initial state of the second half is the final state of the first half calculation. The carrier drive phase is inverted in the first and second sequences, so the effect eventually cancels out. During optimization, the phases of the carrier drive and blue sideband drive are fixed for both cases, and the four optimization parameters are $\{\phi_r^0,\ \phi_r^1,\ \tau_0,\ \tau_1\}$. As indicated in Tabs. D.1 and D.2, the effective drive strengths for both cases are set to 1 MHz and 0.7 MHz, respectively, which could be obtained without difficulty in the experiment.

Result

The simulation results are shown in Figs. D.5 and D.6, and they suggest that the method used in this study is more resistant to decoherence than the ECD. Note that the pulse waveform is not included in the optimization parameters to reduce the computation time, and there is room for further fidelity improvement in both cases. Furthermore, instead of using a transmon, our method (SDF-1) employs a cubic transmon with a lower anharmonicity. Consequently, the SDF-1, which needs a powerful carrier drive, could be worse than this result. Conversely, it is suggested that SDF-1 could achieve high accuracy even

without a strong drive. In the future, we should move to SDF-2 implementation.
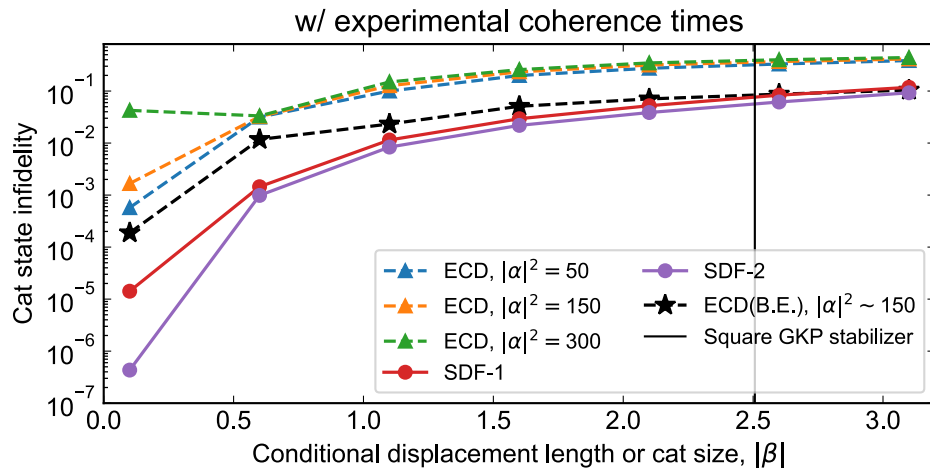
Figure D.5: Simulation results using parameter set 1. Dashed lines with a triangular marker indicate the ECD cases; Solid lines with a circle marker indicate the SDF cases. The result using the break-even experiment parameters [86] is shown with a dashed line and a star marker. The solid black line shows the amplitude required to measure the stabilizer of the square GKP code [110].

Figure D.6: Simulation results using parameter set 2. The other notations are the same as in Fig. D.5.

Bibliography

[1] P. Benioff, "The computer as a physical system: a microscopic quantum mechanical hamiltonian model of computers as represented by turing machines", Journal of Statistical Physics **22**, 563 (1980) (cited on page 1).

[2] R. P. Feynman, "Simulating physics with computers", International Journal of Theoretical Physics **21**, 467 (1982) (cited on page 1).

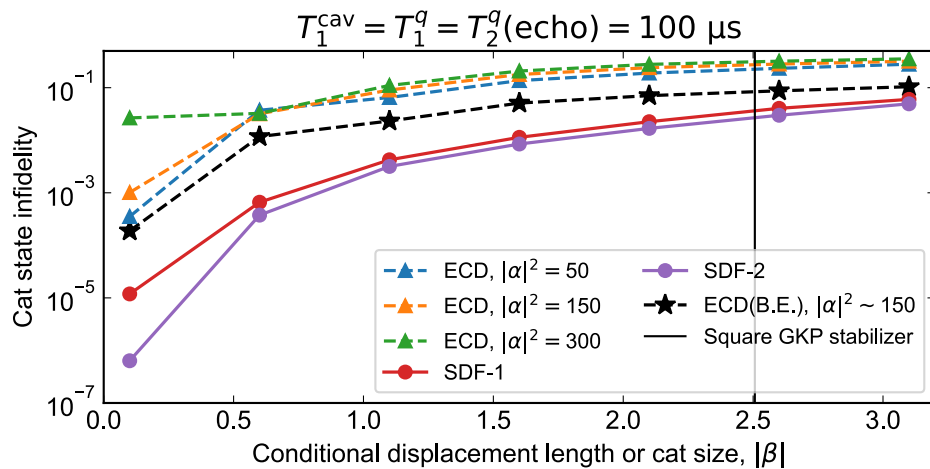[3] C. Monroe *et al.*, "Demonstration of a fundamental quantum logic gate", Phys. Rev. Lett. **75**, 4714 (1995) (cited on page 1).

[4] Y. Nakamura *et al.*, "Coherent control of macroscopic quantum states in a single-cooper-pair box", nature **398**, 786 (1999) (cited on pages 1, 8, 46).

[5] J. Preskill, "Quantum Computing in the NISQ era and beyond", Quantum **2**, 79 (2018) (cited on page 1).

[6] B. Josephson, "Possible new effect in superconducting tunneling", Phys. Lett. **1**, 251 (1962) (cited on page 4).

[7] J. Koch *et al.*, "Charge-insensitive qubit design derived from the cooper pair box", Phys. Rev. A **76**, 042319 (2007) (cited on pages 8–10, 47, 53, 55).

[8] R. Barends *et al.*, "Coherent josephson qubit suitable for scalable quantum integrated circuits", Phys. Rev. Lett. **111**, 080502 (2013) (cited on pages 8, 47).

[9] U. Vool *et al.*, "Introduction to quantum electromagnetic circuits", International Journal of Circuit Theory and Applications **45**, 897 (2017) (cited on page 10).

[10] A. Noguchi *et al.*, "Fast parametric two-qubit gates with suppressed residual interaction using the second-order nonlinearity of a cubic transmon", Phys. Rev. A **102**, 062408 (2020) (cited on pages 11, 13, 14, 53, 61, 62).

[11] N. E. Frattini *et al.*, "3-wave mixing Josephson dipole element", Applied Physics Letters **110**, 222603 (2017) (cited on page 14).

[12] A. A. Clerk *et al.*, "Introduction to quantum noise, measurement, and amplification", Rev. Mod. Phys. **82**, 1155 (2010) (cited on pages 18, 85).

[13] D. M. Pozar, *Microwave engineering* (John wiley & sons, 2011) (cited on pages 19, 20).

[14] V. Ambegaokar *et al.*, "Tunneling between superconductors", Phys. Rev. Lett. **11**, 104 (1963) (cited on page 21).

[15] H. Ibach *et al.*, *Solid-state physics: an introduction to principles of materials* (Springer, Berlin, 1995) (cited on page 21).

[16] A. Osman *et al.*, "Simplified josephson-junction fabrication process for reproducibly high-performance superconducting qubits", Applied Physics Letters **118**, 064002 (2021) (cited on pages 22, 47, 54, 65).

[17] J. M. Martinis, "Surface loss calculations and design of a superconducting transmon qubit with tapered wiring", npj Quantum Information **8**, 26 (2022) (cited on pages 23, 47).

[18] S. Shirai *et al.*, "All-microwave manipulation of superconducting qubits with a fixed-frequency transmon coupler", Phys. Rev. Lett. **130**, 260601 (2023) (cited on page 29).

[19] J. M. Sage *et al.*, "Study of loss in superconducting coplanar waveguide resonators", Journal of Applied Physics **109**, 063915 (2011) (cited on page 45).

[20] J. Verjauw *et al.*, "Investigation of microwave loss induced by oxide regrowth in high-q niobium resonators", Phys. Rev. Appl. **16**, 014018 (2021) (cited on page 45).

[21] M. V. P. Altoé *et al.*, "Localization and mitigation of loss in niobium superconducting circuits", PRX Quantum **3**, 020312 (2022) (cited on page 45).

[22] R. Sun *et al.*, "Fabrication of (200)-oriented tin films on si (100) substrates by dc magnetron sputtering", IEEE Transactions on Applied Superconductivity **25**, 1 (2015) (cited on page 45).

[23] A. Shearrow *et al.*, "Atomic layer deposition of titanium nitride for quantum circuits", Applied Physics Letters **113**, 212601 (2018) (cited on page 45).

[24] Y. Nakamura *et al.*, "Charge echo in a cooper-pair box", Phys. Rev. Lett. **88**, 047901 (2002) (cited on page 46).

[25] J. M. Martinis *et al.*, "Rabi oscillations in a large josephson-junction qubit", Phys. Rev. Lett. **89**, 117901 (2002) (cited on page 46).

[26] I. Chiorescu *et al.*, "Coherent quantum dynamics of a superconducting flux qubit", Science **299**, 1869 (2003) (cited on page 46).

[27] F. Yoshihara *et al.*, "Decoherence of flux qubits due to $1/f$ flux noise", Phys. Rev. Lett. **97**, 167001 (2006) (cited on page 46).

[28] J. Bylander *et al.*, "Noise spectroscopy through dynamical decoupling with a superconducting flux qubit", Nature Physics **7**, 565 (2011) (cited on page 46).

[29] J. A. Schreier *et al.*, "Suppressing charge noise decoherence in superconducting charge qubits", Phys. Rev. B **77**, 180502 (2008) (cited on page 46).

[30] H. Paik *et al.*, "Observation of high coherence in josephson junction qubits measured in a three-dimensional circuit qed architecture", Phys. Rev. Lett. **107**, 240501 (2011) (cited on page 46).

[31] C. Rigetti *et al.*, "Superconducting qubit in a waveguide cavity with a coherence time approaching 0.1 ms", Phys. Rev. B **86**, 100506 (2012) (cited on page 46).

[32] J. B. Chang *et al.*, "Improved superconducting qubit coherence using titanium nitride", Applied Physics Letters **103**, 012602 (2013) (cited on page 46).

[33] R. Barends *et al.*, "Coherent josephson qubit suitable for scalable quantum integrated circuits", Phys. Rev. Lett. **111**, 080502 (2013) (cited on page 46).

[34] A. P. M. Place *et al.*, "New material platform for superconducting transmon qubits with coherence times exceeding 0.3 milliseconds", Nature Communications **12**, 1779 (2021) (cited on page 46).

[35] C. Wang *et al.*, "Towards practical quantum computers: transmon qubit with a lifetime approaching 0.5 milliseconds", npj Quantum Information **8**, 3 (2022) (cited on page 46).

[36] H. Deng *et al.*, "Titanium nitride film on sapphire substrate with low dielectric loss for superconducting qubits", Phys. Rev. Appl. **19**, 024013 (2023) (cited on pages 46, 47).

[37] F. Yan *et al.*, "The flux qubit revisited to enhance coherence and reproducibility", Nature Communications **7**, 12964 (2016) (cited on page 46).

[38] V. E. Manucharyan *et al.*, "Fluxonium: single cooper-pair circuit free of charge offsets", Science **326**, 113 (2009) (cited on page 46).

[39] L. B. Nguyen *et al.*, "High-coherence fluxonium qubit", Phys. Rev. X **9**, 041041 (2019) (cited on page 46).

[40] A. Somoroff *et al.*, "Millisecond coherence in a superconducting qubit", Phys. Rev. Lett. **130**, 267001 (2023) (cited on page 46).

[41] M. D. Reed *et al.*, "Fast reset and suppressing spontaneous emission of a superconducting qubit", Applied Physics Letters **96**, 203110 (2010) (cited on pages 47, 55).

[42] E. Jeffrey *et al.*, "Fast accurate state measurement with superconducting qubits", Phys. Rev. Lett. **112**, 190504 (2014) (cited on page 47).

[43] S. Huang *et al.*, "Microwave package design for superconducting quantum processors", PRX Quantum **2**, 020306 (2021) (cited on page 47).

[44] M. Carroll *et al.*, "Dynamics of superconducting qubit relaxation times", npj Quantum Information **8**, 132 (2022) (cited on page 47).

[45] C. Kurter *et al.*, "Quasiparticle tunneling as a probe of josephson junction barrier and capacitor material in superconducting qubits", npj Quantum Information **8**, 31 (2022) (cited on page 47).

[46] A. P. Vepsäläinen *et al.*, "Impact of ionizing radiation on superconducting qubit coherence", Nature **584**, 551 (2020) (cited on page 47).

[47] R. Barends *et al.*, "Minimizing quasiparticle generation from stray infrared light in superconducting quantum circuits", Applied Physics Letters **99**, 113507 (2011) (cited on page 47).

[48] C. Wang *et al.*, "Surface participation and dielectric loss in superconducting qubits", Applied Physics Letters **107**, 162601 (2015) (cited on page 47).

[49] C. E. Murray *et al.*, "Analytical determination of participation in superconducting coplanar architectures", IEEE Transactions on Microwave Theory and Techniques **66**, 3724 (2018) (cited on page 47).

[50] D. R. Lide, *Crc handbook of chemistry and physics*, Vol. 85 (CRC press, 2004) (cited on page 51).

[51] P. Krantz *et al.*, "A quantum engineer's guide to superconducting qubits", Applied Physics Reviews **6**, 021318 (2019) (cited on page 53).

[52] Z. Chen *et al.*, "Exponential suppression of bit or phase errors with cyclic error correction", Nature **595**, 383 (2021) (cited on page 53).

[53] C. Rigetti *et al.*, "Fully microwave-tunable universal gates in superconducting qubits with linear couplings and fixed transition frequencies", Phys. Rev. B **81**, 134507 (2010) (cited on page 53).

[54] S. Poletto *et al.*, "Entanglement of two superconducting qubits in a waveguide cavity via monochromatic two-photon excitation", Phys. Rev. Lett. **109**, 240505 (2012) (cited on page 53).

[55] J. M. Chow *et al.*, "Microwave-activated conditional-phase gate for superconducting qubits", New Journal of Physics **15**, 115012 (2013) (cited on page 53).

[56] H. Paik *et al.*, "Experimental demonstration of a resonator-induced phase gate in a multiqubit circuit-qed system", Phys. Rev. Lett. **117**, 250502 (2016) (cited on page 53).

[57] S. Krinner *et al.*, "Demonstration of an all-microwave controlled-phase gate between far-detuned qubits", Phys. Rev. Applied **14**, 044039 (2020) (cited on pages 53, 91).

[58] B. K. Mitchell *et al.*, "Hardware-efficient microwave-activated tunable coupling between superconducting qubits", Phys. Rev. Lett. **127**, 200502 (2021) (cited on page 53).

[59] K. Heya *et al.*, "Cross-cross resonance gate", PRX Quantum **2**, 040336 (2021) (cited on page 53).

[60] J. M. Chow *et al.*, "Simple all-microwave entangling gate for fixed-frequency superconducting qubits", Phys. Rev. Lett. **107**, 080502 (2011) (cited on page 53).

[61] S. Sheldon *et al.*, "Procedure for systematically tuning up cross-talk in the cross-resonance gate", Phys. Rev. A **93**, 060302(R) (2016) (cited on page 53).

[62] A. Kandala *et al.*, "Demonstration of a high-fidelity cnot gate for fixed-frequency transmons with engineered ZZ suppression", Phys. Rev. Lett. **127**, 130501 (2021) (cited on pages 53, 59).

[63] M. Malekakhlagh *et al.*, "First-principles analysis of cross-resonance gate operation", Phys. Rev. A **102**, 042605 (2020) (cited on page 53).

[64] A. Morvan *et al.*, "Optimizing frequency allocation for fixed-frequency superconducting quantum processors", Phys. Rev. Research **4**, 023079 (2022) (cited on page 53).

[65] C. Granata *et al.*, "Trimming of critical current in niobium josephson devices by laser annealing", in Journal of physics: conference series, Vol. 97, 1 (IOP Publishing, 2008), p. 012110 (cited on page 53).

[66] J. B. Hertzberg *et al.*, "Laser-annealing josephson junctions for yielding scaled-up superconducting quantum processors", npj Quantum Information **7**, 129 (2021) (cited on page 53).

[67] E. J. Zhang *et al.*, "High-performance superconducting quantum processors via laser annealing of transmon qubits", Science Advances **8**, eabi6690 (2022) (cited on page 53).

[68] H. Kim *et al.*, "Effects of laser-annealing on fixed-frequency superconducting qubits", Applied Physics Letters **121**, 142601 (2022) (cited on page 53).

[69] R. Lescanne *et al.*, "Irreversible qubit-photon coupling for the detection of itinerant microwave photons", Phys. Rev. X **10**, 021038 (2020) (cited on page 53).

[70] P. Mundada *et al.*, "Suppression of qubit crosstalk in a tunable coupling superconducting circuit", Phys. Rev. Applied **12**, 054023 (2019) (cited on pages 53, 59).

[71] E. Sjöqvist, "Geometric phases in quantum information", International Journal of Quantum Chemistry **115**, 1311 (2015) (cited on page 55).

[72] J. Johansson *et al.*, "Qutip: an open-source python framework for the dynamics of open quantum systems", Computer Physics Communications **183**, 1760 (2012) (cited on page 56).

[73] J. Johansson *et al.*, "Qutip 2: a python framework for the dynamics of open quantum systems", Computer Physics Communications **184**, 1234 (2013) (cited on page 56).

[74] C. E. Murray *et al.*, "Analytical determination of participation in superconducting coplanar architectures", IEEE Transactions on Microwave Theory and Techniques **66**, 3724 (2018) (cited on page 57).

[75] F. Motzoi *et al.*, "Simple pulses for elimination of leakage in weakly nonlinear qubits", Phys. Rev. Lett. **103**, 110501 (2009) (cited on page 57).

[76] J. Garbow *et al.*, "Bilinear rotation decoupling of homonuclear scalar interactions", Chemical Physics Letters **93**, 504 (1982) (cited on pages 57, 58).

[77] J. Ku *et al.*, "Suppression of unwanted ZZ interactions in a hybrid two-qubit system", Phys. Rev. Lett. **125**, 200504 (2020) (cited on pages 57, 58).

[78] R. Barends *et al.*, "Superconducting quantum circuits at the surface code threshold for fault tolerance", Nature **508**, 500 (2014) (cited on page 58).

[79] D. C. McKay *et al.*, "Efficient Z gates for quantum computing", Phys. Rev. A **96**, 022330 (2017) (cited on page 57).

[80] E. Magesan *et al.*, "Efficient measurement of quantum gate error by interleaved randomized benchmarking", Phys. Rev. Lett. **109**, 080505 (2012) (cited on page 57).

[81] N. Khaneja *et al.*, "Optimal control of coupled spin dynamics: design of nmr pulse sequences by gradient ascent algorithms", Journal of Magnetic Resonance **172**, 296 (2005) (cited on page 59).

[82] Y. Baum *et al.*, "Experimental deep reinforcement learning for error-robust gate-set design on a superconducting quantum computer", PRX Quantum **2**, 040324 (2021) (cited on page 59).

[83] H. K. Cummins *et al.*, "Tackling systematic errors in quantum logic gates with composite rotations", Phys. Rev. A **67**, 042308 (2003) (cited on page 59).

[84] H. K. Cummins *et al.*, "Use of composite rotations to correct systematic errors in nmr quantum computation", New Journal of Physics **2**, 6 (2000) (cited on page 59).

[85] Z. Ni *et al.*, "Scalable method for eliminating residual ZZ interaction between superconducting qubits", Phys. Rev. Lett. **129**, 040502 (2022) (cited on page 59).

[86] V. V. Sivak *et al.*, "Real-time quantum error correction beyond break-even", Nature **616**, 50 (2023) (cited on pages 61, 96, 100, 101).

[87] Z. Ni *et al.*, "Beating the break-even point with a discrete-variable-encoded logical qubit", Nature **616**, 56 (2023) (cited on page 61).

[88] P. Campagne-Ibarcq *et al.*, "Quantum error correction of a qubit encoded in grid states of an oscillator", Nature **584**, 368 (2020) (cited on pages 61, 96).

[89] A. Eickbusch *et al.*, "Fast universal control of an oscillator with weak dispersive coupling to a qubit", Nature Physics **18**, 1464 (2022) (cited on pages 61, 96).

[90] P. C. Haljan *et al.*, "Spin-dependent forces on trapped ions for phase-stable quantum gates and entangled states of spin and motion", Phys. Rev. Lett. **94**, 153602 (2005) (cited on page 61).

[91] K. Mølmer *et al.*, "Multiparticle entanglement of hot trapped ions", Phys. Rev. Lett. **82**, 1835 (1999) (cited on pages 61, 98).

[92]   A. Bermudez *et al.*, "Robust trapped-ion quantum logic gates by continuous dy-
       namical decoupling", Phys. Rev. A **85**, 040302 (2012) (cited on pages 61, 98).

[93]   T. P. Harty *et al.*, "High-fidelity trapped-ion quantum logic using near-field mi-
       crowaves", Phys. Rev. Lett. **117**, 140501 (2016) (cited on page 61).

[94]   S. A. Caldwell *et al.*, "Parametrically activated entangling gates using transmon
       qubits", Phys. Rev. Appl. **10**, 034050 (2018) (cited on page 62).

[95]   R. Manenti *et al.*, "Full control of superconducting qubits with combined on-chip
       microwave and flux lines", Applied Physics Letters **119**, 144001 (2021) (cited on
       page 62).

[96]   A. Vrajitoarea *et al.*, "Quantum control of an oscillator using a stimulated joseph-
       son nonlinearity", Nature Physics **16**, 211 (2020) (cited on page 62).

[97]   C. Flühmann *et al.*, "Direct characteristic-function tomography of quantum states
       of the trapped-ion motional oscillator", Phys. Rev. Lett. **125**, 043602 (2020) (cited
       on page 66).

[98]   D. Leibfried *et al.*, "Experimental preparation and measurement of quantum states
       of motion of a trapped atom", Journal of Modern Optics **44**, 2485 (1997) (cited on
       pages 66, 67).

[99]   D. Kienzler *et al.*, "Quantum harmonic oscillator state synthesis by reservoir engi-
       neering", Science **347**, 53 (2015) (cited on pages 66, 67).

[100] E. Magesan *et al.*, "Effective hamiltonian models of the cross-resonance gate",
       Phys. Rev. A **101**, 052308 (2020) (cited on pages 83, 94).

[101] A. Blais *et al.*, "Circuit quantum electrodynamics", Rev. Mod. Phys. **93**, 025005
       (2021) (cited on page 83).

[102] K. Koshino, *Cavity-quantum electromagnetic dynamics*, 1st edition (Science, 2020)
       (cited on page 85).

[103] R. Winkler, *Spin-Orbit Coupling Effects in Two-Dimensional Electron and Hole
       Systems*, Tracts in Modern Physics (Springer, Berlin, 2003) (cited on page 87).

[104] M. Leskes *et al.*, "Floquet theory in solid-state nuclear magnetic resonance", Progress
       in Nuclear Magnetic Resonance Spectroscopy **57**, 345 (2010) (cited on page 89).

[105] C. J. Wood *et al.*, "Quantification and characterization of leakage errors", Phys.
       Rev. A **97**, 032306 (2018) (cited on page 90).

[106] D. I. Schuster *et al.*, "Ac stark shift and dephasing of a superconducting qubit
       strongly coupled to a cavity field", Phys. Rev. Lett. **94**, 123602 (2005) (cited on
       page 91).

[107] A. Schneider *et al.*, "Local sensing with the multilevel ac stark effect", Phys. Rev.
       A **97**, 062334 (2018) (cited on page 91).

[108] S. Zeytino ǧlu *et al.*, "Microwave-induced amplitude- and phase-tunable qubit-
       resonator coupling in circuit quantum electrodynamics", Phys. Rev. A **91**, 043846
       (2015) (cited on page 91).

[109] M. A. Nielsen *et al.*, *Quantum computation and quantum information*, 10th an-
       niversary edition (Cambridge University Press, 2010) (cited on page 98).

[110] D. Gottesman *et al.*, "Encoding a qubit in an oscillator", Phys. Rev. A **64**, 012310
       (2001) (cited on page 101).